Microstructure and mechanical properties of electrodeposited copper films

By

XIAONING SONG

A thesis submitted to the College of Engineering and Physical Sciences of the University of Birmingham for the degree of

MASTER OF PHILOSOPHY

School of Metallurgy and Materials
College of Engineering and Physical Sciences
The University of Birmingham
Birmingham
England
B15 2TT

Abstract

Nanostructured materials have assumed increasing scientific and technological interest due to the significant improvement of mechanical properties compared to their coarse-grained counterparts. Nanostructured electrodeposited copper film, for example, is of interest for applications in ultra large-scale integrated (ULSI) devices. However, the microstructure evolution of the copper film at room temperature, which is termed self-annealing, can cause reliability problems. The understanding of the microstructure, in particular the stability of the electrodeposited Cu film, relative to its mechanical properties, is essential to the further development of the performance and reliability of the resulting devices.

In this work, the microstructure and mechanical properties of electrodeposited copper films have been investigated. These copper films were electrodeposited in an additive-free acidified copper sulphate solution by employing either direct current (DC) or pulsed current (PC) of different current densities. The microstructure of the films has been studied using electron microscopy and the mechanical properties have been examined using nanoindentation. It has been noted that the microstructure of the thicker electrodeposited copper films was controlled by deposition parameters. It has been found that the substrate has no significant effect on the texture of the thick copper films formed where the growth direction is parallel to <110>. The twin density in the deposited copper film seems varying with the off-time of the deposition and the highest twin density was observed in the sample deposited with 0.02 *s* on-time and 2 *s*

off-time. Self-annealing (grain growth at ambient condition) of the deposited copper film has been confirmed using focused ion beam imaging and back-scattered electron imaging. Grains with <110> parallel to the film normal direction have a large propensity to grow than those with other orientations. The nanoindentation results show that the high hardness over elastic modulus ratio measured is associated with the high twin density.

Acknowledgements

Sincere and special thanks to Dr Yu-Lung CHIU in School of Metallurgy and Materials, for his kindness, patience, supervision and support. I would like to thank Professor Ian Jones, for the kind academic guidance.

Thanks to Dr R.G. DING, Dr M.Q. CHU and my colleagues in Electron Microscopy Group. I always remember and represent the people who ever help me in my life.

Table of contents

Chapter 1 Introduction

Due to its higher electro-migration resistance and lower electrical resistivity, copper has replaced aluminum as the ultra large-scale integration (ULSI) metallisation material [1, 2]. Electrodeposited copper has been demonstrated to be effective for high-performance devices due to the resulting good physical properties [2, 3]. Copper films can be electrodeposited by either direct current (DC) or pulsed current (PC) techniques. However, several researchers have reported the abnormal grain growth in DC deposited copper films after deposition in the film-thickness range of 1.5-14 μm, which was described as self-annealing. Although limited subsequent work has been reported, self-annealing is recognized to result in changes in film resistivity, residual stress and texture [3-5]. Meanwhile, previous research has indicated that, in a PC deposition cycle, using electrolysis with a modulated current [6] or by adjusting the applied periodic current [7], copper films with different microstructures can be obtained. For example, it has been reported that due to the presence of high density of twins, pure copper with both high strength and high electrical conductivity can be obtained by pulsed electrodeposition [8], but less attention has been paid to study the effect of off-time on the microstructure of pulsed electrodeposited copper.

The trade-off between electrical resistivity and mechanical strength of copper deposits is key to its industrial application. It has been demonstrated that pulsed electrodeposition is an effective way to achieve better mechanical and physical properties in copper deposits [9, 10], as is shown in table. 1.1. So far, most researches have been devoted to electrodeposited copper films with thicknesses ranging from several hundreds of nanometres to about 2 μm [11-13]. This was recently extended to

studies on 20 μm thick electrodeposited copper films [14,15,16]. The stability of a DC deposited copper film with a thickness of around 80 μm and the effect of off-time on the PC copper deposit have yet investigated. Furthermore, it is still unclear that how the micro-mechanical properties of either DC or PC electrodeposited copper films depend on the microstructure [16-19]. The purpose of the present study is to examine the effect of off-time on their microstructures, and to understand the relationship between the resultant microstructure and mechanical properties. Self-annealing was further examined in a thick DC copper film. The films were prepared by electrodeposition using either direct current or pulsed current at room temperature. Selected pulsed electrodeposition parameters were used to examine the off-time effect on its microstructure. The microstructure of the copper films and its evolution were characterised using scanning electron microscopy (SEM), transmission electron microscopy (TEM) and focused ion beam (FIB) microscopy. Self-annealing was examined on a thick copper film deposited with direct current. Nanoindentation was performed to measure the hardness and elastic modulus of the films. The mechanical property results have then been analysed and discussed vis-à-vis the microstructure of the films. A micro-tensile testing rig was designed which could be used for future small scale mechanical testing.

Recapitulating, this project aims to:

- Investigate the off-time effect on the microstructures of PC prepared copper films.
- Examine the stability of the bulk DC deposited copper film.
- Improve the understanding of how mechanical properties of electrodeposited copper films are dependent on their microstructure.

Table 1.1 Typical properties (range) of electrodeposited copper [9, 10]

Properties / Optimized Property	*Tensile Strength (kg/mm^2)*	*Elongation (%)*	*Internal Stress (kg/mm^2)*	*Hardness (kg/mm^2)*	*Electrical Resistivity ($\mu\Omega$, cm)*
Set 1: *High strength*	**45 - 63.5**	4 - 18	4.2 or 3.6 to 5.5	131-159	1.75 - 2.02
Set 2: *Hardness*	3.5-55.5	0 -10	4.2 or 3.0	**193 - 350**	1.96 - 4.60
Set 3: *Low electrical Resistivity*	18.5-27	15-41	0.5 – 1.6	48 - 64	**1.70 - 1.73**

References

1. R. Rosenberg, D. C. Edelstein, C.K. Hu, K. P. Rodbell, Annual Review of Materials Research. 30 (2000) 229.
2. K. Bi, S. Yu, H, Xie, Y. Q. Li, S. Liu., Proceedings of Third International Symposium on Electronics Packaging. Beijing Tsinghua University Press, (1998) 2.
3. S. Lagrange, S.H. Brongersma, M. Judelewicz, A. Saerens, I. Vervoort, E. Richard, R. Palmans, K. Maex, Microelectr. Eng. 50 (2000) 449.
4. W. H. The, L. T. Koh, S. M. Chen, J. Xie, C. Y. Li, P. D. Foo, Microelectr. J. 31 (2001) 579.
5. S. H. Brongersma, E. Kerr, I. Vervoort, K. Maex, Proc. AIP Conf., Melville, NY 612 (2002) 229.
6. B. Z. Cui, K. Han, Y. Xin, D. R. Waryoba, A. L. Mbaruku, Acta Materialia, 55 (2007) 4429.
7. A. Ibanez, E. Fatas, Surface & Coatings Technology, 191 (2005) 7.
8. L. Lu, Y. Shen, X. Chen, L. Qian, K. Lu, Science. 422 (2004) 304.
9. W. Dong, J. Zhang, J. Zheng, J. Sheng, Materials Letters. 62 (2008) 1589.
10. J. Reid, S. Mayer, MRS Proceedings of Advanced Metallization Conference, Materials Research Society, Warrendale. PA (2000) 53.
11. K. Pantleon and M. A. J. Somers, J. Appl. Phys. 100 (2006) 114
12. S. H. Brongersma, E. Richard, I. Vervoort, H. Bender, W. Vandervorst, S. Lagrange, G. Beyer, K. Maex, J. Appl. Phys. 86 (1999) 3642
13. J. M. E. Harper, C. Cabral, Jr., P. C. Andricacos, L. Gignac, I. C. Noyan, K. P. Rodbell, and C. K. Hu, J. Appl. Phys. 86 (1999) 2516.
14. K. B. Yin, Y. D. Xia, C. Y. Chan, W. Q. Zhang, Q. J. Wang, X. N. Zhao, A. D. Li, Z. G. Liu, M. W. Bayes, and K. W. Yee, Scr. Mater. 58 (2008) 65.
15. K. B. Yin, Y. D. Xia, W. Q. Zhang, Q. J. Wang, X. N. Zhao, A. D. Li, Z. G. Liu, X. P. Hao, L. Wei, C. Y. Chan, K. L. Cheung, M. W. Bayes, K. W. Yee, J. Appl. Phys.103 (2008) 066 103.
16. R. Huang, W. Robl, H. Ceric, T. Detzel, G. Dehm, IEEE Transactions on Device and Materials Reliability. 10 (2010) 47.
17. Z. Yong, C. Sheng, J. Chen, G. Ding, D. Wen, W. Li, M. Wang, Y. Zhang, Y. Zhang, Thin Solid Films. 460 (2004) 175.
18. D. T. Read, Y. W. Cheng, R. Geiss, Microelectronic Engineering. 75 (2004) 63.
19. S. Cho, I. Chasiotis, T. A. Friedmann, J. P. Sullivan, Journal of Micromechanics and Microengineering. 15 (2005) 728.

Chapter 2 Literature Review

2.1 Nanocrystalline Materials

Nanocrystalline materials are characterised by a microstructural length or grain size up to about 100 nm. Materials having a grain size of ~0.1 to 0.3 μm are classified as submicron or near-nanocrystalline materials. Nanomaterials have experienced a rapid development in recent years due to existing and /or potential applications in a wide variety of technological areas such as electronics, catalysis, magnetic data storage and structural components. To meet the increasing technological demands in these particular fields, the size of the material's structure requires to be reduced to the nanometre scale. For instance, the miniaturisation of functional electronic devices demands the placement or assembly of nanometre scale components into well-defined structures. As the size reduces into the nanometre range, the materials exhibit outstanding physical, mechanical and chemical properties, such as superhardness, extremely high strength, good fatigue resistance, higher wear resistance and enhanced superplastic formability at lower temperature [1-5] (table 2.1).

Table 2.1 The comparison of selected characteristics of copper before and after nanocrystallisation (nanocrystallised grain size 70~200nm) [1-5].

Characteristics	Ultimate Tensile Strength (MPa)	Yield Strength (MPa)	Microhardness (HV)
Conventional coarse-grained copper	228	108	60
Nano-grained copper	280	265	103

The unique properties of nanocrystalline materials are derived from their large number of grain boundaries compared to their coarse-grained polycrystalline counterparts. In nanocrystalline solids, more atoms are associated with grain boundaries than in conventional coarse-grained solids. It has been reported that the fraction of atoms associated with grain boundaries can be as high as 49% in nanocrystalline solid [6]. Thus the grain boundary structure plays an important role in determining the physical and mechanical properties of nanocrystalline materials. For instance, it has been reported that nanocrystalline copper has a much higher electrical resistivity and a larger temperature dependence of the resistivity than conventional micro-grain size copper [7], which were attributed to the large fraction of grain boundary in the nanocrystalline copper enhancing the the scattering of electrons. Nanocrystalline metals have been found to exhibit creep and superplasticity with high strain rates at lower temperatures than their micro-grained counterparts. High strain-rate superplasticity at lower temperatures is of practical interest because it can offer an efficient near-net-shape forming technique to industry. Despite recent advances in the development of nanocrystalline materials, much work remains to be done to achieve a basic understanding of their deformation and fracture behaviours. Nanocrystalline metals generally exhibit significantly higher yield strength and reduced tensile elongation relative to their microcrystalline counterparts. The hardness and yield strength tend to increase with decreasing grain size down to a critical value (~20 nm). When the grain size is below 20 nm, strength appears to decrease with further grain refinement. At this stage, dislocation sources inside the grains are not visable. This implies that dislocation pile-ups cannot form and the Hall–Petch relationship for conventional coarser grained materials is no longer valid. Instead, there is an inverse Hall–Petch effect, i.e. softening is obtained when the grain size is

reduced. The softening behaviour of nanocrystalline materials is a subject of much debate. Several mechanisms have been proposed to explain the anomalous deformation behaviour of nanocrystalline materials with a grain size below the critical value. These include grain boundary sliding, grain-boundary diffusion, the triple junction effect and presence of nanopores and impurities [8, 9]. A comprehensive understanding of the processing-structure–property relationships is essential and helpful in the development of novel nanomaterials with unique properties for structural and functional engineering applications [8-10].

2.1.1 Processing synthesis

Many of the applications of nanomaterials are still in an early stage of technical development. It has been demonstrated that there are still a few issues to be clarified before nanomaterials could be extensively applied into industry, including the synthesis of high purity nanocrystalline materials with large yield economically and environmentally; characterisation of new structures and properties of nanophase materials; fabrication of dense products from nanoparticles with full density and less contamination; retention of the ultrafine grain size in service in order to preserve the mechanical properties associated with the nanometre scale [6]. If nanocrystalline bulk materials could be processed in a cost effective manner and scale sufficient for present structural applications, it is clear that with their special, often superior, properties they might supplant existing conventional grain size materials. However, at the current stage of technological development this is not possible [11]. Due to the thermodynamical instability, most methods for preparing nanomaterials (grain size <100 nm) can manufacture product of relatively small size.

Novel fabrication technology of nanostructured materials is versatile and includes a wide range of vapour, liquid and solid state processing routes. These approaches have been classified into bottom-up and top-down. In the bottom-up approach the materials are arranged into a nanostructure atom-by-atom and layer by layer. In the top-down approach a bulk material is broken down into a nanostructure. The principal synthesis methods are as follows.

Inert gas condensation and compaction can be regarded as a bottom-up method. This technique consists of evaporating a metal inside a chamber containing a partial pressure (typically a few hundred Pascals) of an inert gas. The evaporated atoms collide with the gas atoms inside the chamber, lose their energy and condense in the form of small discrete crystals of loose powder. The condensed fine powders collect on a liquid nitrogen cooled cold finger and are stripped off by an annular Teflon ring into a compaction device. The details of this process and improvements to the original design have been published [12]. While this method provided the materials for the seminal early studies of the properties of nanocrystalline materials, it suffers from both the limited size of samples that can be prepared and from the common problem of two-step methods in that the compaction step may not provide completely dense or bonded material. In addition, contamination of powders and porosity are likely to form due to insufficient consolidation in spite of improvements to the process.

Physical vapor deposition (PVD) is a versatile synthesis method and capable of preparing thin film materials with structural control at the atomic or nanometre scale by carefully monitoring the processing conditions. PVD involves the generation of vapour phase species either via evaporation, sputtering, laser ablation or ion beam

method [13, 14]. In evaporation, atoms are removed from the source by thermal or electronic means; in sputtering, atoms are ejected from the target surface by the impact of energetic ions. In the former case, the vapour phase species that experience collisions and ionisation are condensed onto a substrate followed by nucleation and growth. Thermal evaporation has a limitation in multicomponent materials since one of the metallic elements typically evaporates before the other due to the differences in vapour pressure of the evaporating species [15]. In contrast, sputtering is capable of depositing high melting point materials such as refractory metals and ceramics, which are difficult to fabricate using evaporation. Since the sputtered atoms carry more energy than the evaporated atoms, the sputter-grown films usually have higher density. Owing to the lower purity of the sputtering target materials, sputtered films are more prone to contamination than evaporated films.

Chemical vapor deposition (CVD) is a process where one or more gaseous adsorption species react or decompose on a hot surface to form stable solid products. The main steps that occur in the CVD process can be summarised as:

(a) Transport of reacting gaseous species to the surface.

(b) Adsorption of the species on the surface.

(c) Heterogeneous surface reaction catalysed by the surface.

(d) Surface diffusion of the species to growth sites.

(e) Nucleation and growth of the film.

(f) Desorption of gaseous reaction products and transport of reaction products away from the surface [16,17].

CVD is a more complex method of forming thin films and coatings than PVD. CVD exhibits several distinct advantages such as the capability of producing highly pure and dense films or fine particles at reasonably high deposition rates, and the capability of coating complex-shaped components uniformly due to its non-line-of-sight nature. CVD is widely used for the deposition of metallic, ceramic and semi-conducting thin films. In conventional thermally activated CVD, resistive heating of hot wall reactors provides sufficiently high temperatures for dissociation of gaseous species. This leads to the entire heating of the substrate to a high temperature before the desired reaction is achieved. It precludes the use of substrates having melting points much lower than the reaction temperature. Alternatively, one could heat the reacting gases in the vicinity of the substrate by placing a hot tungsten filament inside the reactor.

Depending on the activation sources for the chemical reactions, the deposition process can be categorised into thermally activated, plasma-assisted and laser-assisted CVD. Plasma-enhanced CVD is known to exhibit a distinct advantage over thermal CVD owing to its lower deposition temperature. Various types of energy resources e.g. direct current, radio frequency, microwave and electron cyclotron resonance microwave (ECR-MW) radiation, can be used for plasma generation in CVD [18]. Laser-assisted CVD is associated with the deposition of chemical vapours using a laser beam generated from sources such as CO_2, or excimer. This process offers deposited films with good quality at a lower temperature with better control of composition and deposition area [19].

Electrodeposition is classified as a "bottom-up" method of preparation of nanocrystalline materials and also as "one-step" since no consolidation step is needed.

Compared with other methods, electrodeposition has its own intrinsic advantages for forming dense nanocrystalline materials: (1) potential for synthesising a large variety of nanostructured materials—pure metals, alloys and composite systems with grain sizes as small as 20 nm; (2) low investment; (3) high production rates; (4) few size and shape limitations; and (5) a high probability of transferring this technology to existing electroplating and electroforming industries. Electrodeposition has been considered to be an effective way to produce bulk nanocrystalline materials, as the thick deposits may still possess a grain size of less than 100 nm [11]. Nanocrystalline deposits are formed on a cathode surface during plating by properly controlling the electrodeposition parameters, e.g. bath composition; temperature and pH. Extensive studies have been carried out on the use of pulsed plating and DC plating for these purposes. Pulsed plating is particularly attractive because it can be used to produce finer-grained structures and coatings that are not obtainable by DC plating. In pulsed plating, current is imposed in a repetitive square wave with the following control parameters: peak current density (peak current/ deposited film area); pulse on-time; pulse-off-time [20-22] (Figure 2.1). El-Sherik and Urb devised a process for producing nanocrystalline Ni having grain sizes in the range 10–40 nm and thickness of 40–50 μm by pulsed electrodeposition from a modified Watts-type bath. The solution consists of nickel sulphate, nickel chloride, boric acid and saccharin inhibitor ($C_7H_4NO_3S$). The deposits generally have an equiaxed structure with fairly narrow grain size distribution (～ 600 nm) [23, 24]. To achieve a significant grain refinement, the pulse-off time must be longer than the pulse-on time (on time: 0.01 - 0.1 s; off time: 0.5 – 2 s) [8, 24]. Grain refiner such as saccharin is generally needed to retard the grain growth of the deposits.

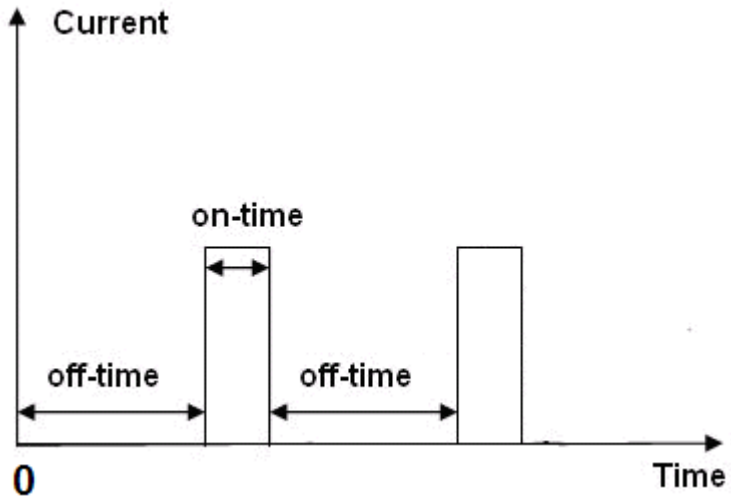

Figure 2.1 Schematic drawing of the controlling parameters of pulsed current deposition.

Mechanical alloying/milling produces nanostructured materials by the structural disintegration of a coarse-grained structure. Mechanical alloying consists of repeated deformation (welding, fracturing and rewelding) of powder particles in a dry high-energy ball mill until the desired composition is achieved. In this process, mixtures of elemental or pre-alloyed powders are subjected to grinding under a protective atmosphere in equipment capable of high-energy compressive impact forces such as attrition mills, shaker mills and ball mills. Figure 2.2 shows the set-up for ball milling. It has been proved that nanometre-sized grains can be obtained in almost any material after a sufficient milling time. The grain size decreases with milling time down to a minimum value that appears to scale inversely with melting temperature. It was suggested by Fecht that localised plastic deformation creates shear bands that show evidence of rotational dynamic recrystallisation similar to that obtained in high-strain rate deformation. The grain size distribution varied from 20 to 200 nm [25-28].

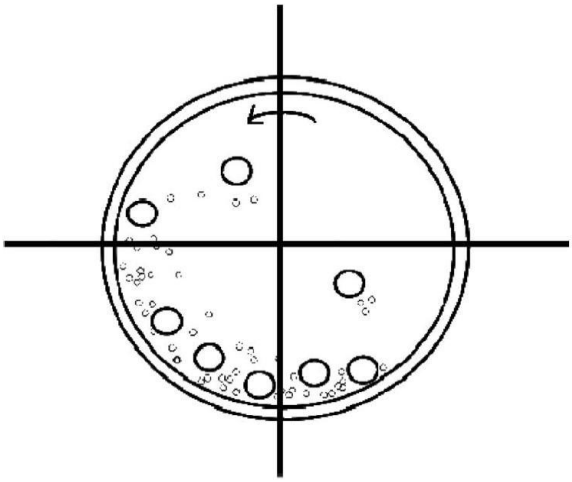

Figure 2.2 The set-up of mechanical milling to produce nanostructured materials.

The possibility of producing very fine grain structures by severe plastic deformation was suggested by research using conventional deformation methods taken to very high degrees of strain [11]. There are two major procedures for severe plastic deformation processing, namely high-pressure torsion (HPT) and equal-channel angular pressing (ECAP). In the HPT process, a sample in the form of a disc is subjected to very large shear torsion straining under an applied high pressure of several GPa at room temperature. One of the sample holders rotates and surface friction deforms the material by shear (Figure 2.3a). In ECAP, the sample is pressed through a die in which two channels, equal in cross section, intersect at an angle φ, with an additional angle ψ defining the outer arc of curvature where the two channels intersect (Figure 2.3b). The sample is pressed through the die using a plunger and subjected to shear as it passes through the shearing plane at the intersection of the two channels. As deformed dimensions are identical to the initial ones, it is possible to repeat this process for many cycles to accumulate large plastic strain. In this regard, ECAP is more attractive than HPT because it can be used to produce not only laboratory samples but bulk submicron-grained billets for industrial applications[100]. Both of these procedures are known to induce a high density of dislocations that

arrange subsequently into metastable subgrains of low-angle boundaries. In pure metals, the application of HPT usually results in the formation of an ultra fine-grained structure with an average size of about 100 nm and ECAP yields a grain size of 200–300 nm. It has been demonstrated that ECAP can successfully produce numerous submicron-grained metallic materials including Ni, Cu, Fe–Cu alloy, Ti alloy, Al and its alloys [29-34].

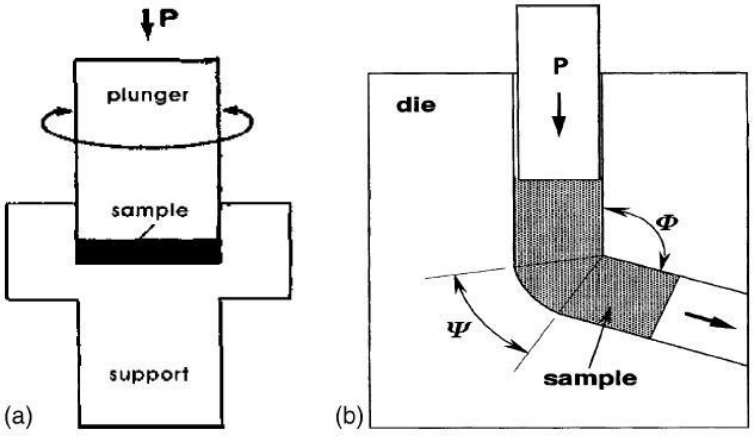

Figure 2.3 Schematic diagrams showing severe plastic deformation methods of forming materials with submicron grain sizes (a) HPT (b) ECAP [30].

In summary, available approaches for the synthesis of nanomaterials via vapour routes range from physical vapor deposition to chemical vapor deposition. Solid state preparation can take place via mechanical milling or electrochemical synthesis. Each method has its own advantages and shortcomings. Among these, electrodeposition and mechanical milling are commonly used to produce bulk nanostructured materials.

2.1.2 Typical microstructure

As mentioned before, nanocrystalline materials are classified as having a microstructural length or grain size of up to about 100 nm. The unique physical and mechanical properties are significantly influenced by the microstructure of the

nanostructural materials. In order to clarify the structure-property relationship, it is necessary to understand the microstructural features of nanocrystalline materials.

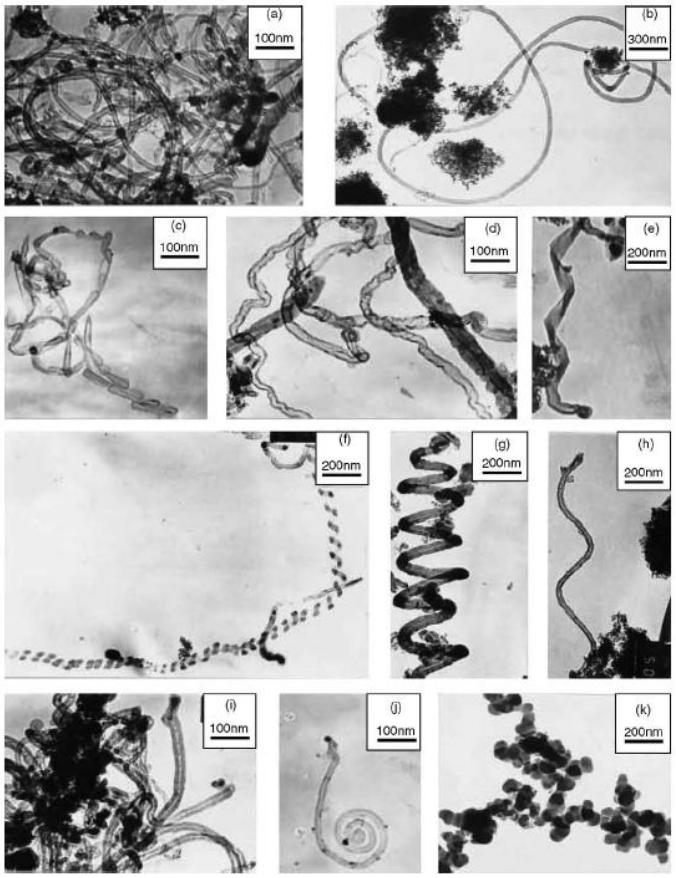

Figure 2.4 TEM images of carbon nanostructures prepared by microwave plasma-enhanced CVD [35].

Figure 2.4 shows a TEM micrograph of carbon nanotubes prepared by MW (Microwave) - CVD using a mixture of CH_4, H_2 and Ar gases. The researcher attempted to use CVD to produce various morphologies of carbon nanotubes by regulating the preparation parameters. However, the mechanisms for the formation of various shapes of carbon nanotubes were not fully explained [35]. Fe, Ni or Co catalysts were used in the CVD. The multi-walled carbon nanotubes consist of a hollow core and coaxial tubes of multiple graphitic sheets. The outer diameters of nanotubes range from 10 to 30 nm and the aspect ratio is in the range of 100 to 1000

(Fig. 2.3a and b). The carbon nanotubes with a circular cross section are smooth and curvy (Fig. 2.3d). Moreover, ribbon-like (Fig. 2.3e), spring-shaped nanotubes with different radii and pitches (Fig. 2.3f and g) as well as necklace-chains (Fig. 2.3k) are also observed. Some black dots are evident in the spring and necklace-shaped nanotubes. They are considered to be nuclei.

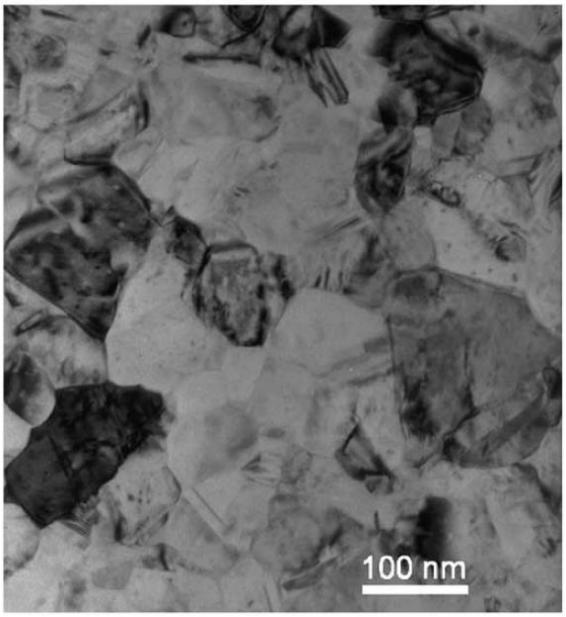

Figure 2.5 A TEM micrograph of pulsed electrodeposited nanocrystalline Ni. (Courtesy of M. Goeken, University of Erlangen, Germany).

Previous research has demonstrated that nano grained-structure Ni could be successfully prepared by pulsed electrodeposition. Figure 2.5 shows a TEM micrograph of a pulsed electrodeposited Ni sample. The average grain size is of 110 nm and no crevice or pore can be observed as shown in the TEM image. Through the measurements at the current magnification, the average grain size can be classified as nanoscale. Processing by HPT has the advantage of producing exceptionally small grain sizes, often in the nanometre range (<100 nm), and has the ability to process brittle materials such as intermetallics and semiconductors.

2.1.3 Mechanical properties

Nanocrystalline materials have a high potential for use in structural and device applications where enhanced mechanical and physical characteristics are required. The mechanical behaviour of nanocrystalline materials has attracted great interest first observed by the pioneers in this field [37], as follows

- Lower elastic moduli than for conventional grain size materials – by as much as 30-50%.
- Very high hardness and strength values for nanocrystalline pure metals（～10 nm grain size): 2 to 10 or more times higher than those of large grained (>1μm) metals.
- Increased ductility – perhaps even superplastic behaviour – at low homologous temperatures, even in normally brittle ceramics or intermetallics with nanoscale grain sizes, believed to be due to the grain boundary, or diffusional deformation mechanisms.

Processing flaws like porosity are known to be detrimental to the properties of nanocrystalline materials. Figure 2.6 shows the Young's modulus as a function of porosity for nanocrystalline Pd and Cu [38]. This decrease in Young's modulus with the increasing porosity has been investigated [39, 40]. The effects of porosity on modulus primarily attribute to the material's bulk density depending on various shaped pores, but the widely recognized theories to explain the relationship of the phenomenon have been found [41].

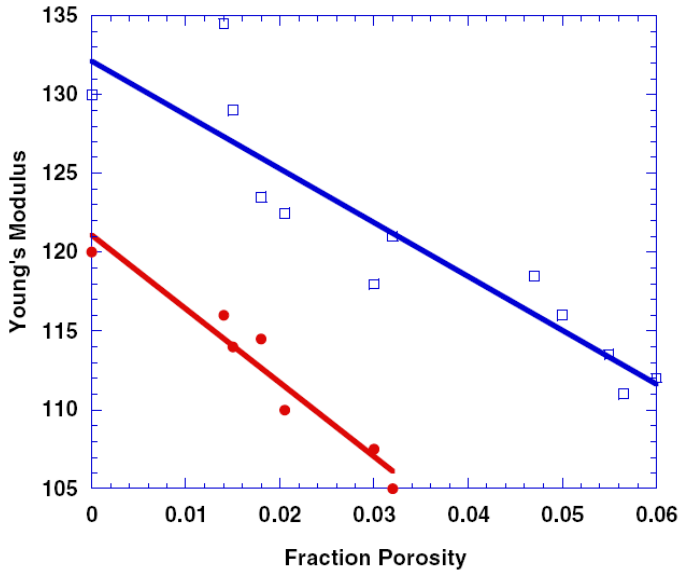

Figure 2.6 Young's modulus as a function of porosity for nanocrystalline Pd and Cu [38].

The plastic deformation behaviour of nanocrystalline materials is strongly dependent on grain size. The empirical Hall-Petch equation provides the relationship between the yield strength of a material and its grain size [42].

$$\sigma_y = \sigma_0 + \frac{K}{\sqrt{d}}$$

Equation 1

σ_y is the yield strength, σ_o is the friction stress below which dislocation will not move in the material (in the absence of grain boundaries) and d is the grain size, while k is a constant. According to this correlation, the yield strength of a material should continue to increase with decreasing grain size, but some measurements indicated that the strength of nanocrystalline metals is significantly lower than predicted by an extrapolation of the equation above to very fine grain sizes.

The study of mechanical strength for most nanocrystalline materials is confined to hardness measurements. Typically the results are displayed as Hall-Petch plots, characterised by Equation 1. A study of the grain size effect on nano-mechanical

properties of copper demonstrated that there was a overally increase in hardness from 1 GPa to about 2.3 GPa with decreasing grain size for refinement from 40 μm to about 43 nm, regardless of the synthesis method. With further grain refinement, especially for electrolessly plated Cu film, with a grain size refinement down to 16 nm, the hardness starts to decrease from 2.1 GPa to 1.1 GPa, which is referred to as the Inverse Hall-Petch Effect which is shown in figure 2.7 [43].

In conventional coarse-grained polycrystalline materials, plastic deformation is mainly governed by lattice dislocations within individual grains [44]. The refinement of grains essentially creates a higher volume of grain boundary in nanocrystalline materials and impedes the dislocation motion and planar glide, resulting in the material being harder to deform further and thus increasing the mechanical strength [43, 45-47].

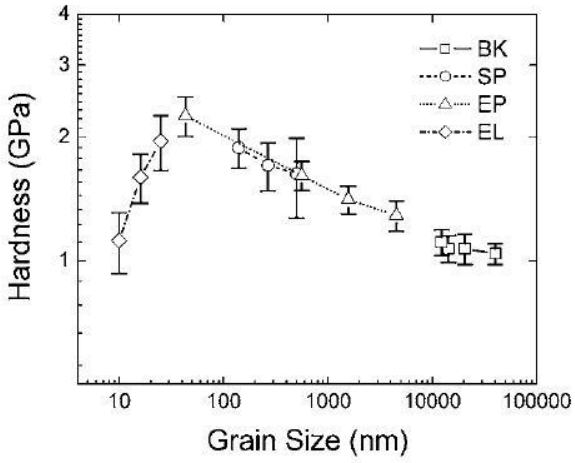

Figure 2.7 Hardness behaviour of bulk Cu (BK), sputtered Cu (SP), electrodeposited Cu (EP) films, and electrolessly plated Cu (EL) films with different grain sizes. Hardness changes with different grain size [43].

2.1.4 Stability issues

Knowledge of the thermal stability of nanocrystalline materials is important for both technological and scientific reasons [11]. From a free energy point of view, the very fine grains which have a large fraction of grain boundary have a tendency to grow in order to reach stabler energy state. From a technological point of view, thermal stability is important for consolidation of nanocrystalline particulates without coarsening the microstructure. Since most consolidation processes involve both heat and pressure, the temperature stability of the nanoscale microstructure is always at risk. The goal of particulate consolidation is to attain essentially 100% theoretical density and good particulate bonding while preventing or minimising growth of the nanocrystalline grains. Understanding the scientific nature of stability and grain growth of nanocrystalline microstructures is necessary for developing a strategy to minimise grain growth. The thermal stability in a broader sense involves not only the stability of the grain structure, that is the microstructure, but also the stability of the structure of the grain boundaries in nanocrystalline materials. In other word, the stability of the grain boundary structure primarily focuses on the fraction change of grain boundary in the total area; grain boundary sliding and defects in the grain boundary. A number of investigations of the thermal stability of nanocrystalline materials have been conducted. Grain growth in nanocrystalline materials has been observed [48-50].

There are two basic ways in which the extent of grain growth can be reduced. The first is the kinetic approach in which the grain boundaries are pinned in various ways to decrease grain boundary mobility. The second is the thermodynamic approach in which the driving force for grain growth is lowered by reducing the grain boundary

energy. In the kinetic approach the grain boundary mobility is reduced by various possible mechanisms, including porosity drag, second phase drag, solute drag, chemical ordering, and grain size stabilisation [51-55]. The thermodynamic approach depends upon the reduction of the grain boundary energy by solute segregation. Since the driving force for grain growth is directly proportional to the grain boundary energy, reducing the grain boundary energy should minimise grain growth. The previous research demonstrated that in the thermodynamic approach, segregation of solute, or impurity atoms to the grain boundaries appears to be an effective method for grain size stabilisation [56-59].

In summary, nanostructured materials have attracted increasing scientific and technological interest due to their unique properties. Nanocrystalline materials can be processed via various ways, and the featured nano-scale grain size can clearly improve their mechanical responses. The stability issues can cause microstructure evolution and thus influence the mechanical performance. Stability is still an important limitation to the use of nanocrystalline materials.

2.2 Electrodeposition Processing

2.2.1 Structural overview

Electrodeposition is primarily an oxidation-reduction electrochemical reaction. It uses electrical current to reduce cations of a desired material from a solution and coat a conductive object with a thin layer of the material. Specifically metals or alloys are deposited onto an electronically conductive surface from an electrolyte containing the metal ions. Electrodeposition is mainly used for depositing a layer of material to inherit a desired property to a surface that otherwise lacks that property. The properties of the deposits are dependent on their microstructure, which in turn is influenced by the deposition/processing parameters, such as electrolyte composition, pH, electrodeposition temperature and current density [60].

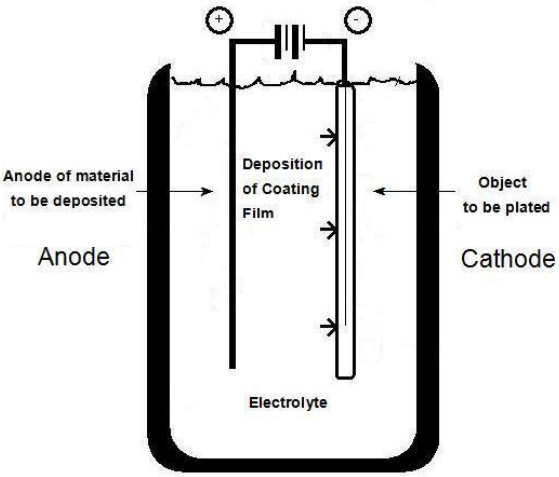

Figure 2.8 Schematic illustration of the copper electrodeposition cell

The electrodeposition process itself consists of a power source, either a constant power or pulsed power source to supply current to flow in one direction when a potential difference is imposed across the system. The cathode, where the metal or alloy is deposited, can either be a metal, a semiconductor, or a non-metallic conductor

such as graphite, while the anode is present primarily to complete the electrical circuit and to remove the negative ions, thus maintaining overall charge neutrality in the solution [61]. The anode can also serve to maintain a constant supply of fresh metal to replace that removed from the electrolyte by the deposition on the cathode. In the case of copper deposition, these are referred to as sacrificial anodes, which were made of the same metal being deposited. High purity copper plate is used as sacrificial anode and dissolves anodically to release copper ions into the electrolyte [61]. When a voltage is applied across the two electrodes, electrons flow from the anode through the external circuit and back to the cathode. The sacrificial anode will thereby dissolve anodically, forming cations which migrate to the cathode while the anions present in the electrolyte move in the opposite direction towards the anode [61, 62, 63]. This process is illustrated in Figure 2.8 above.

It has been stated that the two most important mechanisms which are rate determining steps for formation of nanoscale grains in electrodeposition are charge transfer at the electrode surface and surface diffusion of adions on the crystal surface [47]. Since high overpotential favours extensive nucleation, pulse plating, as a powerful method to achieve high overpotential is a technique to synthesise a nanocrystalline structure without the use of additives. Another method to inhibit growth of nucleated crystallites is by reducing the surface diffusion of adions by adsorption of foreign species (which may be referred to as “grain refiners” or “additives”) on the growing surface. Therefore, there are several processing strategies that can be used to provide artifact-free bulk nanocrystalline materials by electrodeposition. Some of the bulk nanocrystalline electrodeposited examples exhibit optimized combinations of strength and ductility with their stable microstructures.

2.2.2 Deposition parameters of copper

As mentioned before, the microstructure of a deposit is dependent on the various deposition/processing parameters [60]. In order to satisfy the particular property needs of copper films, it is necessary to choose appropriate deposition parameters prior to carrying out electro-deposition. The electro-deposition parameters are generally considered to consist of the electrical power type and its parameters, solution composition, pH, temperature and current density.

Electrodeposition has been reported using a constant power supply at 0.6 V. The solution contained not only the conventional copper sulphate but also $InCl_3$, $GaCl_3$ and H_2SeO_3 with a pH of 2.4 at room temperature. In order to improve the adhesion between the thin film and the substrate, while decreasing the residual internal stress of the deposits, the thin film after deposition was annealed to further remove the residual stress using flowing H_2S at 500 ℃ for an hour [64].

TiN film is commonly deposited as a buffer layer on the substrate prior to copper thin film electrodeposition [65]. Morisue used a constant power supply to produce copper thin films in a solution mainly containing high-grade copper sulphate. The electrolyte was de-aerated for 2 hours by bubbling through nitrogen gas in order to get high quality copper thin film without obvious voids optically [65]. Oskam demonstrated that electro-deposition using a silicon wafer substrate (n-Si 100) with a TiN buffer layer was successful in obtaining a nanocrystalline copper thin film [66]. The TiN layer was radio frequency sputter deposited at room temperature onto a silicon wafer substrate for 1 min. The aqueous solution included $CuCO_3$ $Cu(OH)_2$, H_3BO_3 and HBF_4. The pH value of the solution was about 1.4. Constant power was applied at a potential of 0.22

V [66]. The experiment confirmed that TiN buffer layer can be successfully applied into copper electrodeposition in the strong acid environment, but the substrate's pre-treatment was needed.

Some experiments were carried out using a multi-buffer layer placed between the copper thin film and substrate. A silicon wafer substrate was pre-coated with TiN and Ti, but a power supply was not used in this copper deposition. The solution composition mainly included $CuCl_2$ (175 g), $CoNO_3$ (6 g), HNO_3 (30 ml (69%)), ethylene diamine (2 g) and distilled water (812 g). The pH of the electroless deposition solution was 6.8. After deposition, the deposits were rinsed with deionised water and dried in an N_2 stream. Two TEM samples were prepared to carry out cross-sectional observations. One was annealed at 400 $^{\circ}C$ for 30 minutes after electrodeposition, the other was not. TEM results demonstrated that the adhesion between the deposited film and substrate was much improved by the annealing compared with the other sample which has not been annealed, as the waved-shape gap between the film and substrate was not obviously found after annealing [67].

Some of the publications do not include detailed deposition parameters. The electrolyte commonly contains Cu^{2+}, Cl^- and acid with different additives in order to achieve different properties of the deposits. Some of the experiments used copper seeds or electro-less deposition to achieve an appropriate buffer barrier prior to electro-deposition. The principle of using a seed layer is that electro-deposition onto a continuous seed layer allows the deposition of an initial layer without voids; otherwise with a discontinuous seed layer, the subsequent electro-deposited layer contained more defects and had a lamellar structure. Also poor adhesion of the seed

layer caused peeling of the thin film from the substrate surface during the planarisation process [68]. The treatment after electro-deposition varied depending on which property of the deposited copper foil was preferred. Pickling, which was used for activation prior to electro-deposition, was preferred, especially for brass substrates. As the adhesion strength was important for further mechanical testing, annealing after electro-deposition (at 300 - 400 ˚C lasting less than 30 minutes) [67, 68] was necessary to achieve better adhesion.

Recent research focusing on direct current electrodeposited Cu has indicated that the copper films with an average grain size ranging from 0.3-1.4 μm can be obtained with a current density ranging from 3.5-250 mA/cm^2 [69, 70]. It has been recognised that the applied current density was one of the key parameters in determining the grain size of the DC electrodeposited copper [70]. For pulsed current electrodeposited Cu, several researchers have reported that by adjusting the peak current density or the pulsed current waveform, copper films with an average grain size ranging from 0.1-0.5 μm can be obtained with a current density ranging from 5-500 mA/cm^2 [70-72]. Some investigations have examined the on-time effect on microstructure [71]. A finer grain structure and stronger texture of electrodeposited copper was achieved with shorter on-time. The off-time was theoretically believed to constitute the particular stress relaxation time with recrystallization and grain growth [71].

In conclusion, the potential for copper deposition is below 1 V, and the solutions mainly consisted of copper sulphate with a pH of around 1 to 2 with some additives (Cl^-). Room temperature was often used. Pre-treated activation was preferred for the substrate prior to electrodeposition and annealing was often used to decrease the

residual stress of the Cu deposits. Copper films with enhanced properties can be achieved by PC deposition rather than DC deposition. Some investigations have concerned the effect of the deposition parameters of PC prepared Cu films. Off time pf PC deposition is one of the important processing parameters, and is generally regarded as recrystallisation and grain growth time. However, the off-time effect on determining the resultant microstructure of copper films has not been particularly/fully examined yet.

2.2.3 Substrate explorations of Cu deposits

Substrates may have an effect on the microstructure and adhesion strength of a Cu deposit [60, 64-66]. So, prior to the electrodeposition, it is necessary to choose the appropriate substrate.

Soda-lime with Co has been used as a substrate. A Co layer with a thickness of 10-15 nm was employed as a buffer layer deposited onto crystalline Soda-lime. It has been demonstrated that the adhesion between Cu film and substrate was much improved with Co layer deposited onto a soda-lime substrate [64]. The grain size was found to have a large range from 600 nm to 2100 nm, and the deposition date was relatively lower (16 ± 2 nm/min) using Soda-lime as substrate [64]. Stainless steel sheet was used with TiN pre-coating. The stainless steel sheet was thoroughly clean and the TiN film was sputtered onto it with a thickness of 100-200 nm [65]. It was found that the relatively bulk deposits can be fabricated without obvious change of microstructure among layers [65].

TiN film as a buffer layer is widely used as a barrier material in copper metallisation as well as in aluminum-based metallisation [73, 74]. Copper is known to have high diffusivity in silicon [75]. TiN film had micron grain size and a dense grained structure which effectively prevented copper diffusion into the substrate. Even at elevated temperature, the TiN was still an effective diffusion barrier [76]. Another important reason for the frequent use of TiN pre-coating is that TiN film is non-electrically conductive, but the copper film has good electro-migration ability and enhanced mechanical strength, so the overall layout, with a TiN coating underneath and copper film above, satisfies the structural needs of IC devices.

A number of researchers used silicon wafers (n-Si 100) in Cu electrodeposition, the deposited films were demonstrated to only have (100) texture [66]. Some investigations indicated that steels, especially ferritic steels, used as a substrate needed no pre-coating to produce relatively thick copper film [77]. The Chinese Academy of Sciences reported that nanocrystalline copper films were extensively prepared using pulsed electro-deposition onto a pure Fe sheet substrate [64]. A ferritic stainless-steel sheet with Au-nickel (3 wt%) coating was also a successful substrate for copper film electro-deposition [78]. Brass and bulk silver were also reported to be usable as substrates for electrodeposition [78, 79].

In summery, different substrates were reported to have effects on the growth rate, grain size and adhesion of the electrodeposited copper films. A silicon wafers with TiN pre-coating are initially preferred because of manufacturing needs in industry but the films have strong texture dependence on substrate. However, compared to other substrates such as brass and steel, pre-coating prior to electrodeposition requires a

more complicated and costly process. Ferritic steel as a substrate is inexpensive and did not require complicated pre-coating. But pre-treatment like electropolishing, a Ni-P coating for “activation” is still necessary. The resultant microstructures of the films do not have clear substrate’s dependence but depending on the deposition parameters.

2.3 Electrodeposited Cu Film

2.3.1 Overview

It has been suggested in the previous review that electrodeposition yields grain sizes in the nanometre range when the electrodeposition variables are chosen such that the nucleation of new grains is favored rather than growth of existing grains. This is achieved by using high deposition rates, formation of appropriate complexes in the bath and addition of suitable surface-active elements to reduce the surface diffusion of ad-atoms [80]. This technique can yield porosity-free finished products that do not require subsequent consolidation processing. Furthermore, this process requires low capital investment and provides high production rates with few shape and size limitations.

2.3.2 Microstructure of Cu films

The microstructure of an electro-deposited copper film is dependent on the various deposition parameters and the mechanical properties of the film are determined by its microstructure. So before investigations are carried out, it is necessary to clarify the relevant films microstructure. Here, the microstructure of nanocrystalline Cu prepared by consolidation is illustrated below, in order to clarify the relevant microstructure of nanostructured Cu using different processing.

Figure 2.9 shows a TEM image of consolidated nanocrystalline Cu. The statistical distribution of grain sizes (More than 600 grains were used to do the statistics) can be seen from (b), which indicates that the narrow range of grain size of nanocrystalline

Cu film with average 19 nm in size [81]. Recent results by Shen and Lu indicated that a highly twinned structure can be produced under the appropriate electrodeposition condition. This high annealing twin density is responsible for the enhancement of ductility [82, 83]. The typical microstructure of a highly twinned structure which prepared by pulsed electrodeposition is shown in figure 2.10, which indicated that most of the grains were roughly equiaxed in three dimensions with an average 400 nm in size and 5 μm in thickness..

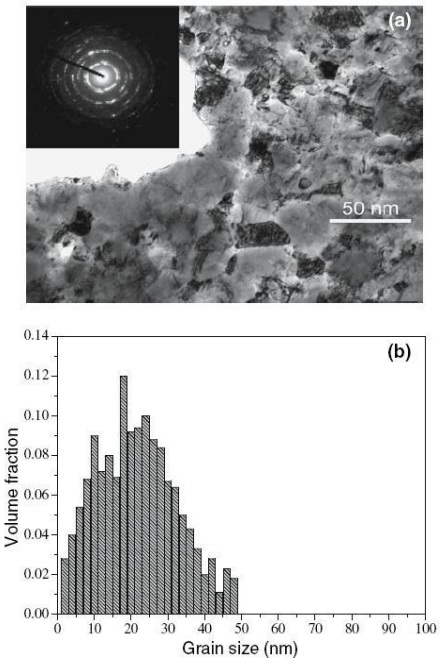

Figure 2.9 TEM observations of a typical microstructure in an in situ consolidated nanocrystalline Cu. The bright-field TEM micrograph (a) and the SADP [the upper left inset in A] show roughly equiaxed grains with random orientations. The statistical distribution of grain size (b) was obtained from multiple dark-field images of the same sample [81].

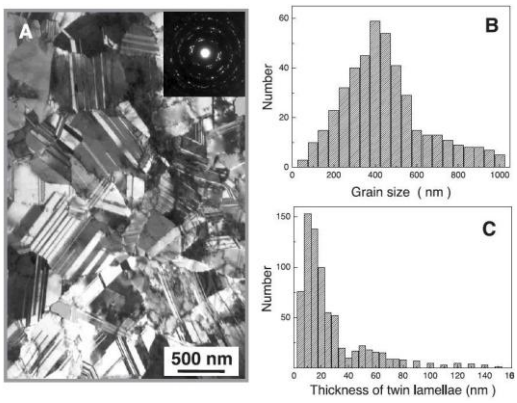

Figure 2.10 TEM observations of the typical microstructure in an as-deposited Cu sample. A bright-field TEM image (A) and the electron diffraction pattern (inset) show roughly equiaxed submicronmetre–sized grains with random orientations. Grain size statistical distributions (B). Thickness of the twin/lamellae (C) [82].

Figure 2.11 shows a cross sectional bright field image of a freshly electrodeposited Cu thin film. It was prepared by DC deposition. In the cross-section, TEM investigations revealed a partially columnar but more fine-grained microstructure throughout the whole Cu layer. The researcher indicated that the mean grain size was 86 nm [84].

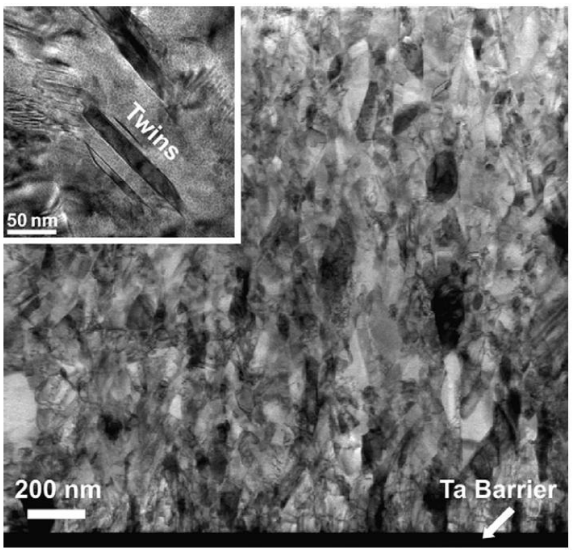

Figure 2.11 TEM bright field image of a 2000 nm electrodeposited Cu thin film in cross-section [84]

2.3.3 Mechanical properties of nanocrystalline Cu films

2.3.3.1 Micro-hardness

Hardness is an important mechanical property of the metallic film since it is related to the strength or fracture toughness of the specimen. A high hardness value usually corresponds to high abrasive wear resistance [85]. However, this definition of hardness is based on the contact area under load, which may deviate from traditional hardness measurements based on the area of the residual hardness impression, especially if significant elastic recovery during unloading occurs [85, 86]. This is because the residual area is relatively small for purely elastic contact, thus giving a closely infinite hardness measurement based on the traditional definition.

$$H = \frac{P_{\max}}{A}$$ **Equation 2**

P max is the maximum applied load, and *A* is the projected indenter contact area. In general, hardness usually implies a resistance to deformation, and for metals the property is a measure of their resistance to permanent or plastic deformation [87]. In the current study, *P* max is the maximum load of nano-indenter applied onto the film surface, *A* is the projected indenter contact area on the copper film surface.

2.3.3.2 Micro-tensile strength

Strength is one of the most important mechanical properties of materials. In metallurgy, strength refers to the material's ability to withstand an applied stress without failure. Yield strength refers to the point on the engineering stress-strain curve beyond which the material begins deformation that cannot be reversed upon removal

of the load. Ultimate strength refers to the point on the engineering stress-strain curve corresponding to the maximum stress [88].

While nano-scale grains have been the focus for increasing strength in studies of nanocrystalline materials, Lu has reported that the grain size of electro-deposited copper was of the order of 400-500 nm, the outstanding mechanical properties primarily attribute to the nano-grained structure [82]. Meanwhile, the twin structure also optimizes the properties of the copper films. Twin boundaries can also be an effective obstacle to dislocation motion and a potent strengthener [82]. The yield strength of the Cu followed Hall-Petch behaviour with increased strength as twin lamellar spacing decreased [83]. The experimental data for the tensile strength of coarse-grained copper, nanocrystalline copper and nanocrystalline twinned copper are as follow in figure 2.12 and figure 2.13.

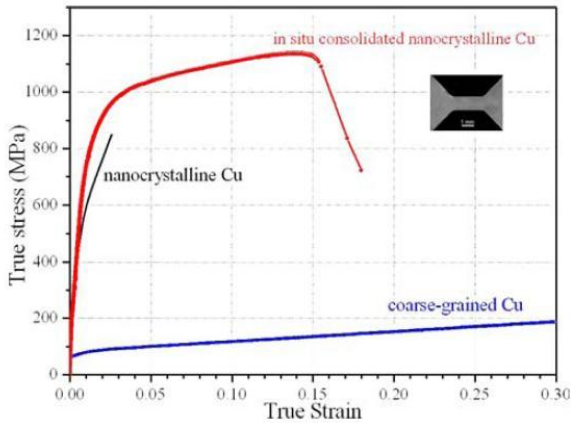

Figure 2.12 Stress–strain curves for in-situ consolidated nanocrystalline Cu, nanocrystalline Cu made by inert gas condensation, and coarse-grained Cu [81].

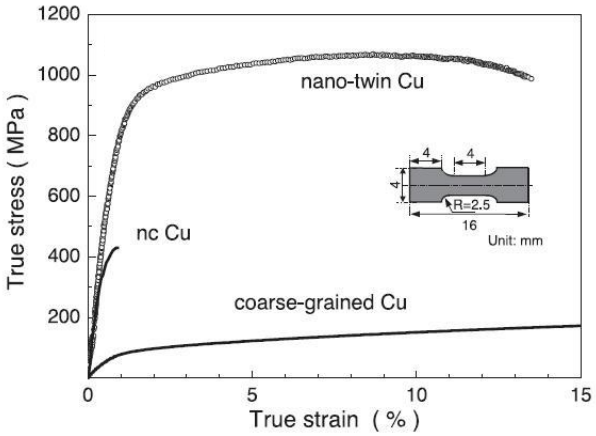

Figure 2.13 A typical tensile stress-strain curve for an as-deposited Cu sample with nano-twins in comparison with that for a coarse-grained polycrystalline Cu sample (with an average grain size larger than 100 μm) and a nanocrystalline (nc) Cu sample (mean grain size 30 nm). The inset shows the geometry of the tensile sample for the as-deposited nano-twin sample (R, radius of curvature) [82].

2.3.4 The influence of electrodeposition parameters

Aqueous processing of Cu by pulse electroplating has been reported in literatures, in which researchers have mentioned the capability of generating nanostructures in terms of either nanocrystallite size or nanotwinned grains [100,101]. Three parameters are independently variable in practical pulse plating: pulse peak current, on time and off time, which determine the physical characteristics of the deposits obtained from the given electrolyte. A research carried out by Xi Zhang[102] shows a stronger (110) texture was obtained with increasing the pulse current density, that the higher energy pulses would cause stronger texture due to stonger self-annealing, while lower energy ones lead to more random texture. And high density of nanotwins was observed as a result of pulse plating with applied peak current densities in the medium to high range. A. Balasubramanian, D. S. Srikumar, G. Raja, G. Saravanan and S. Mohan [103] studied the influences of pulse duty cycle and pulse frequency on the thickness and current efficiency of copper deposited , it was found that at 80% duty cycle and 50 Hz, a maximum thickness and current efficiency were given for the author's experimentations.

2.3.5 Deformation mechanisms in nanocrystalline films

Nanocrystalline films demonstrate enhanced mechanical properties which are related to the specific deformation mechanisms in these films [45]. The deformation of nanocrystalline films can also be explained by the Hall-Petch effect, where conventional dislocation slip dominates for grain sizes above a critical grain size of 10-30 nm, depending on the material and its structure. For very small grain size (below the critical grain size), the deformation mechanisms associated with the active role of grain boundaries dominate, reducing the yield strength with further refinement of grain size [43, 45-47].

2.3.6 Self-annealing

An important feature of electrodeposited Cu affecting its microstructure is self-annealing, or room-temperature recrystallisation after deposition [89, 90]. The recrystallisation of as-electrodeposited copper at room temperature, which is termed self-annealing, is a very distinct phenomenon [91]. It has been reported that during the recrystallisation, resistance, stress and texture in copper films change dramatically at room temperature [91, 92]. For example, the electrical resistance of electrodeposited copper can be one third after ten days at room temperature storage compared with the fresh sample. Even the texture of the films can be changed from (111) to (110) within five days at room temperature. During the last decade, an intensive amount of research has been devoted to studying direct current electrodeposited Cu thin films. The most interesting finding is that microstructural evolution or self-annealing occurs

at room temperature. That is to say, the DC electrodeposited Cu film transforms itself to a larger-grained structure over a period of hours or days after deposition [93, 94].

From the various published literature, self-annealing occurred mainly in DC electrodeposited copper films with a thickness range of 1.5-14 μm [91, 92, 95]. Transmission electron microscopy (TEM) and Focused Ion Beam (FIB) microscopy were most frequently used to investigate the microstructural evolution. The drawback of TEM is the limited observable area, and sample preparation is more complex. Larger areas can be observed using FIB microscopy and this technique does not need a long time for sample preparation if it has been properly electropolished. TEM and FIB evidence of microstructural evolution of DC electrodeposited copper films is shown in figure 2.14 and figure 2.15, respectively. Furthermore, it has been postulated that ion bombardment in a FIB microscope can lead to grain growth in Cu and Au thin films [96]. Grains that are oriented for channeling with respect to the incident beam grow at the expense of the other grains [96]. However, the effect of ion beam bombardment on copper grains will be examined in the present study.

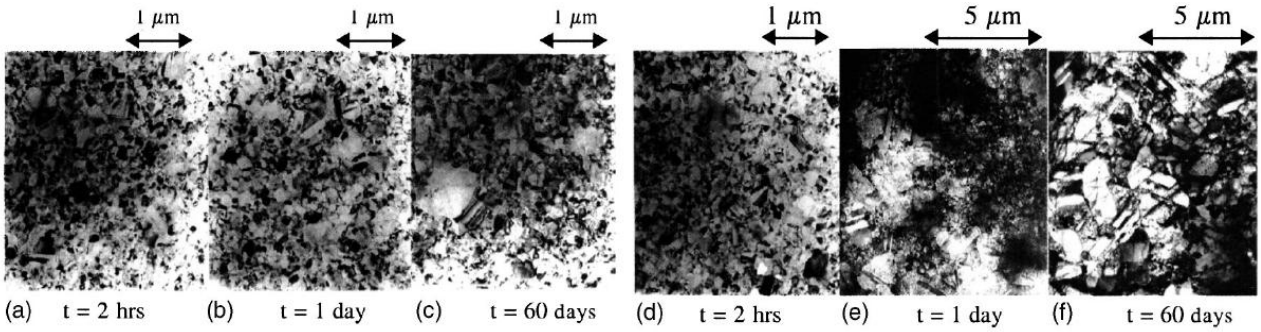

Figure 2.14 TEM grain images as a function of time for Cu films dc-plated; (a), (b), (c): at 5 mA/cm^2; (d), (e), (f): at 10 mA/cm^2 [90].

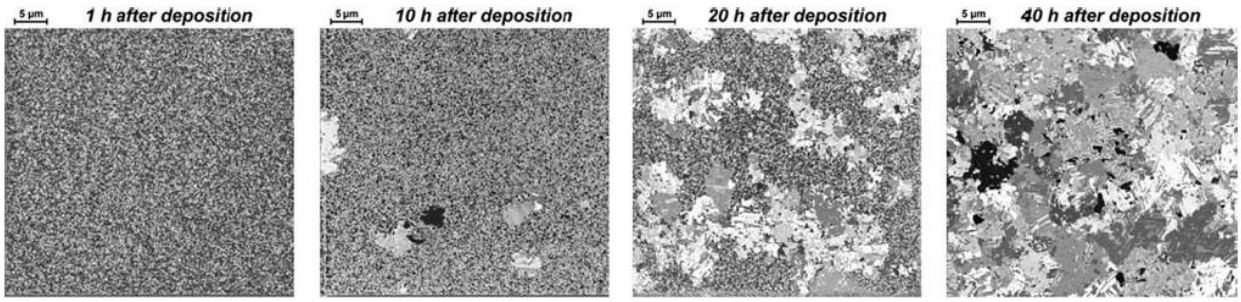

Figure 2.15 Microstructure evolutions during self-annealing of a 1000 nm thick Cu layer as a function of time [97].

2.4 Nanoindentation

Indentation testing has been used widely to study the elastic modulus and hardness by penetrating the material of interest with another material whose properties are known. With a recent increase in interest in the mechanical properties of thin film systems and small volumes of materials, a conventional hardness tester with penetration depth in the microns or millimetres cannot provide low enough forces to measure the properties of the film without involving the substrate. With nanoindentation, a penetration depth in the range of nanometres is used, from which the hardness and elastic modulus, along with other mechanical properties such as wear resistance, can be derived during one cycle of loading and unloading [85].

2.4.1 Test cycle and P-h curve

A typical nanoindentation test cycle consists of an application of load followed by an

unloading sequence and either maximum load or displacement can be specified, as illustrated in Figure 2.16. Two control parameters that can be applied during the indentation test are either constant loading rate or constant strain rate (The rate of change in strain with respect to time). At each load increment and at maximum load, a hold period is allowed for the instrument and specimen to stabilize before depth and load readings are taken while a hold period at maximum load can be used also to measure the creep within the specimen [85]. Furthermore, a hold period for thermal drift is usually carried out at the end of the indentation test, at low load (usually about 10% of maximum load), to minimize the effect of creep within the material [85]. During this period, the change in dimensions of the instrument due to thermal expansion or contraction of the apparatus is measured. The thermal drift rate can then be computed and the depth readings taken throughout the test are adjusted accordingly.

The four important parameters measured during the indentation test include the maximum load, P_{max}, the maximum displacement, h_{max}, the final or residual depth after unloading, h_f, and the elastic unloading stiffness or contact stiffness which is the slope of the upper portion of the unloading curve during the initial stage of unloading, defined as $S=dP/dh$. The measurement of hardness and elastic modulus in nanoindentation is based on the unloading process and a schematic illustration of the penetration depth appears in figure 2.17. As the indenter is driven into the material, both elastic and plastic deformation occurs, causing the formation of a hardness impression that conforms to the shape of the indenter at the contact depth, h_c. When the indenter is withdrawn, only the elastic portion of the displacement is recovered, leaving a residual impression on the surface of the specimen from the plastic deformation [85, 86, 98, 99].

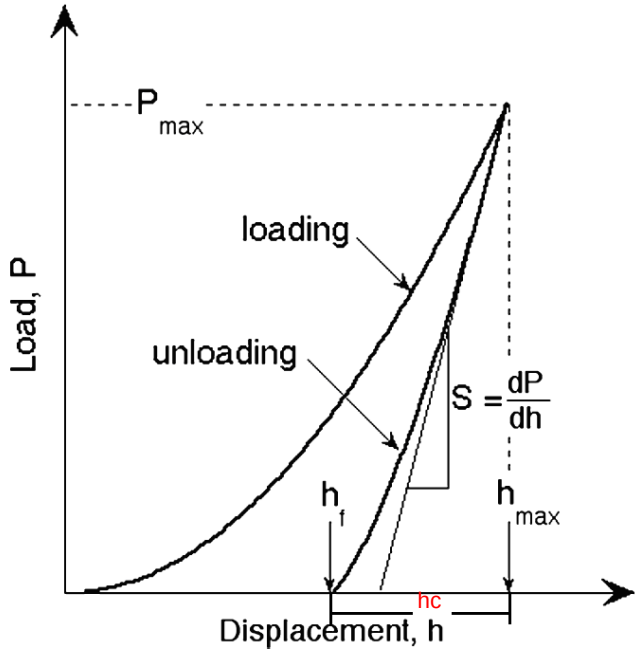

Figure 2.16 Schematic illustration of load – displacement data set showing a typical test cycle and highlighting the important measurable parameters [86]

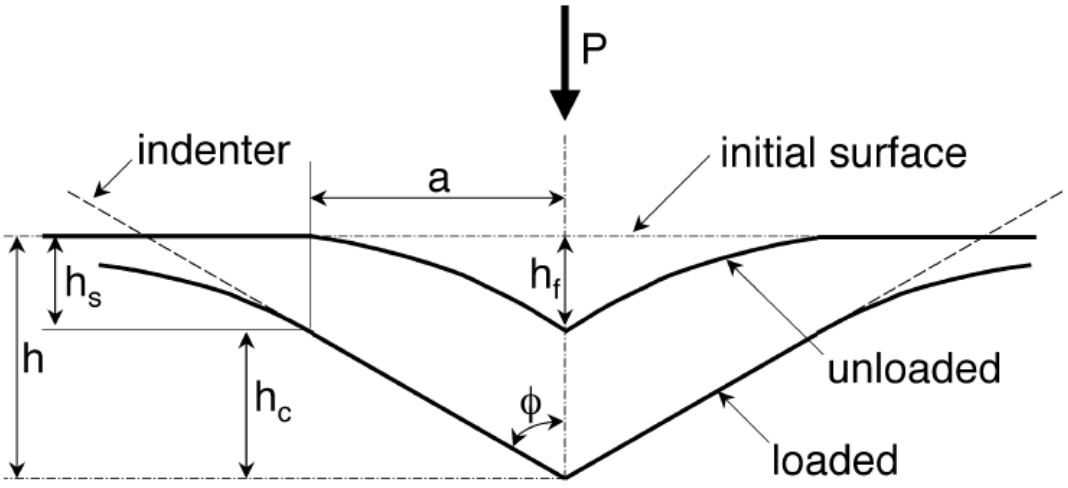

Figure 2.17 Schematic diagram of the penetration depth, showing the important parameters for contact geometry determination [86]

2.5 Summary of Literature Survey

Copper films prepared by direct current electrodeposition have been studied for a longer time than those prepared by pulsed current electrodeposition. PC deposition is more likely to produce copper films with enhanced properties due to the finer-grained structure. Research interest has been paid to study the effect of current density and substrate selection to the microstructure of the electrodeposited copper films, but effect of off-time in a pulsed cycle has not been examined, deriving which was recognized to take place recrystallisation and grain growth. Self-annealing was found in DC electrodeposited copper films with 1.5-14 μm thickness. Bulk nanocrystalline materials have attracted scientific and industrial interest, but the stability of bulk DC copper deposits（～80 μm) has not been investigated.

References

1. M. C. Roco, R. S. Williams, P. Alivisatos, Nanotechnology research directions. U.S. National Science and Technology Council, Washington, D.C. 2000.
2. G. M. Chow, I. A. Ovid'ko, T. Tsakalakos, Nanostructured films and coatings. 2000.
3. H. Gleiter, Acta Materialia**.** 48 (2000) 1.
4. S. Komarneni, R. A. Vaja, G. Q. Lu, J. I. Matsushita, J. C. Parker, Nanophase and nanocomposite materials IV. MRS symposium proceedings, vol. 703. 2003.
5. C.C. Berndt, T. Fischer, I. A. Ovid'ko, G. Skandan, T. Tsakalakos, Nanomaterials for structural applications. MRS symposium proceedings, vol. 740. 2003.
6. S.C. Tjong, Haydn Chen, Materials Science and Engineering R. 45 (2004) 1.
7. Y.K. Huang, A.A. Menovsky, F.R. de Boer, Nanostructure Materials. 2 (1993) 505.
8. Y. Sun, Y. Xia, Science. 298 (2002) 2176.
9. A. A. Federov, M. Yu Gutkin, I.A. Ovid'ko, Acta Materialia. 51 (2003) 887.
10. H. Wrzesinska, J. Ratajczak, K. Studzinska, J. Katckj, Materials Chemistry and Physics. 81 (2003) 265.

11. C. C. Koch, Journal of Materials Science. 42 (2007) 1403-1414.
12. R.W. Siegel, R.W.Cahn, P.Haasen, E.J.Kramer, Materials science and technology. 15 (1991) 583.
13. N. Guillou, L.C.Nistor, H. Fuess, H. Hahn, Nanostructure Materials. 8 (1997) 545.
14. T. Haubolt, R. Bohn, R. Birringer, H. Gleiter, Materials Science and Engineering. 153 (1992) 679.
15. J. C. Sanchez-Lopez, A. Justo, A. Fernandez, Philosophical Magazine B. 76 (1997) 663.
16. M. L.Hitchman, K. F.Jensen, Chemical Vapor Deposition—Principles and Applications. Academic Press. London. 1993.
17. A. Sherman, Chemical Vapor Deposition For Microelectronics—Principles, Technology and Applications, Noyes Publications, New Jersey, 1987.
18. J. Y. Seo, S. Y. Yoon, K. Niihara, K.H. Kim, Thin Solid Films. 406 (2002) 138.
19. P. Heszler, L. Landstrom, M. Lindstam, J.O. Carlsson, Journal of Applied Physics. 89 (2001) 3967.
20. C.B. Wang, D.L. Wang, W.X. Chen, Y.Y. Wang, Wear. 253 (2002) 563.
21. F. Ebrahimi, G.R. Bourne, M.S. Kelly, T.E. Matthews, Nanostructure Materials. 11 (1999) 343.
22. H. Li, F. Ebrahimi, Materials Science and Engineering A. 347 (2003) 93.
23. U. Erb, A.M. El-Sherik, US Patent 5,352,266 (1994).
24. A.M. El-Sherik, E. Erb, Journal of Materials Science 30 (1995) 5743.
25. C.Suryanarayana, Progress in Materials Science. 46 (2001) 1.
26. H. J. Fecht, E. Hellstern, Z. Fu, W.L. Johnson. Metallurgical and Materials Transactions A. 21 (1990) 2333.
27. J. Eckert, J.C. Holzer, C.E.Krill, W. L. Johnson. Journal of Materials Research. 7 (1992) 1751.
28. H. J. Fecht. Nanophase materials. 260 (1994) 125.
29. L.S. Toth, Advanced Engineering Materials. 5 (2003) 308.
30. K. Neishi, Z. Horita, T.G. Langdon, Materials Science and Engineering A. 325 (2002) 54.
31. S. Komura, Z. Horita, M. Nemoto, T.G. Langdon, Journal of Materials Research. 14 (1999) 4044.
32. R. Z. Valiev, I. V. Alexandrov, Nanostructure Materials. 12 (1999) 35.
33. V. A. Teplov, V. P. Pilugin, V. S. Gaviko, E. G. Chernyshov, Nanostructure Materials. 6 (1995) 437.
34. R.S. Mishra, V.V. Stolyarov, C. Echer, R.Z. Valiev, A.K. Mukherjee, Materials Science and Engineering. 298 (2001) 44.
35. X. Wang, Z. Hu, X. Chen, Y. Chen, Scripta Materialia. 44 (2001) 1567.
36. A. P. Zhilyaev, G. V. Nurislamova, B. K. Kim, M. D. Baro, J. A. Szpunar, T. G .Langdon, Acta Materialia. 51 (2003)753.
37. H. Gleiter, Progress in Materials Science. 33 (1989) 223
38. P. G. Sanders, J. A. Eastman, J. R. Weertman, Acta Materialia. 45 (1997) 4019.
39. J. B. Wachtman, Mechanical and thermal properties of ceramics. NBS

Washington: NBS Special Publication, (1963) 139.
40. J. K. MacKenzie, Proceedings of the Physical Society. 63 (1950) 2.
41. J. Youngdahl, P. G. Sanders, J. A. Eastman, J. R. Weertman, Scripta Materialia. 37 (1997) 809.
42. T. H. Countney, Mechanical behaviour of Materials (McGraw-Hill, New York, NY, 1990), pp. 80-136, and 263-324
43. S. Y. Chang, T. K. Chang, Journal of Applied Physics. 101 (2007) 033507.
44. J. Chen, L. Lu, , Y. F. Shen, S. Suresh, Acta Materialia, 54 (2006) 5421
45. A. Caveleiro, and J.T.M.D.Hosson, eds. Nanostructure Science and Technology. Nanostructured Coatings. 2006, Springer.
46. C. H.Seah, S. Mridha, L. H. Chan, Journal of Materials Processing Technology. 89 (1999) 432
47. U. Erb, K. T. Aust, G. Palumbo In: Koch CC, Nanostructured materials: processing, properties, and applications. William Andrew Publ., Norwich, NY, 179 (2002).
48. C. Suryanarayana, International Materials Reviews. 40 (1995) 41.
49. J. Weissmuller, D. L. Bourell, Synthesis and processing of nanocrystalline powder.TMS,Warrendale, PA, (1996) 3
50. T. R. Malow, C. C. Koch, D. L. Bourell Synthesis and processing of nanocrystalline powder. TMS, Warrendale,PA, (1996) 33
51. H. J. Hofler, R. S. Averback, Scripta Metall Mater. 24 (1990) 2401.
52. K. Boylan, D. Osstrander, U. Erb, G. Palumbo, K. T. Aust, Scripta Metall Mater. 25 (1991) 2711.
53. A. Michels, C.E. Krill, H. Ehrhardt, R. Birringer, D.T. Wu, Acta Materialia. 47 (1999) 2143.
54. Z. Gao, B. Fultz, Nanostructure Materials. 4 (1994) 939.
55. C. E. Krill, L. Helfen, D. Michels, H. Natter, A. Fitch, O. Masson, R. Birringer, Physical Review Letters. 86 (2001) 842.
56. J. Weissmuller, Nanostructure Materials. 3 (1993) 261.
57. J. Weissmuller, Journal of Materials Research. 9 (1994) 4.
58. R. Kirchheim, Acta Materialia. 50 (2002) 413.
59. F. Liu, R. Kirchheim, Scripta Materialia. 51 (2004) 521
60. W. A. Goddard, D. W. Brenner, S. E. Lyshevski, G. J. Iafrate, Handbook of Nanoscience, Engineering, & Technology. (2003) CRC Press.
61. N. Kanani, Electroplating – Basic Principles, Processes, and Practice. (2004) Oxford, UK: Elsevier Advanced Technology.
62. R.F. Bunshah. Handbook of Deposition Technologies for Films and Coating – Science, Technology and Applications. (1994) William Andrew Publishing.
63. M. Braunovic, V. V. Konchits, N. K. Myshkin, Electrical Contacts: Fundamentals, Applications and Technology. (2007) Press Taylor & Francis.
64. Y. Lai, F. Liu, S. Kuang, J. Liu, Z. Zhang, J. Li, Y. Liu, Electrochemical and Solid-state Letters. 12 (2009) 65.
65. M. Morisue, Y. Fukunaka, E. Kusaka, R. Ishii, K. Kuribayashi, Journal of Electroanalytical Chemistry. 559 (2003) 155.

66. G. Oskam, M. Philippe, P C, Searson, Journal of Electrochemical Society. 146 (1999) 1436.
67. J. J. Kim, S. Kim, C. H. Lee, Y. S. Kim, The Journal of Vacuum Science and Technology B. 21 (2003) 1.
68. T. Hara, K. Sakata, Electrochemical and Solid-State Letters. 4 (2001)77.
69. R. Huang, W. Robl, H. Ceric, T. Detzel, G. Dehm, IEEE Transactions on Device and Materials Reliability. 10 (2010) 47.
70. A. Ibanez, E. Fatas, Surface & Coatings Technology, 191 (2005) 7.
71. X. Zhang, K. N. Tu, Chen, Zhong, Tan, Y. K, Wong, C. C., Mhaisalkar, S. G., Li, X. M, Tung, C. H, Cheng, C. K., J. NN, 5, 8 (2008).
72. B. Z. Cui, K. Han, Y. Xin, D.R. Waryoba, A.L. Mbaruku, Acta Materialia, 55 (2007) 4429.
73. S. Q. Wang, I. J. Raaijmakers, B. J. Burrow, S. Suthar, S. Redkar, K. B. Kim, Journal of Applied Physics. 68 (1990) 5176.
74. J. O. Olowolafe, J. Li, J.W. Mayer, E.G. Colgan, Applied Physics Letters. 58 (1991) 469.
75. G. F. Vander Voort, Metallography, Principles and Practice. McGraw-Hill Book Co., New York, 1984.
76. S. K. Rha, W. J. Lee, S. Y. Lee, Y. S. Hwang, Thin Solid Films. 320 (1998) 134.
77. W. Dong, J. Zhang, J. Zheng, J. Sheng, Materials Letters 62 (2008) 1589.
78. P. E. Bradley, D. Landolt, Electrochimica Acta. 45 (1999)1077.
79. T. Song, D. Li, Nanotechnology, 17 (2006) 65.
80. M.A. Meyers, A. Mishra, D.J. Benson, Progress in Materials Science. 51 (2006) 427.
81. K. M. Youssef, R. O. Scattergood, K. L. Murty, J. A. Horton, C. C..Koch, Applied Physics Letters. 87 (2005) 091904-1
82. L. Lu, Y. Shen, X. Chen, L. Qian, K. Lu, Science. 422 (2004) 304.
83. Y. Shen, L. Lu, Q. Lu, Z. Jin, K. Lu, Scripta Mater,52 (2005) 989.
84. M. Stangl, M. Liptåk, A. Fletcher, J. Acker, J. Thomas, H.Wendrock, S. Oswald, K. Wetzig, Microelectronic Engineering. 85 (2008) 534.
85. Fischer-Cripps, A. C., Nanoindentation. Mechanical Engineering Series, F. F. Ling. 2002, New York: Spinger-Verlag New York, Inc.
86. W. C. Oliver, G. M. Pharr, Journal of Materials Research. 19 (2004) 3
87. G.E.Dieter, Mechanical Metallurgy, McGraw-Hill Press Company, London, (1988) 751.
88. W.D.Callister, Jr. Materials Science and Engineering: An introduction, Seventh Edition, John Wiley & Sons, Inc. (2007), 117.
89. K. Ueno, T. Ritzdorf, S. Grace, Journal of Applied Physics. 86 (1999) 4930.
90. H. Lee, William. D. Nix, S. Simon Wong, J. Vac. Sci. Technol. B 22 (2004) 2369.
91. W. H. The, L. T. Koh, S. M. Chen, J. Xie, C. Y. Li, P. D. Foo, Microelectr. J. 31 (2001) 579.
92. S. H. Brongersma, E. Kerr, I. Vervoort, K. Maex, Proc. AIP Conf., Melville, NY 612 (2002) 229.
93. C. Lingk, M. E. Gross, Appl. Phys. Lett. 74 (1999) 682.
94. S. H. Brongersma, E. kerr, I. Vervoort, A. Saerens, K. Maex, J. Mater. Res. 17

(2002) 582.
95. S. Lagrange, S. H. Brongersma, M. Judelewicz, A. Saerens, I. Vervoort, E. Richard, R. Palmans, K. Maex, Microelectr. Eng. 50 (2000) 449.
96. R. Spolenak, L. Sauter, C. Eberl, Scripta Materialia 53 (2005) 1291.
97. M. Stangl, J. Acker, V. Dittel, W. Gruner, V. Hoffmann, K. Wetzig, Microelectronic Engineering. 82 (2005) 189.
98. J. L. Hay, and G. M. Pharr, Instrument Indentation Testing in ASM Handbook Volume 8: Mechanical Testing and Evaluation, H. Kuhn and Medlin, D., ASM International: Materials Park, OH (2000) 232.
99. W. C. Oliver, G. M. Pharr., Journal of Materials Research. 7 (1992) 1564.
100. H. Natter and R. Hempelmann, J. Phys. Chem. 100, 19525(1996).
101. L. Lu, Y. F. Shen, X. H. Chen, L. H. Qian, and K. Lu, Science 304, 422(2004).
102. X. Zhang, K. N. Tu, Z. Chen, Y. K. Tan, C. C. Wong, S. G. Mhaisalkar, X. M. Li, C. H. Tung, and C. K. Cheng, J. Nanosci. Nanotechnol. 2008. Vol8, No5, 2568.
103. A. Balasubramanian, D. S. Srikumar, G. Raja, G. Saravanan and S. Mohan. Surface Engineering. Vol 25, No 5, (2009) 389.

Chapter 3 Experimental Procedure

3.1 Substrate Preparation

Ferritic steel (type 945) with dimensions of 8 mm × 5 mm × 1 mm were used as substrate for copper electrodeposition. The substrate was ground using a series of waterproof silicon carbide papers (#120 - #2400), followed by diamond paste polishing down to 1 μm and final polishing (OPS). A mirror-like surface finishing was obtained. The substrate was then cleaned ultrasonically in ethanol for 3 minutes and dried. Prior to electrodeposition, the ferritic steel sheet was immersed into a copper sulfate solution for less than 5 seconds to obtain a copper buffer layer of about a few nanometers for activation purpose. Finally the pre-treated substrate was rinsed in distilled water.

3.2 Direct Current and Pulsed Current Electrodeposition

Electrodeposition of copper has been carried out using direct current (DC) and pulsed current (PC). The anode was a high purity copper sheet (99.99% purity) with dimensions of 35 mm × 55 mm × 7 mm. The prepared ferritic steel substrate (described in section 3.1) was used as substrate. The composition of the electrolyte is shown in Table 3.1. The pH value of the electrolyte is around 1.1.

Table 3.1 Electrolyte compositions for copper thin film electro-deposition

$CuSO_4.5H_2O$	185g
H_2SO_4	32ml (1.89g/ml)
$CuCl_2$	0.05g
Distilled Water	755g

3.2.1 Direct current (DC) deposition

A constant potential of 0.15 V was applied in the DC deposition process. A HQ PS1503SB DC power supply with the voltage range of 0-15 V and current range of 0-3 A was used. A current of about 23 mA was measured in the circuit for the DC deposition of sample FS1. Samples were electrodeposited 40 minutes for the purpose of microstructure observations, one hour for the purpose of growth rate measurement at room temperature.

3.2.2 Pulsed current (PC) deposition

In PC deposition, square wave potentials with unequal on-time and off-time were applied. The pulsed constant current modes used are illustrated in Figure 3.1. During the on-time a constant potential with peak current of 500 mA was applied to electrodes and during the off time no potential was applied. The sum of the on-time and off-time was referred to as the time period. The on-time was maintained at 0.02 s for pulsed samples. Off-time of 1s, 2s and 3s was used for the deposition of samples

FS2, FS3 and FS4, respectively.

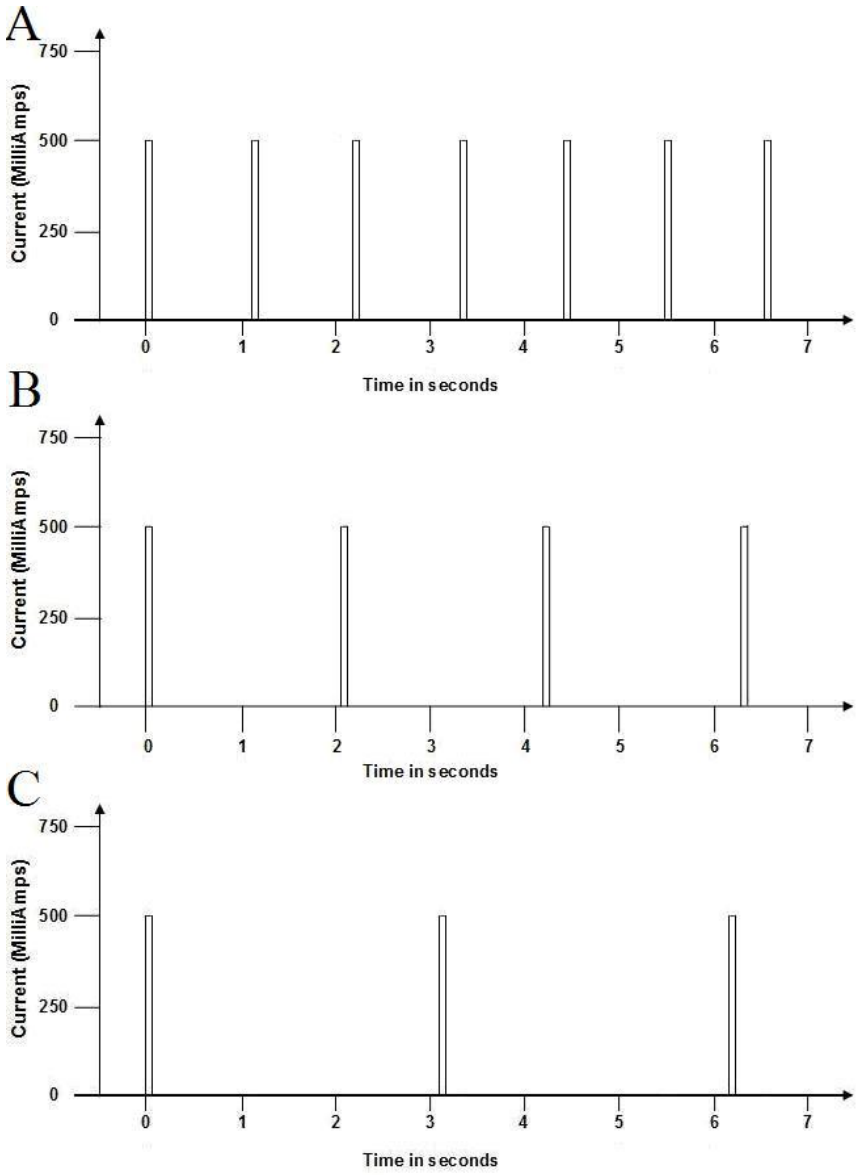

Figure 3.1 Schematic drawings showing different PC depositions with unequal on-times and off-times. A) on-time 0.02 s and off-time 1 s, peak current 500 mA. B) on-time 0.02 s and off-time 2 s, peak current 500 mA. C) on-time 0.02 s and off-time 3 s, peak current 500 mA.

The on-time and off-time was controlled using a Hengstler 741 0-R41-011 multifunction time-delay relay connected to a DC power supply. A program written in qbasic language was used to control the relay via a computer. The set up is shown in

figure 3.2.

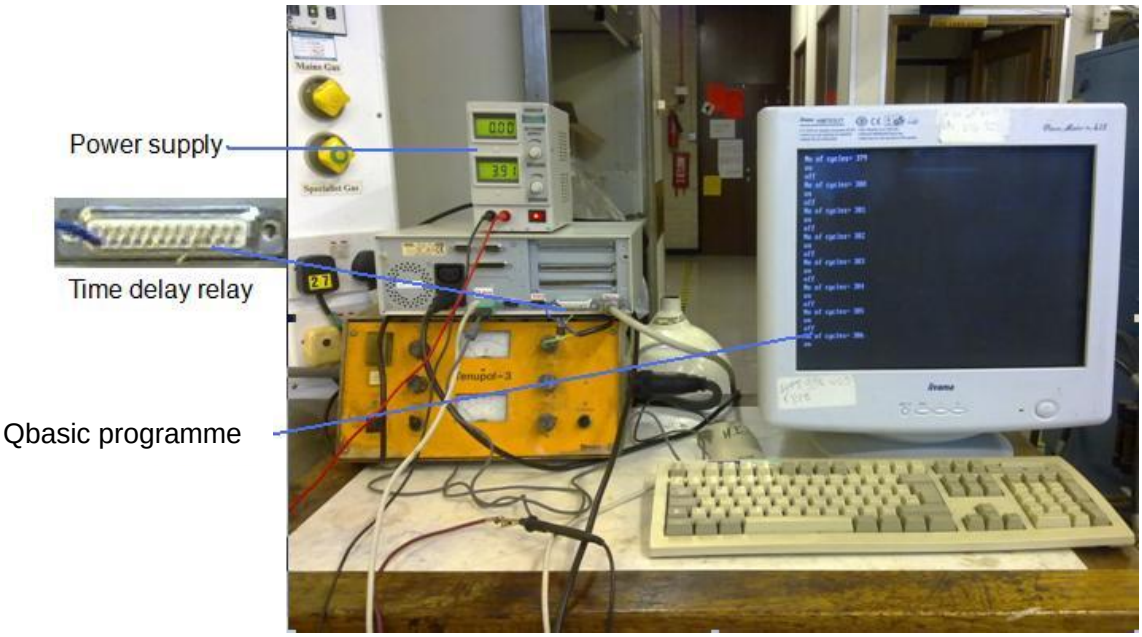

Figure 3.2 Photograph showing the setup for the PC deposition

The deposition parameters are summarized in Table 3.2. Sample FS1 was prepared by DC deposition and samples FS2, FS3 and FS4 were prepared by PC deposition. In all depositions, the electrolyte, temperature, stirring magnitude and substrate size were kept the same.

Table 3.2 Sample designation and the deposition parameters used

Sample Reference	On-time	Off-time	Voltage (V)	Current Density (mA/cm^2)
FS1	0.02 s	0 s	0.15	23
FS2	0.02 s	1 s	3.37	500
FS3	0.02 s	2 s	3.37	500
FS4	0.02 s	3 s	3.37	500

3.3 Microstructural Characterisation

3.3.1 X-Ray diffraction

The phase identification and 2θ diffraction pattern scan were carried out on a Philips diffractometer at a scanning rate of 2 degree per minute, a step size of 0.02 degree. X-ray diffraction experiments were performed on a Philips diffractometer using copper Ka radiation with wavelength of 1.5406 angstrom.

3.3.2 Optical microscopy

Ferritic steel was metallographically prepared and etched in 2% Nital for about 10 seconds. Optical observations were conducted on a Leica DMRX microscope using a KS300 image capture and analysis software. The mean grain size (equivalent diameter) was worked out from an average of over 500 grain measurements.

3.3.3 Scanning electron microscopy (SEM)

For SEM observation, the substrate was prepared following the standard metallographic procedure. Copper films used for surface morphology observation were rinsed in ethanol and dried after deposition without grinding and polishing. Copper films used for back-scattered electron imaging were cleaned in ethanol and distilled water after the deposition and then ground on SiC paper of 4000 grade and mechanically polished on a Struers polishing machine using Largo and Chem cloths with abrasive suspension of diamond and OPS respectively. Finally electropolishing

was performed at a voltage of 3.2 V at room temperature. The electropolishing solution contained 500 ml distilled water, 200ml ethanol, 250ml H_3PO_4, 50 ml propanol and 5g carbamide. Finally electropolishing was performed at a voltage of 3.2 V. Microstructure characterisation and composition analysis were carried out on a JEOL 7000 SEM with a field emission gun and equipped with an Oxford INCA Energy Dispersive X-ray (EDX) and Oxford INCA Crystal Electron Back-scatter Diffraction (EBSD) analysis system. For EBSD analysis, the Kikuchi lines produced by the back-scattered electrons were recorded by a Peltier cooled CCD camera and automatically analysed by a computer programme to obtain the crystal orientation.

The particle size and grain size of analyses were performed using a KD-400 image analyser and ImageJ, assuming a circular particle/grain shape. Approximately 1500 particles were counted for copper films and 700 grains of the ferritic steel were measured.

3.3.4 Transmission electron microscopy (TEM)

Electrodeposited films of about 100 μm thick were manually detached from the substrates and ground down to about 80 μm thickness which was measured by high vernier caliper. Discs of 3 mm diameter were then punched from these films and glued onto a copper grid for twin-jet electropolishing (Struers Tenupol-5). Polishing solution consisting of 500 ml distilled water, 200ml ethanol, 250ml H_3PO_4, 50 ml propanol and 5g carbamide was used, at -15 ^oC with an applied voltage of 7.5 V. An FEI Tecnai F20 FEG TEM and a Philips CM20 TEM were used for microstructure observations.

3.3.5 Focused ion beam microscopy (FIB)

As-deposited copper films of about 80 μm thickness were cleaned in ethanol and distilled water, and then performed with electropolishing at a voltage of 3.2 V in order to carry out the self-annealing study. The electropolishing solution contained 500 ml distilled water, 200ml ethanol, 250ml H_3PO4, 50 ml propanol and 5g carbamide. A range of different beam currents (typically between 0.5 nA and 65 nA) were used for the milling process and the ion beam imaging was carried out with ion beam current at 10 pA. A dual-beam (FIB/SEM) microscope (FEI Quanta 3D Focused Ion Beam system) was used to study the self-annealing and to obtain the cross-sectional observations of the electrodeposited copper film.

3.4 Mechanical Property Assessment

A Nanoindentation Test 600 machine (Micro Materials, UK) was used to evaluate the hardness and elastic modulus of the electrodeposited copper films. A load-control mode was used in all the indentation tests, with the pre-set peak load of 50 mN and a dwell time of 10 seconds at the peak load. 10 measurements were made under each condition.

Chapter 4 Results and Discussion

4.1 Substrate Investigation

A commercial ferritic steel sheet from Tata Steel Ltd was used as a substrate for both DC and PC deposition. The chemical composition of the ferritic steel is given in Table 4.1. It was hot rolled at 750 ℃ and then air-cooled to room temperature.

Table 4.1 Chemical composition of the as-received ferritic steel (wt %).

C	Si	Mn	P	S	Cr	Al	Fe
0.041	0.010	0.140	0.011	0.007	0.020	0.027	Balance

4.1.1 Morphology and grain size measurement

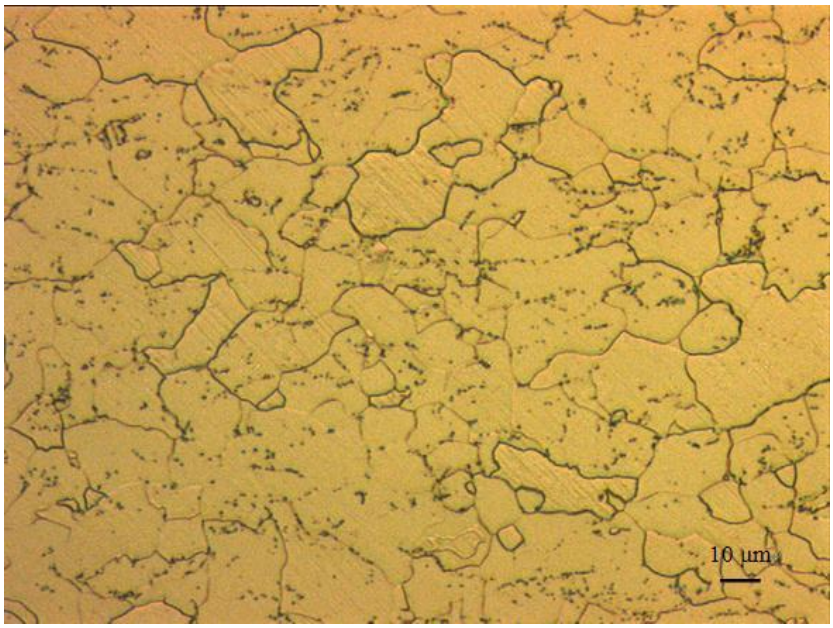

Figure 4.1 Optical micrograph showing the microstructure of the as-received ferritic steel.

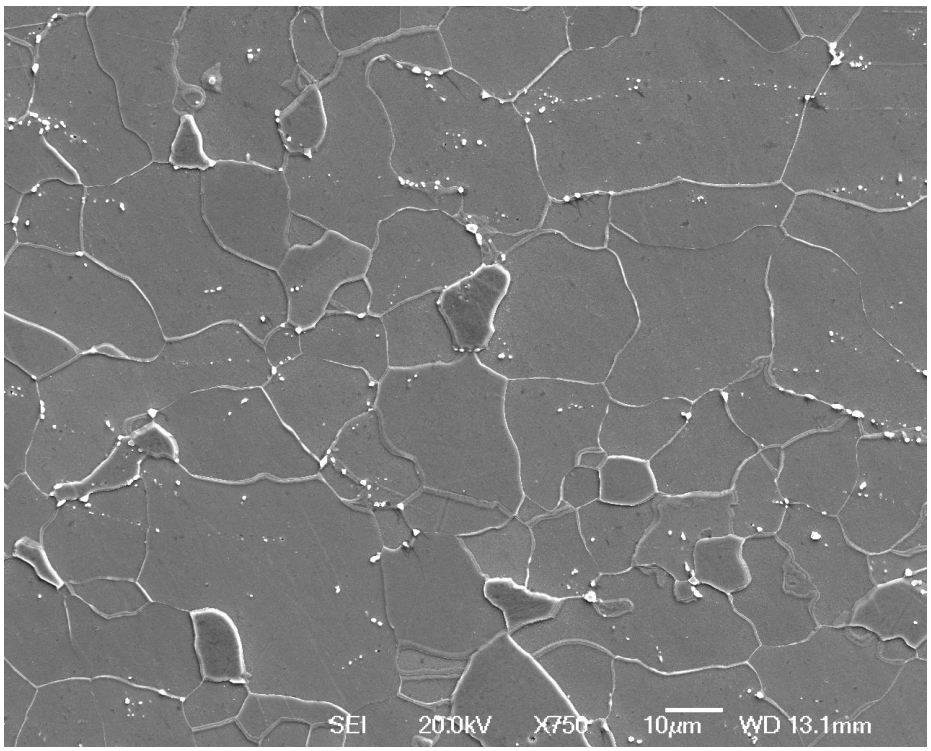

Figure 4.2 Secondary electron micrograph of the as-received single phase ferritic steel.

Figure 4.1 illustrates a typical optical micrograph obtained from the ferritic steel after 2% nital etching. Figure 4.2 shows a secondary electron micrograph obtained from the same sample. According to the EDX measurement results, the black dots and curves in figure 4.1 and the white marks in figure 4.2 are preferably carbides by EDS (EDS comparisons not shown here) as dispersed phases in the matrix of ferrite along with the inclusions such as MnS or Al_2O_3. The grain size was measured and calculated from 18 images of the total area of 0.03 mm^2. The average grain size measured from the ferritic steel is 21.3 $\pm$0.6 μm and the grain size varies from less than 5 μm to more than 60 μm. Figure 4.3 shows the results of the grain size distribution of the ferritic steel. The result indicates a wide grain size distribution of the ferritic steel. The optical grain size difference between Figure 4.1 and 4.2 are due to the difference of their scale bars.

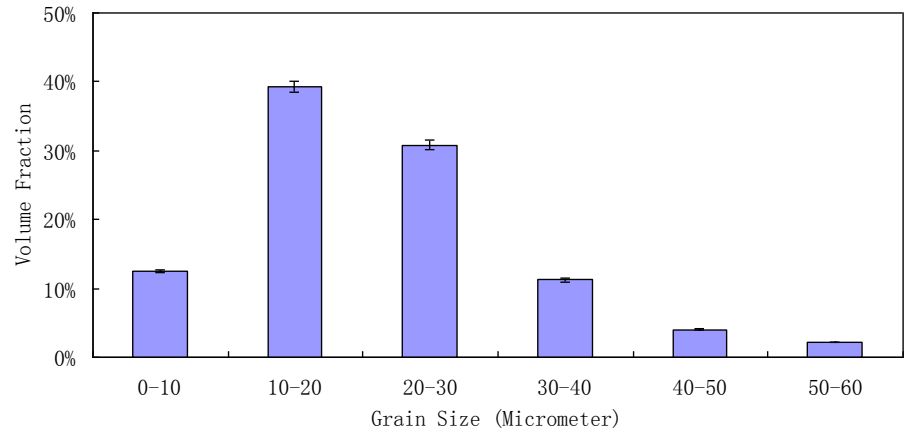

Figure 4.3 Grain size distribution showing a wide grain size range of the ferritic steel.

4.1.2 Texture analysis

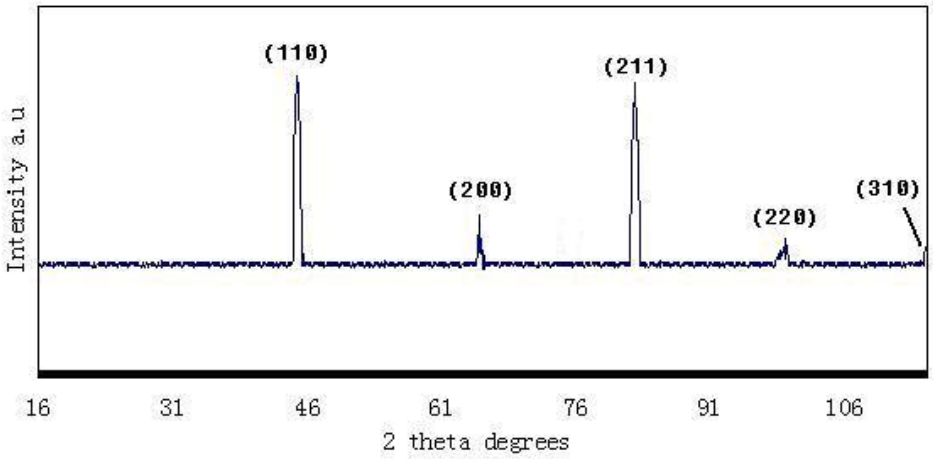

Figure 4.4 XRD pattern showing typical peaks from the ferritic steel

Figure 4.4 shows an XRD pattern obtained from the ferritic steel. The XRD pattern displays (110), (200), (211), (220) and (310) reflections of the bcc phase at 44.8 ^{o}, 65.2 ^{o}, 82.5 ^{o}, 99.1^{o} and 115.8^{o}, corresponding to d-spacings of 2.027, 1.433, 1.169, 1.013 and 0.906 Å. The (110) and (211) reflections have obviously high intensity than the other reflections. Further texture analysis was studied using EBSD.

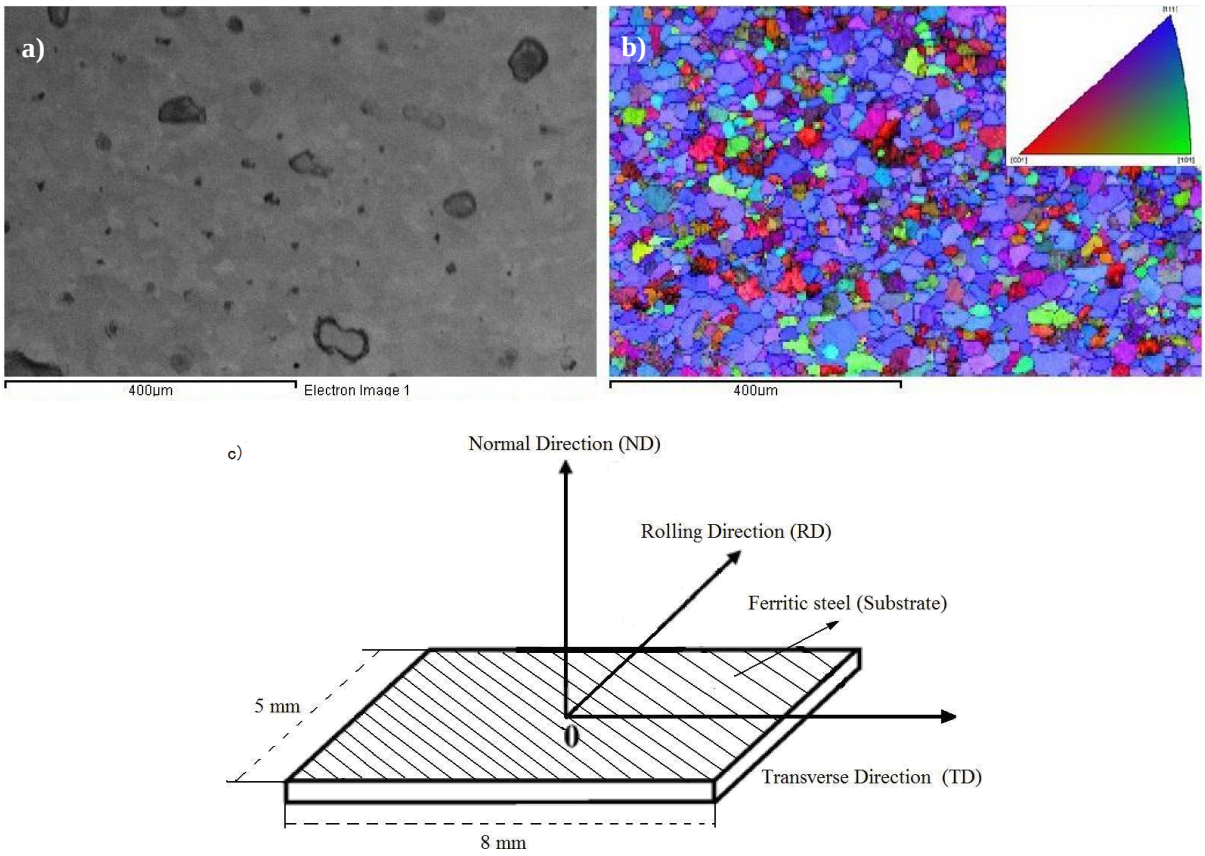

Figure 4.5 SEM image and EBSD map obtained from the same region on a ferritic steel. a) Secondary electron micrograph of an electropolished ferritic steel sample. b) EBSD orientation image map with orientation colour key obtained from the rolling plane of the ferritic steel sample. c) Schematic drawing showing the geometry of the ferritic steel sample.

Figure 4.5 shows a secondary electron image of the ferritic steel sheet together with the EBSD map of the same region. The SEM image does not clearly reveal the grain structure, but from the EBSD orientation image map clear grain structure can be observed. The structure looks banded which may be due to the experimental operations. The results suggest that the ferritic steel substrate has a strong <222>//ND texture.

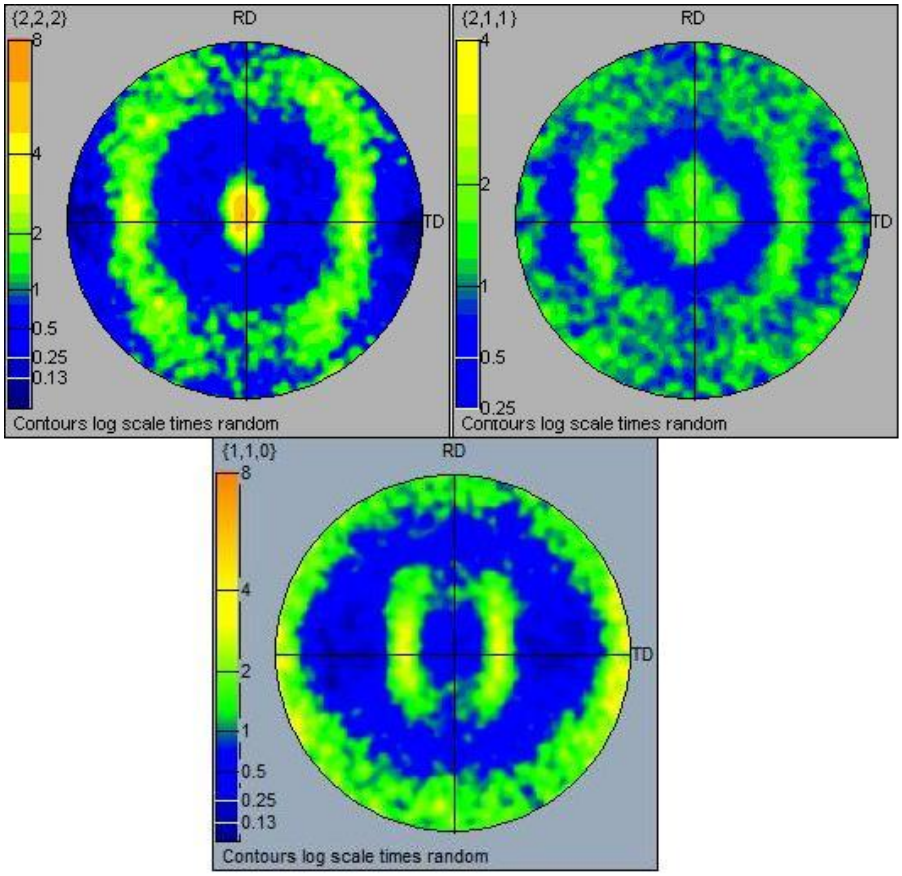

Figure 4.6 (222), (211) and (110) pole figures obtained from the ferritic steel substrate.

Figure 4.6 shows the (110), (222) and (211) pole figures obtained from EBSD mapping of the ferritic steel. (222) and (211) planes are observed approximately parallel to the steel sheet surface. The maximum intensities at the centre of the (222) and (211) pole figures, are about 5.5 and 1.5 time of the random, respectively. These results confirm that the ferritic steel substrate has a strong [222]//ND texture.

4.2 Surface Morphology Observations of Copper Film

The surface morphology of the four electrodeposited films is shown in Figure 4.7. Sample FS1 was DC deposited and FS2, FS3 and FS4 were all obtained using the PC deposition. The surface morphology varies with the deposition parameters.

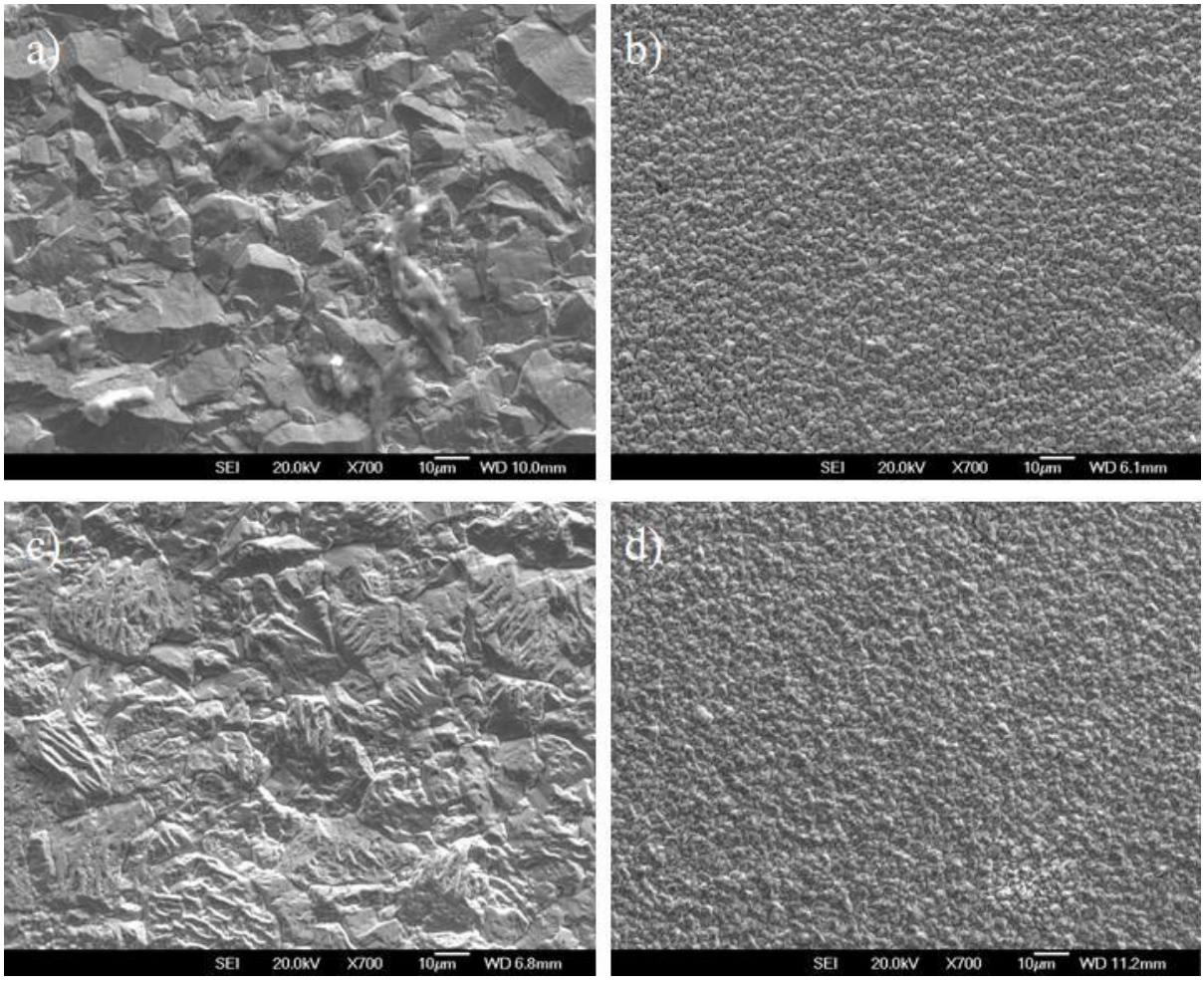

Figure 4.7 Secondary electron images obtained from copper films electrodeposited for 40 minutes with varying deposition parameters. a) DC deposition at 0.15 V, sample FS1. b) PC deposition with on-time of 0.02 s, off-time of 1 s and peak current density of 0.5 A/cm^2, sample FS2. c) PC deposition with on-time of 0.02 s, off-time of 2 s and peak current density of 0.5 A/cm^2, sample FS3. d) PC deposition with on-time of 0.02 s, off-time of 3 s and peak current density of 0.5 A/cm^2, sample FS4.

The overall surface morphology of the electrodeposited copper films with different deposition parameters is shown in figure 4.7. The films are dense and there is no observable porosity or crack on the surface. It can be observed that the surface morphology varies with deposition parameters. The surface primarily consists of particles which are much bigger than the grains which are investigated in section 4.4. Sample FS1 obtained from DC deposition consists of facetted particles. Figures 4.7 b), 4.7 c) and 4.7 d) compare the surface morphology of electrodeposited copper using PC deposition with the same on-time but different off-time. It can be observed that the on/off time has a significant effect on the film morphology. The thickness of all films was kept around 80 μm in order to eliminate the influence of the layer thickness on morphology. A relatively smooth surface morphology is evident in figures 4.7 b) and 4.7 d. Both samples FS2 and FS4 have a similar topography consisting of small and granular particles. The difference of particle size and size distribution between FS2 and FS4 is not obviously observed at this magnification. The surface morphology of sample FS3 is different from figures 4.7 b) and d. Although obvious voids or pinholes have not been observed in sample FS3 at this magnification, its surface is rougher than samples FS2 and FS4. The particles in sample FS3 are less clearly facetted than in samples FS2 and FS4. The large differences of surface morphology between FS2, FS3 and FS4 primarily come from the different cycles, i.e. off-time. The unique topography of FS3 may derive from the defects coming from the processing. Further work needs to be carried on to explain the phenomenon differences.

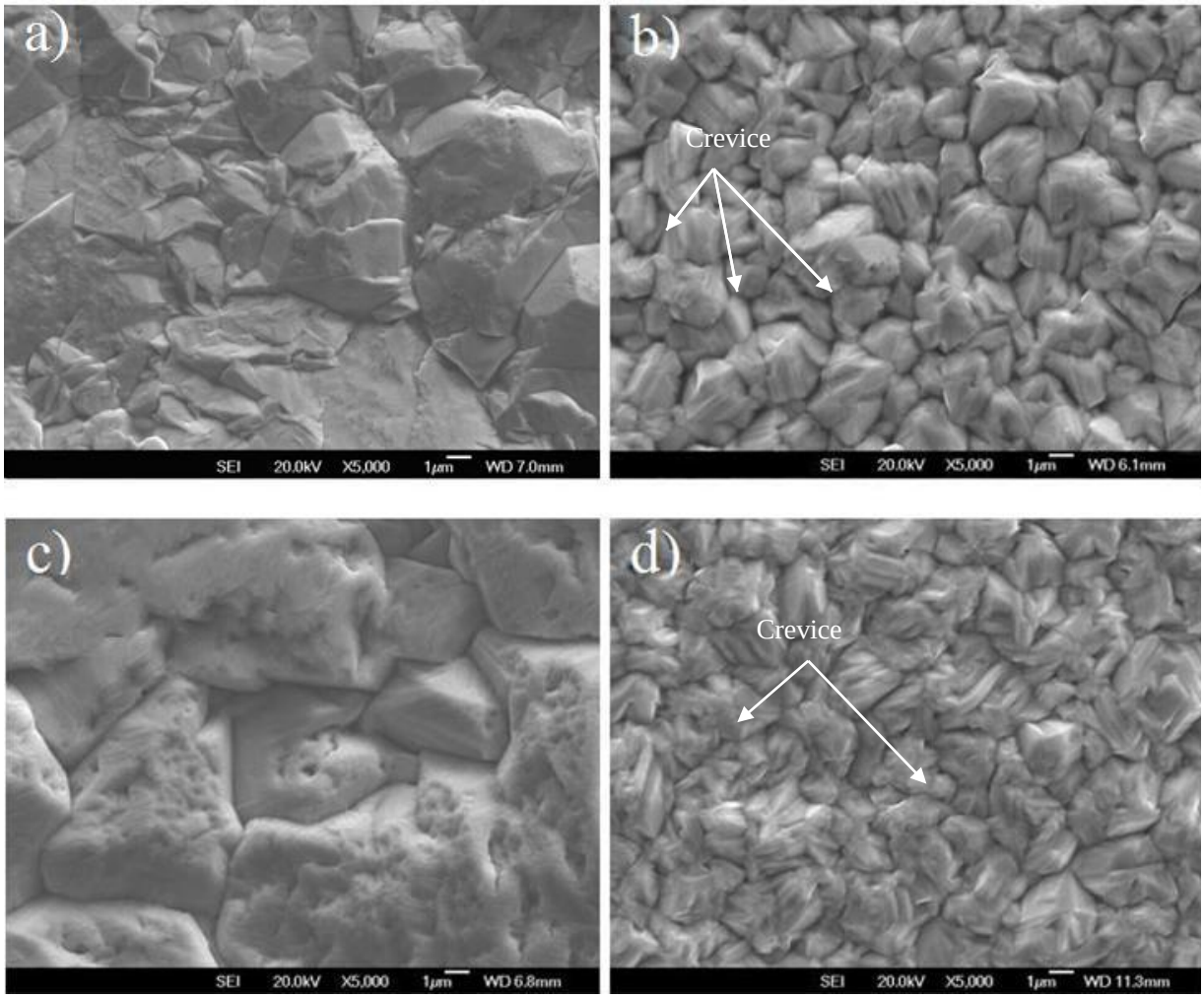

Figure 4.8 Higher magnification secondary electron images showing the microstructure of copper films electrodeposited for 40 minutes with different deposition parameters. a) DC deposition at current density of 23 mA/cm^2, sample FS1. b) PC deposition with on-time of 0.02 s, off-time of 1 s and peak current density of 0.5 A/cm^2, sample FS2. c) PC deposition with on-time of 0.02 s, off-time of 2 s and peak current density of 0.5 A/cm^2, sample FS3. d) PC deposition with on-time of 0.02 s, off-time of 3 s and peak current density of 0.5 A/cm^2, sample FS4.

The surface morphology of the films is shown at higher magnification in figure 4.8. The much smaller in size of the individual grain (nano-grained size) can be determined and evidenced in section 4.4. The average particle size of sample FS1 cannot be determined in figure 4.8 a) as the smaller crystallites tend to form clusters with non-uniform shapes, but the particle size of the dome-like particles in figure 4.8 b) and d) is about 2.12 ± 0.56 μm and 1.98 ± 0.62 μm, respectively, and the average

size of sample FS3 measured from the lower magnification images is about 10.6 ± 1.08 μm The different deposition parameters thus have produced different particle morphologies. For sample FS1, some of the particles are larger than 10 μm, but most of them cannot be easily distinguished. The crevices between the particles for FS1 are fewer than for samples FS2, FS3 and FS4. The individual particles of samples FS2 and FS4 can be clearly discerned compared to samples FS1 and FS3. At this higher magnification, it can be observed that the overall shapes of primary particles within aggregates/grain clusters of samples FS2 and FS4 are the same. The particles are much bigger in figure 4.8 c) and some quite obvious pinholes and porosities as defects are observed on the surface.

Overall, more crevices among the particles are observable on the PC deposited samples than the DC deposited sample, which may be due to the desorption of hydrogen during the off-time [1]. During the electrodeposition, small crystallites (nano range in size) are likely to form clusters (micro range in size). The observed morphology reflects the clusters (i.e. particles) rather than individual grains. It has been reported that materials synthesised by deposition are often plagued by high levels of residual stress, the actual grain clustering and coalescence are favoured in the nanocrystalline film in order to reduce the intrinsic stress/strain [2, 3]. It also has been reported that neighbouring grains of a growing film spontaneously join together by grain coalescence under the action of interatomic forces, eliminating two free surfaces in favour of an elastically strained grain boundary [3]. Individual grains have to overcome certain energy barrier to coalesce and try to reach an equilibrium state. Higher magnification SEM images obtained from samples FS2 and FS4 are shown in figures 4.9 and 4.10, respectively. The particles/aggregates developed a multi-faceted

morphology contains defects (pore/band) on the crystal platelets, suggesting the merging of grains as building blocks of the particle aggregation. Although it does not show if there are clear grain boundaries between the clusters and layers, it is logical to reason that there are indeed boundaries between the layers because the size of crystallites measured. In section 4.4, by TEM is much smaller than that it would be if all these particles were individual grains. The atom distribution in grain boundary is less ordered than at grain interior. When the grains grows, they gradually merge and form grain boundaries. If the final stage is not complete, defects such as pores may be formed at the triple junctions. Figure 4.9 b) indicates that the relatively larger particles appear to be the result of the merging of several neighbouring smaller grains. The pores within the particle may indicate that the merging was incomplete, still in process [3]. Figure 4.10 indicates that the "big island-shape" particles consist of smaller grains in the particular "transition" area obtained from the "fresh" sample FS3. The pores are formed after the merging of the neighbouring grains. The schematic drawing shows the transitional area where individual grains are yet to form particle aggregations. This may explain the scenario in figure 4.10 a).

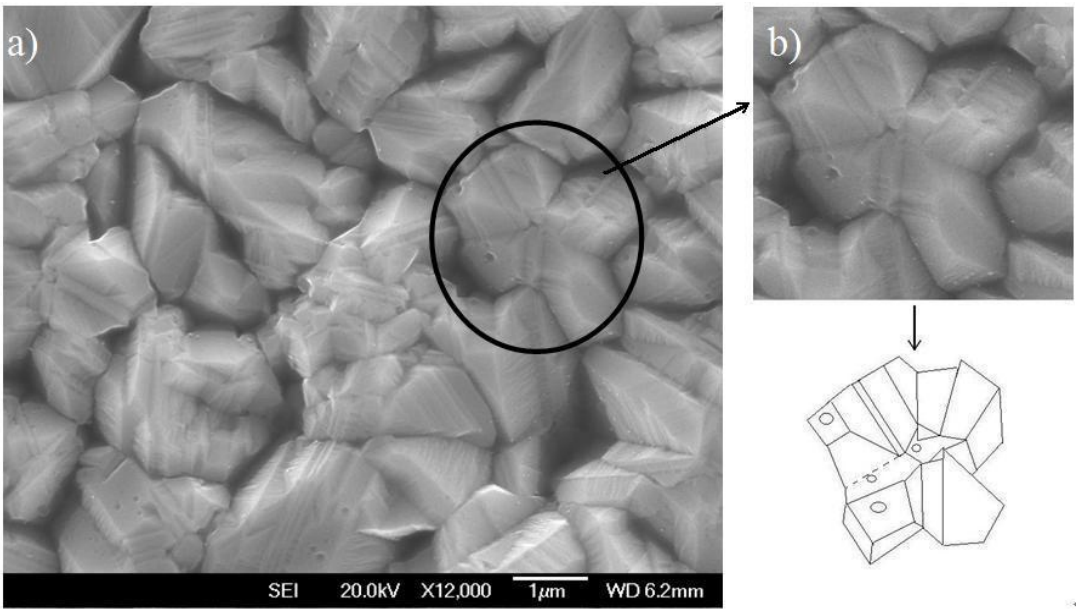

Figure 4.9 a) Secondary electron micrograph showing the particle morphologies of sample

FS2. b) A cluster of grains revealing the process of coalescence of neighbouring grains. The dashed lines indicate the location of eliminated boundaries.

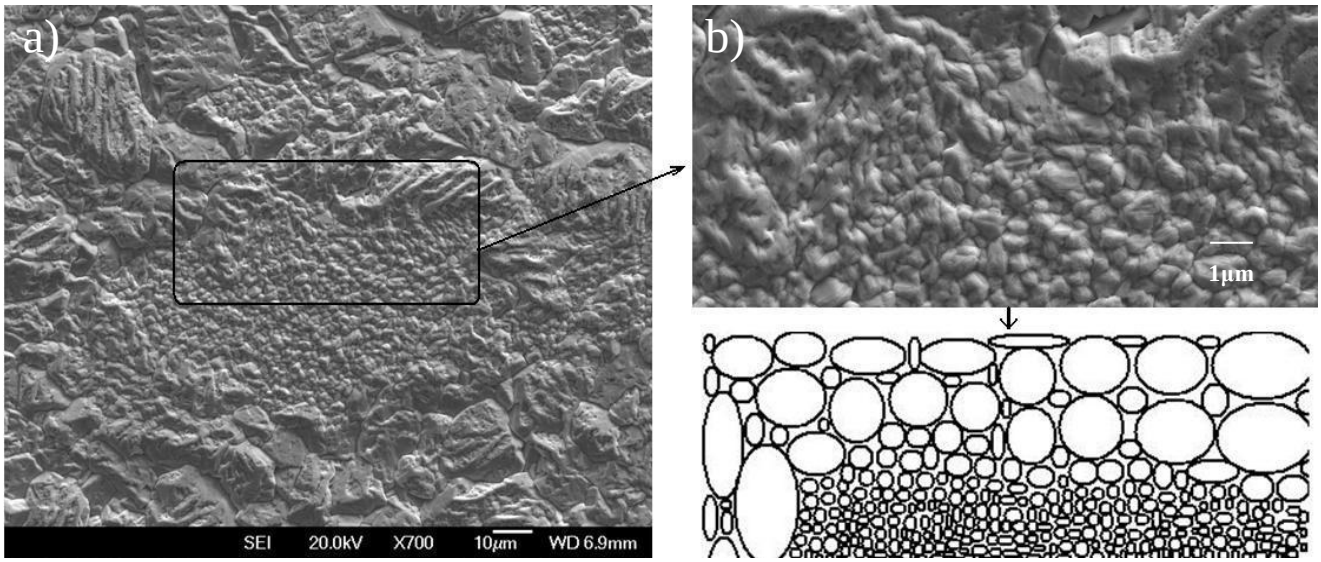

Figure 4.10 a) Secondary electron micrograph showing the surface morphologies (FS3). b) A high magnification SEM image revealing the process of coalescence of neighbouring grains.

The results in the current study indicate that the small grains tend to form clusters or particles. The coalescence can be accomplished by either conventional boundary migration or direct elimination of common boundaries [3]. In nanocrystalline films, the driving force for grain coalescence is the high internal strain of the grains coming from the processing [4]. Overall, the present results are in agreement with the relevant literature, but it has been rarely reported about the same clarification in electrodeposited copper films.

4.3 Film Growth Rate Measurements

SEM was used to measure the thickness of the deposited films. After one hour electro-deposition the thickness of FS1, FS2, FS3 and FS4 is about 84 μm, 75 μm, 57 μm and 46 μm. Figure 4.11 shows the thickness of the as-deposited samples FS1, FS2, FS3 and FS4 on the ferritic steel substrate after one hour electrodeposition.

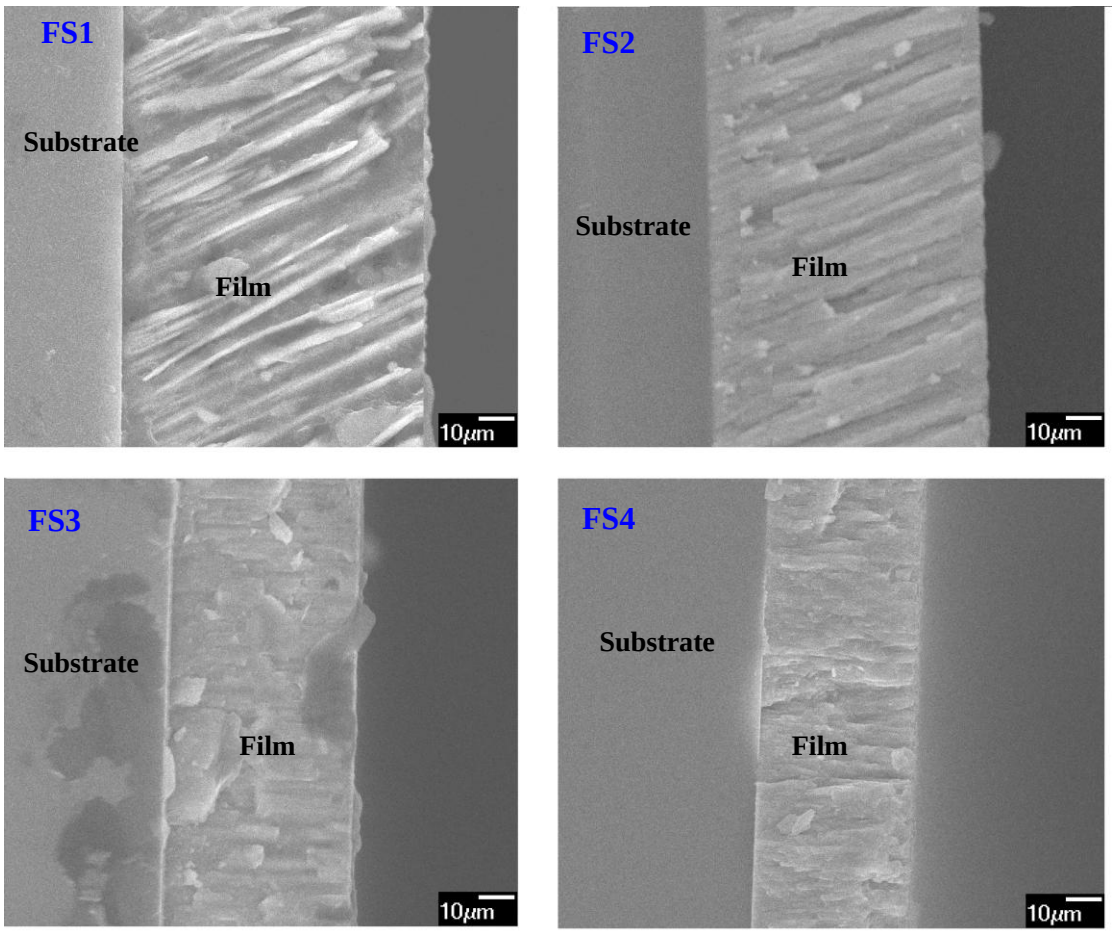

Figure 4.11 Secondary electron micrograph showing the thickness of the samples FS1, FS2, FS3 and FS4 on the steel substrate for one hour's electrodeposition.

Figure 4.12 shows the thickness of the films as a function of the deposition time obtained from samples FS1, FS2, FS3 and FS4. The overall trend for the film growth

is linear. The thickness increases linearly at a rate of 1.4 ± 0.01 μm/min, 1.26 ± 0.01 μm/min, 0.94 ± 0.02 μm/min and 0.76 ± 0.02 μm/min of samples FS1, FS2, FS3 and FS4, respectively. Table 4.2 illustrates the growth rates of the copper films under different deposition conditions. The nominal average growth rate is calculated considering both the on-and off-time of electrodepostion. If only the on-time is taken into consideration for film nucleation and growth, then the net growth rate of relatively higher value can be derived. However, this is not realistic. Indeed during the off-time in a PC deposition, the deposition of copper still occurs. The nominal average growth rate and average net growth rate for the copper deposits are listed in table 4.2.

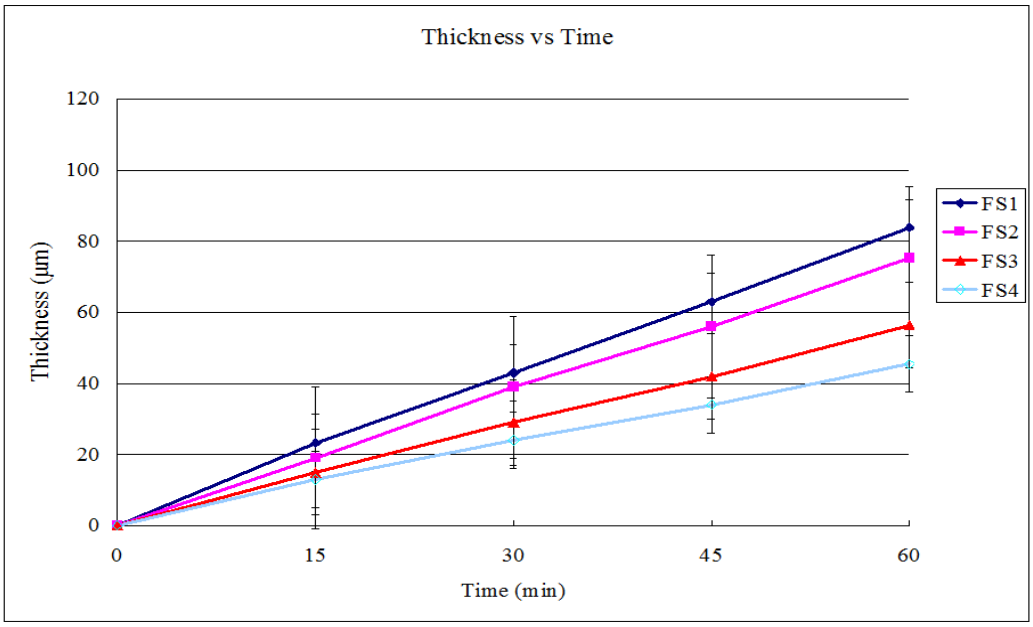

Figure 4.12 Graph of thickness of FS1, FS2, FS3 and FS4 as a function of time.

Table 4.2 Summary of nominal average growth rate and average net growth rate of Cu with different pulsed cycles.

Sample Reference	Off time	Peak Current Density (mA/cm^2)	Average nominal growth rate ($nm\ s^{-1}$)	Average net growth rate ($nm\ s^{-1}$)
FS1	0 s	23	23.3	23.3
FS2	1 s	500	20.9	1066.8
FS3	2 s	500	15.7	1582.3
FS4	3 s	500	12.7	1908.5

It can be noted from Table 4.2 that the DC deposition provides a higher nominal deposition rate than the PC deposition. The PC deposition reflects the lower nominal deposition rate as a function of pulsed cycles.

4.4 TEM Microstructure Observations

The grain size, grain boundaries, twin and twin fraction of the electrodeposited copper films were studied using TEM.

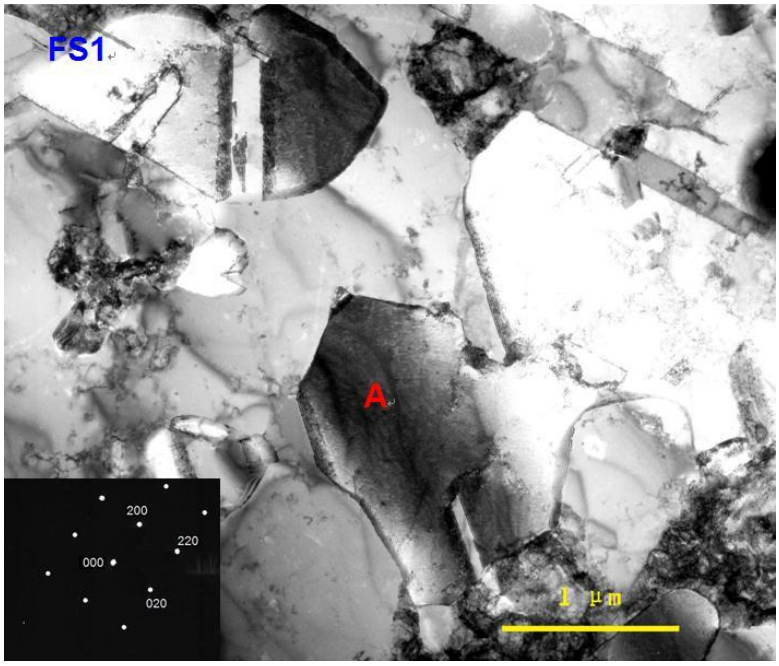

Figure 4.13 BF image showing the microstructure of sample FS1. The corresponding SAD pattern was taken from region A.

Figure 4.13 shows a bright field micrograph taken from sample FS1. The as-deposited copper consists the grain size rangeing from 0.9 μm to 1.8 μm with an average of 1.2 μm. Some of the grains include twins. The twins separate some of the original grains into submicron-thick twin/matrix lamellar structure. The average twin thickness is about 135 nm. The length of the twins is from 300 nm to 800 nm. The twin area fraction in FS1 is 4.5%. The insert in figure 4.13 is a selected area diffraction (SAD) pattern along the [001] zone axis taken from region "A".

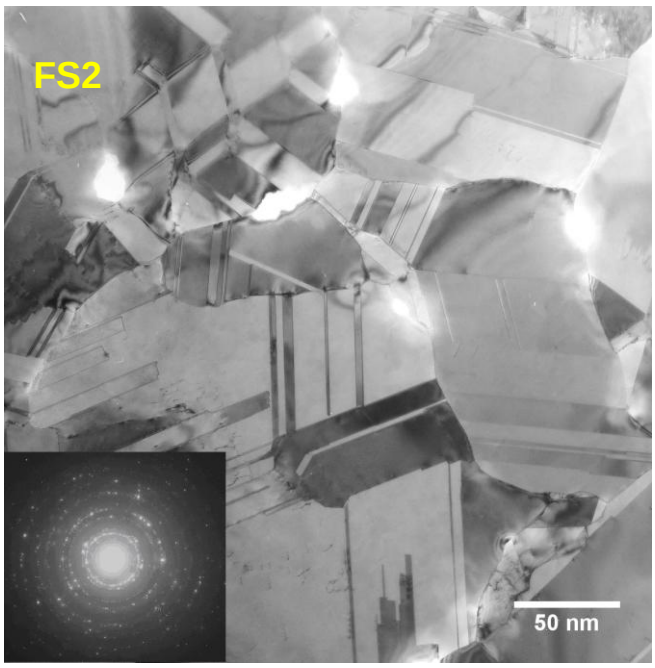

Figure 4.14 BF image showing the typical microstructure of sample FS2 and the electron diffraction ring pattern (inset).

Figure 4.14 shows a bright field micrograph taken from sample FS2. The irregular grain structure is observed. The grain size of FS2 ranges from 20 nm to 150 nm with an average of 70 nm. Most grains contain nano-scaled twins. Thickness of the twin lamellae ranges from several nanometres to about 20 nm. The length of the twins is from 30 to 60 nm. The twin area fraction for FS2 is about 14.5%. The inset electron diffraction ring pattern corresponds to its nanocrystalline structure.

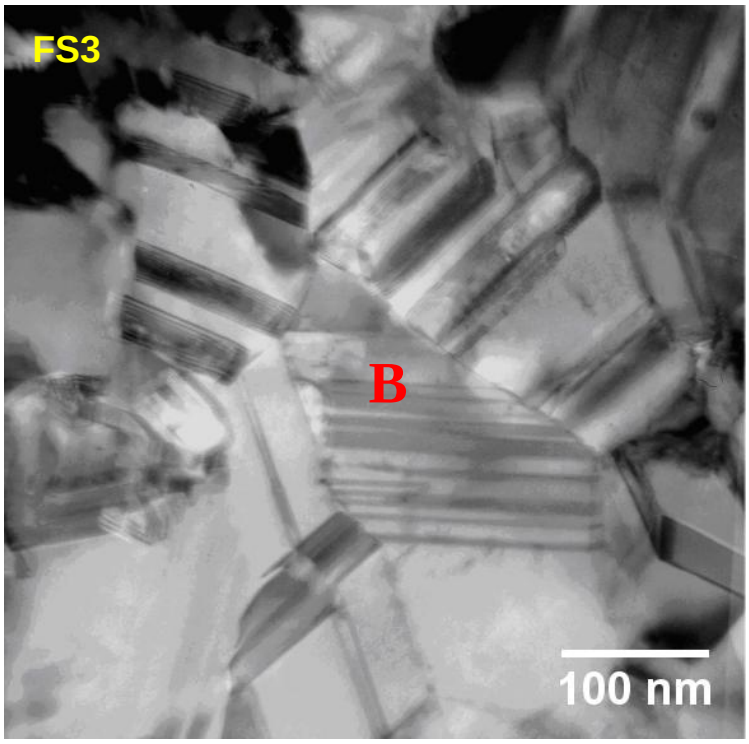

Figure 4.15 BF image showing the microstructure of sample FS3.

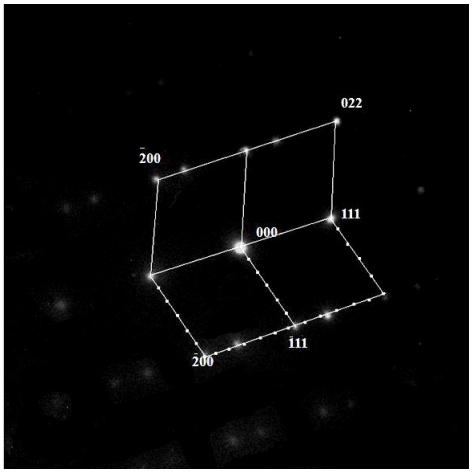

Figure 4.16 Selected area electron diffraction pattern along $[0\bar{1}1]$ zone axis taken from region "B" in figure 4.15.

Figure 4.15 shows a bright field micrograph taken from sample FS3. The sample consists of irregularly shaped grains. The grain size ranges from 100 nm to 460 nm, with an average of 250 nm. Twins are visible in most of the grains with straight and coherent twin boundaries. The length of the twins is from 100 nm to 300nm. FS3 has

higher twin density than FS1 and FS2. The dense twins separate the original grains into smaller nanometer-thick twin/matrix lamellar structure. Thickness of the twin lamellae ranges from several nanometres to about 45 nm. The twin area fraction is about 35.6 % in FS3. Figure 4.16 shows an SAD pattern taken from the region "B" in figure 4.15 along the $\left[0\bar{1}1\right]$ zone axis, characteristic of a twin in FCC crystal. The full line and dashed line represent the matrix and twin diffraction, respectively. The twinning plane is {111}.

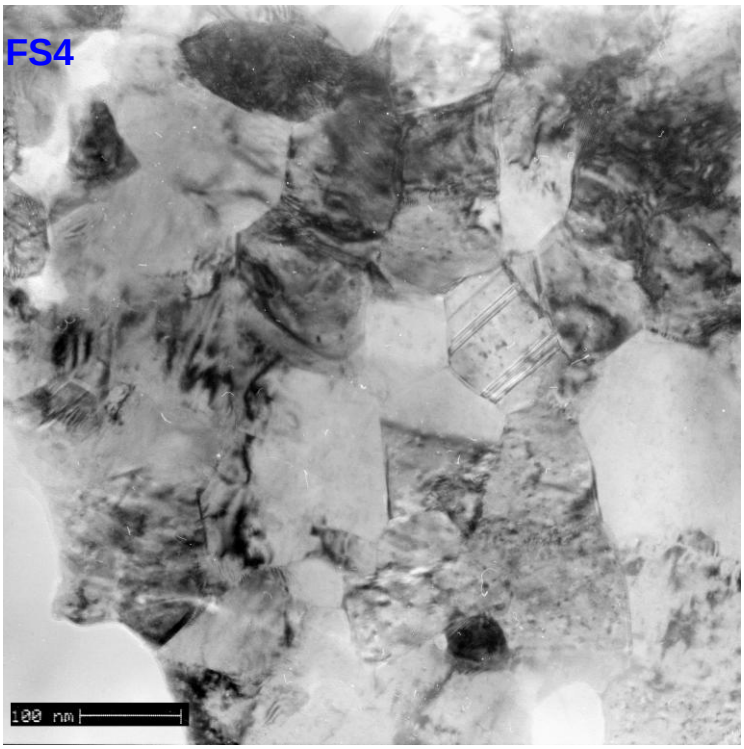

Figure 4.17 BF image showing the microstructure of sample FS4

Figure 4.17 shows a bright field micrograph taken from sample FS4, consisting of irregularly shaped grains (most of them are roughly equiaxed). The grain size of FS4 ranges from 60 nm to 150 nm with an average of 100 nm. Some of the grains have

twins of 40 to 80 nm long. The thickness of the twin lamellae is about 10 nanometres. The twin area fraction in FS4 is about 10%.

For comparison purpose, TEM micrographs at the same magnification obtained from samples FS2, FS3, FS4 are shown in figure 4.18. Measurements of the grain size are shown in figure 4.18 (d), (e) and (f). FS4 has a narrow distribution indicating its more homogeneous microstructure than samples FS2 and FS3. The deposition parameters, grain size and twin fraction are summarized in table 4.3.

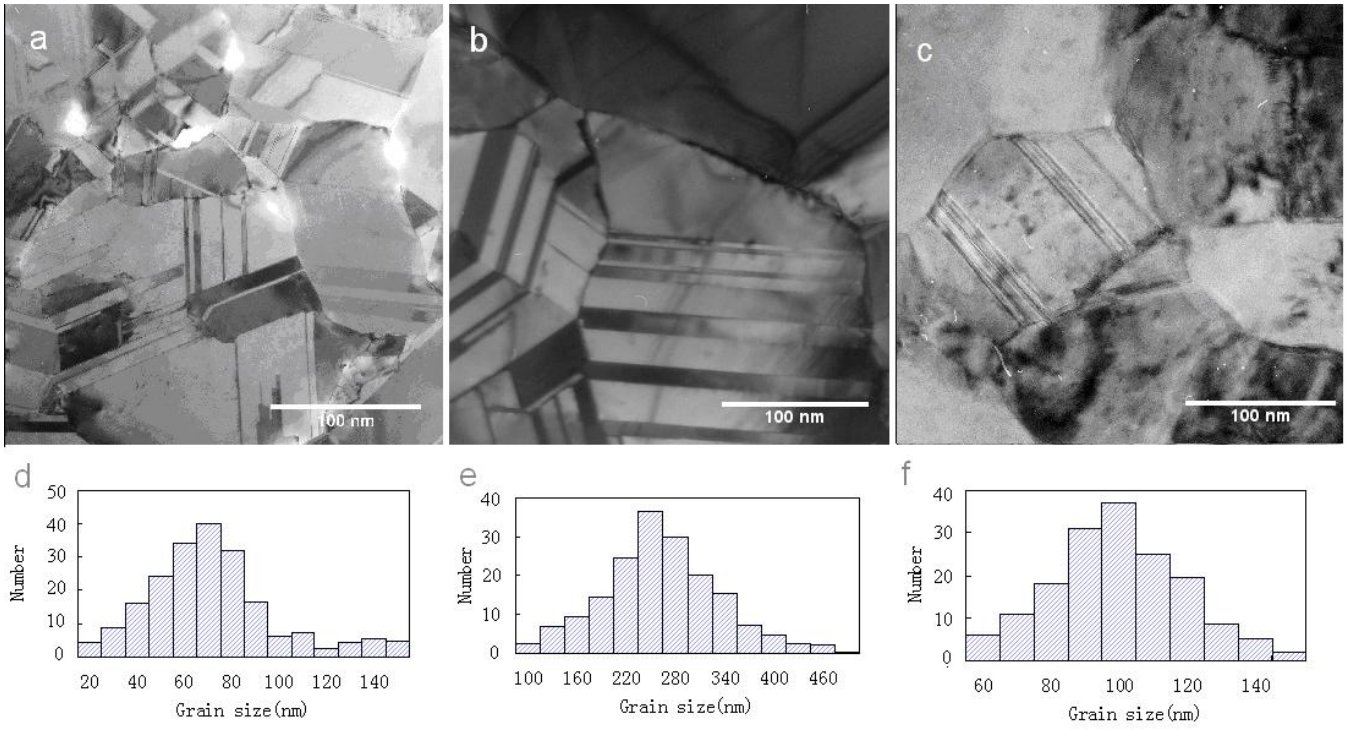

Figure 4.18 BF images showing the microstructure of samples FS2 (a), FS3 (b) and FS4 (c) at the same magnification. The grain size distribution of FS2 (d), FS3 (e) and FS4 (f).

Table 4.3 Summary of grain size and twin fraction of Cu films with different deposition parameters.

Sample Reference	On time	Off time	Peak Current Density (mA/cm^2)	Average grain size (nm)	Twin fraction in total area
FS1	constant	0 s	23	1200 ±12	4.5%
FS2	0.02s	1 s	500	70 ±8	14.5%
FS3	0.02s	2 s	500	250 ±9	35.6%
FS4	0.02s	3 s	500	100 ±8	10.0%

In DC deposition, the nucleation, grain growth and subsequent recrystallisation all happen continuously. In PC deposition, the current flow is only maintained during the on-time. Some researchers hold the opinion that it is only the on-time that Cu^{2+} migration and site nucleation occur [4]. Off-time is believed to be a stress relaxation stage followed by the recrystallisation and secondary grain growth [5]. In the present study, a high rate of deposition using the current density of 500 mA/cm^2 was maintained during the on-time of 0.02 s. This increased the density of nucleation and results in a fine grain structure. It has been reported that high levels of stress [3] and defects [5] are induced by a high and continuing deposition rate. In order to reduce the large amount of energy stored due to the high density of defects and high internal strain associated with a fast deposition rate, twin formation is favoured, because the twin boundary energy is normally much lower than the grain boundary energy [4, 5]. Furthermore, researchers have found that twin bands are frequently observed within the new crystals after recrystallisation and secondary grain growth [5, 6], and that twin boundaries formed during recrystallisation [7]. That is to say, recrystallisation may lead to the formation of high density of twins. Compared with the DC deposition, the PC deposition has the long off-time in each cycle where recrystallisation can continue, driven by the internal strain energy associated with the high peak current density (500

mA/cm^2) during the on-time. That is why pulsed electrodeposition favours high density of twins. The result of high density of nano-twinned grains observed in the present study (e.g. Figure 4.15) agrees with the literature [5, 6, 7].

Recrystallisation and the subsequent grain growth in electrodeposited copper films have attracted increasing attention. The grain growth of copper prepared using DC deposition stored at room temperature has been reported [6, 7]. However, neither in DC nor PC deposition, has limited evidence been specifically reported about recrystallisation as it might take place quite rapidly after the deposition or even during the deposition processing [5]. It has been indicated that recrystallisation and secondary grain growth is apparently similar to recrystallisation in cold-work metal [6]. New strain-free crystallites or grains recrystallise at highly strained regions and then grow to consume the parent material. As a result, a new microstructure stabilised by the removal of internal strain emerges in the metal with sometimes substantial increase of grain size [6].

As a result, the difference of grain size in figures 4.14, 4.15 and 4.17 can be probably explained in terms of the recrystallisation and secondary grain growth in the PC deposited copper films with different off-time. In FS2, fine grains of around 20 nm or even smaller size are observable. This may be due to the short off-time of 1 s for the limited grain growth. In FS3, the grains continually grow bigger due to the longer 2 s off-time, but some smaller grains of 50-80 nm are observed. In FS4, the grain shape is more regular than that in samples FS2 and FS3, which has been confirmed from the measurements of grain size distribution in figure 4.18. This may be because of the longest off-time 3s allowing the recrystallised grains to grow up and replace the

original grains, producing an equiaxed grain structure. However, further investigations need to be undertaken.

4.5 XRD and Texture Analysis of Copper Film

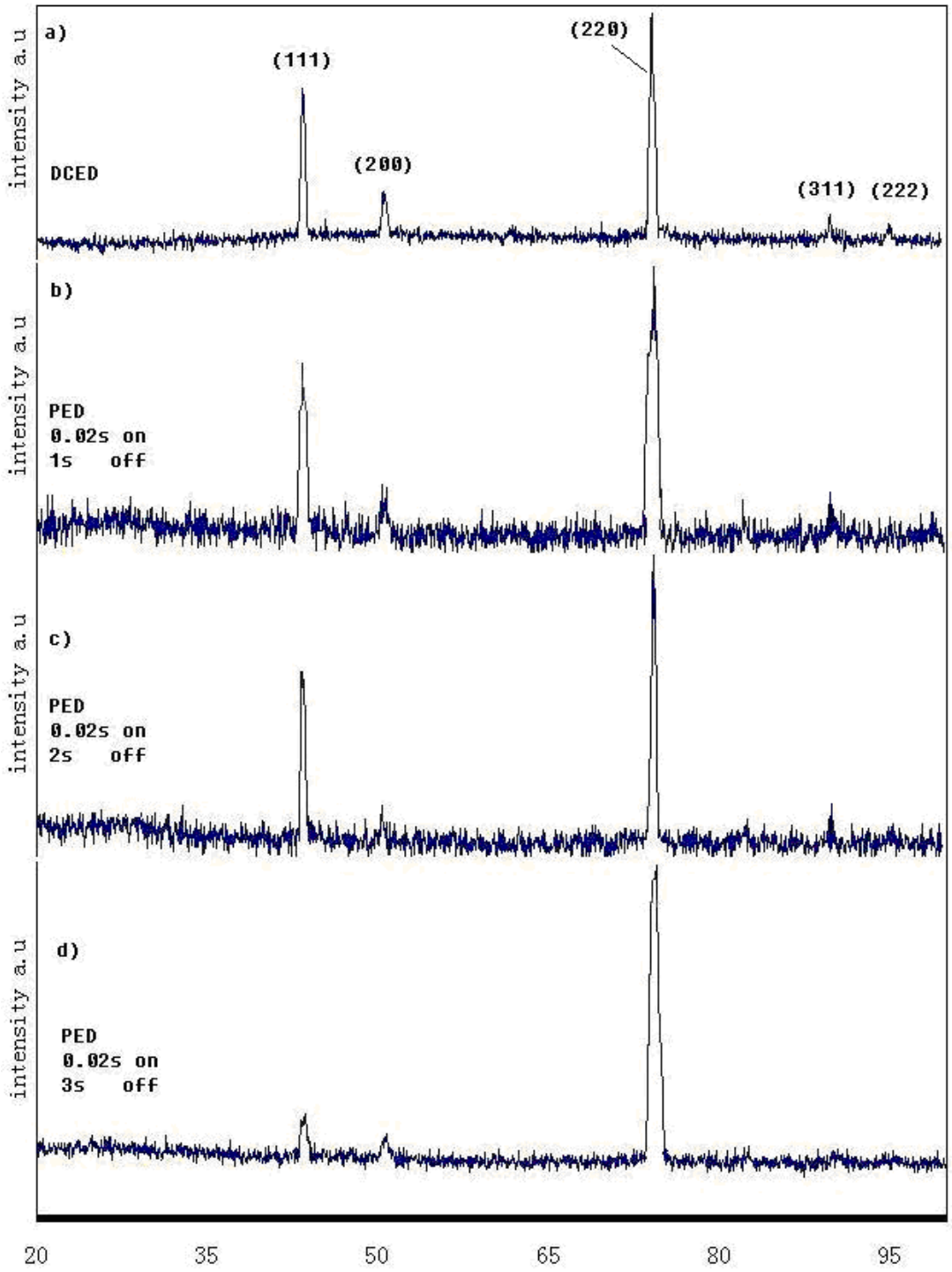

Figure 4.19 XRD patterns obtained from copper films deposited for 40 minutes with different processing parameters. a) DC deposition, current density of 23 m A/cm^2. b) PC deposition with on-time of 0.02 s, off-time of 1 s, peak current density of 0.5 A/cm^2. c) PC deposition with on-time of 0.02 s, off-time of 2 s, peak current density of 0.5 A/cm^2. d) PC deposition with on-time 0.02 s, off-time 3 s, peak current density of 0.5 A/cm^2.

The copper films were characterised using XRD. Figure 4.19 shows the XRD patterns obtained from samples FS1, FS2, FS3 and FS4, respectively. Five peaks (Copper) of (111), (200), (220), (311) and (222) can be observed on most of the samples, at 2θ of ~43.65°, 50.8°, 74.5°, 89.9° and 95.09° with the corresponding d-spacing of 2.071 Å, 1.795 Å, 1.272 Å, 1.089 Å and 1.044 Å, respectively. The (220) reflection intensity is the strongest. Compared with FS4, the (111) reflection peak is relatively stronger in samples FS1, FS2 and FS3. It means samples FS1, FS2 and FS3 have relatively strong (111) texture besides the (220) out-of-plane texture than the FS4. The XRD patterns obtained from samples FS1 and FS3 have narrow peaks, e.g. the (220) peak, than those obtained from samples FS2 and FS4, which indicates larger crystals and/or less strain.

The crystal size D can be estimated using Scherrer's formula from the full width at half maximum *L* of the peaks expressed in terms of radians [1].

$$D = \frac{0.94\lambda}{L\cos\theta}$$

where *L* is the Full Width at Half Maximum calculated from a particular reflection, λ is the wavelength of the incident X-rays (1.5406 Å) and θ is the diffraction angle. Based on the equation, the crystal sizes are calculated from the (220) reflection and are given in Table 4.4.

Table 4.4 Crystallite sizes of copper deposits with different electrodeposition parameters

Sample	*hkl*	Deposition parameter	Crystallite size (nm)
FS1	220	DC deposition with potential of 0.15 V	712.8
FS2	220	PC deposition with on time 0.02 s, off time 1 s	92.6
FS3	220	PC deposition with on time 0.02 s, off time 2 s	320.2
FS4	220	PC deposition with on time 0.02 s, off time 3 s	112.4

The results of PC deposits from table 4.4 are overall consistent with those of the PC deposits from table 4.3. Compared with the crystal size of DC copper film, the copper films prepared using PC deposition have a relatively smaller crystal size. Due to the higher peak current density, PC deposition provides higher nucleation rate, resulting in fine grains. In the present study, it has been confirmed that the PC deposition produces copper films with a smaller crystal size than the DC deposition.

A texture transition for copper films at a thickness of 5 μm has been reported [8], so the texture in a relatively thinner film might be different from thick films. X-ray diffraction was used to determine the texture of a 0.8 μm thick fresh copper film of sample FS4. From figure 4.20 (a) it can be observed that the XRD pattern displays a relatively strong (111) peak of FS4. The peak close to 45^{o} is from substrate (110) reflection. For comparison, a standard XRD pattern obtained from polycrystalline copper powders [9] is shown in figure 4.20 (b) (JCPDS 40-0836) and listed in table 4.5.

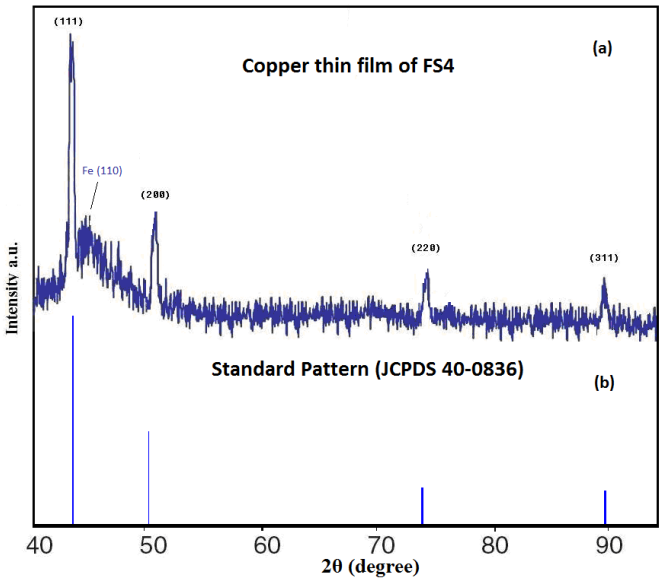

Figure 4.20 XRD 2θ pattern shows the diffracted peaks from (a) a Cu thin film of about 1 μm of sample FS4 and (b) standard polycrystalline copper powder (JCPDS 40-0836).

Table 4.5 RPI of XRD patterns for standard polycrystalline copper powders and thin copper film surface of sample FS4 (RPI – relative peak intensities to the highest peak).

Sample type	Peaks	(111)	(200)	(220)	(311)
Standard polycrystalline copper powers	RPI	100%	46%	20%	17%
Thin Cu film surface of sample FS4	RPI	100%	29.2%	14.6%	12.8%

In the standard XRD pattern obtained from polycrystalline copper powders, the four peaks are (111), (200), (220) and (311), whose relative peak intensities (RPI) to the highest peak (111) are 100%, 46%, 20% and 17%, respectively, as shown in table 4.5. For sample FS4 with the thickness of about 0.8 μm, RPI of the four peaks are 100%, 29.2%, 14.6% and 12.8%, respectively. It is obvious that, the RPI of (200), (220), (311) peaks of sample FS4 are all lower than those obtained from the standard powder sample. This indicates that [111] is the relatively favoured grain growth direction/preferred orientation at this thickness of sample FS4.

The pole figure scan was performed to examine/confirm the texture from the top layer of the 80 μm thick copper films. Four sets of pole figures of (111), (200), (220) and (311) were selected. The sample coordinate system is shown in figure 4.21, with the normal direction perpendicular to the film surface.

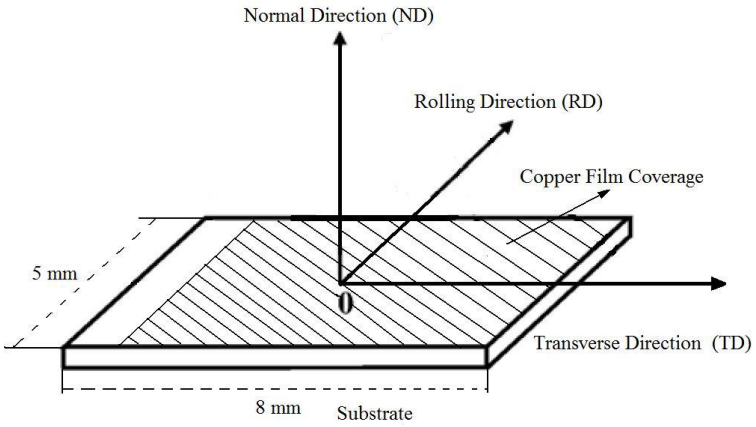

Figure 4.21 Schematic drawing showing the sample geometry.

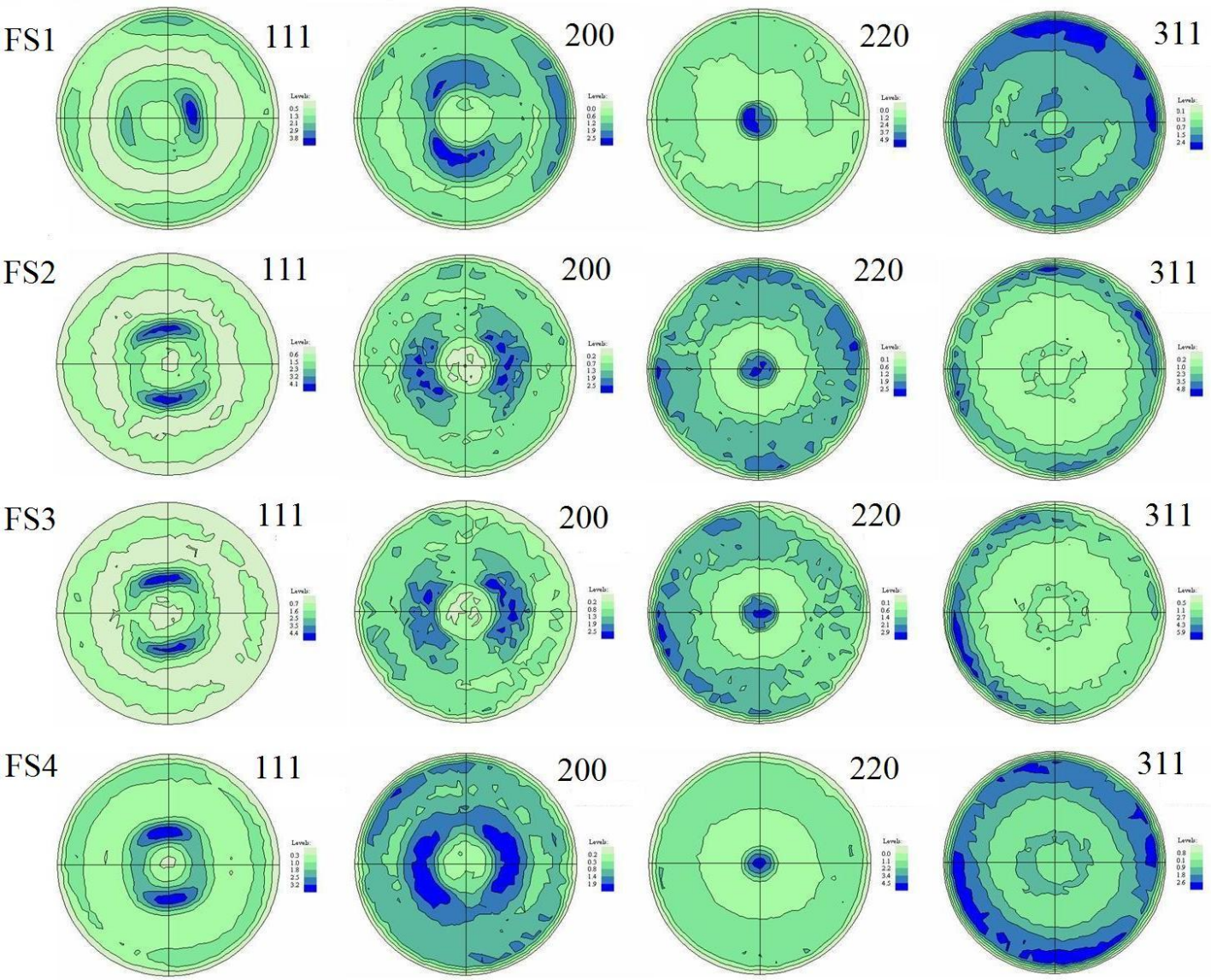

Figure 4.22 (111), (200), (220) and (311) pole figures of copper films for samples FS1, FS2, FS3 and FS4.

Figure 4.22 shows the pole figures obtained from samples FS1, FS2, FS3 and FS4. The (110) planes are observed mostly parallel to the sample surface. The maximum intensities of the (110) pole figure of samples FS1, FS2, FS3 and FS4 are 4.9, 2.5, 2.9, 4.5, respectively, indicating the relatively stronger texture of (110) in samples FS1 and FS4. The strong intensities of the (110) pole figure are only observed in the normal

direction of samples FS1 and FS4. But in FS2 and FS4, these can be partly detected in the rolling and transverse directions as well. The relatively obvious intensities of the (311) pole figure can be partly observed in the rolling and transverse directions of samples FS2 and FS3. The results suggest that the 80 μm thick sample has a strong <110>//ND texture.

Two texture components, (111) and (110) were observed in the current study with different film thicknesses. A similar texture transition from (111) to (110) of electrodeposited copper with increased film thickness has been reported [10]. It has been postulated that a possible reason to explain the texture evolution was the effect of the substrate [10]. With increasing film thickness, the deposit texture and crystal size is less influenced by the substrate and electrodeposition parameters gradually become the dominant factor determining the film texture and its crystal size [11]. In the current study, the copper layer deposited on the (111) oriented ferritic steel reveals the [111] // ND texture within ~0.8 micrometre thickness. For thicker layers the texture evolves into [110] // ND. Rasmussen [12] has reported that the deposited copper films gradually developed a [110] // ND texture when deposited onto both strong (111) texture Au and a random oriented Ni-P layer, but within 3 micrometres thickness the Cu layer inherits the (111) texture of the Au grains and random texture of the amorphous substrate. Furthermore, the first few micrometres of Cu deposits on a strong (110) oriented nickel-cobalt base alloy sheet (MP35N), are composed of (110) oriented grains, with a (111) texture formed in thicker layers [13]. Compared with the results from the current study and literature, the major texture component affected by the substrate is not always favourable in the thick films. It might be concluded that the substrate may affect the crystallographic texture only in the initial layers for the first few

micrometres thick and a gradual decrease of such influence in the subsequent growth of the deposits. Further systematic work needs to be explored to study the substrate effect of electrodeposited copper.

The thin film texture formation were initially described by Kozlov and Bicelli [14-16]. They proposed that the nucleation process of an initial layer on substrate may occur through the formation of 3D nuclei. They calculated the work of formation of nuclei of an FCC crystalline lattice on a substrate from the atomistic point of view. The investigations focused on the crystallization of the (111), (100) and (110) planes as a function of the applied voltage. The results revealed that the work of formation is inversely proportional to the amount of the critical nucleus [17]. The calculation showed that in the nucleation of ultrafine grains, the (111) plane has the smallest work of formation, so it is favoured when the film is initially deposited [18]. This is coincident with the fact that in all the planes of fcc metals, (111) has the lowest surface energy [19]. At the following nucleation process, the previous layer acts as the simultaneous "active" substrate. The classical 2D nucleation theory was then proposed to explain the subsequent grain growth from the energy point of view [20]. The work of formation (A_{hkl} $\times 10^{-19}$ J) for different planes has obvious difference. The formation of (110) plane at the moment costs the least energy, i.e., $A_{110}<A_{100}<A_{111,}$ in the subsequent grain growth [21].

As such, the currently observed preferable (111) texture in the thin copper film and the favourable (110) texture in the thicker films can be explained.

4.6 Cross-sectional Observations Using FIB

A dual beam FIB/SEM was employed to examine the cross section of sample FS3. FIB is a powerful technique to investigate the cross section of coatings. Ion channeling contrast may reveal more details compared to the purely electron image.

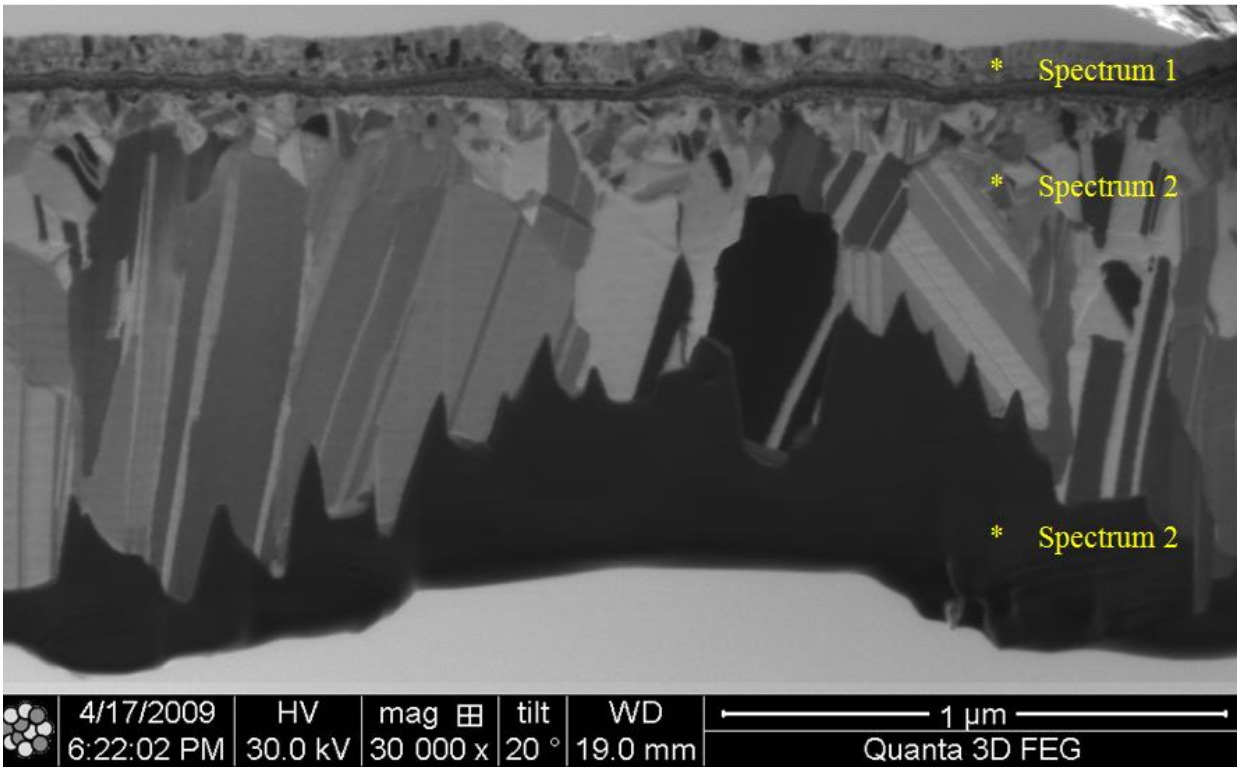

Figure 4.23 Ion channeling contrast image showing the cross-section of copper film FS3. The small grains and columnar grains are clearly visible. The EDX spectra appear in figure 4.24.

Figure 4.23 illustrates the cross section of an as-deposited sample FS3 showing the ion beam channeling contrast. The EDX analysis shows different composition, when measured 3 different positions on the cross section, as shown in figure 4.24,

corresponding to the substrate, copper film and tungsten protective layer, respectively.

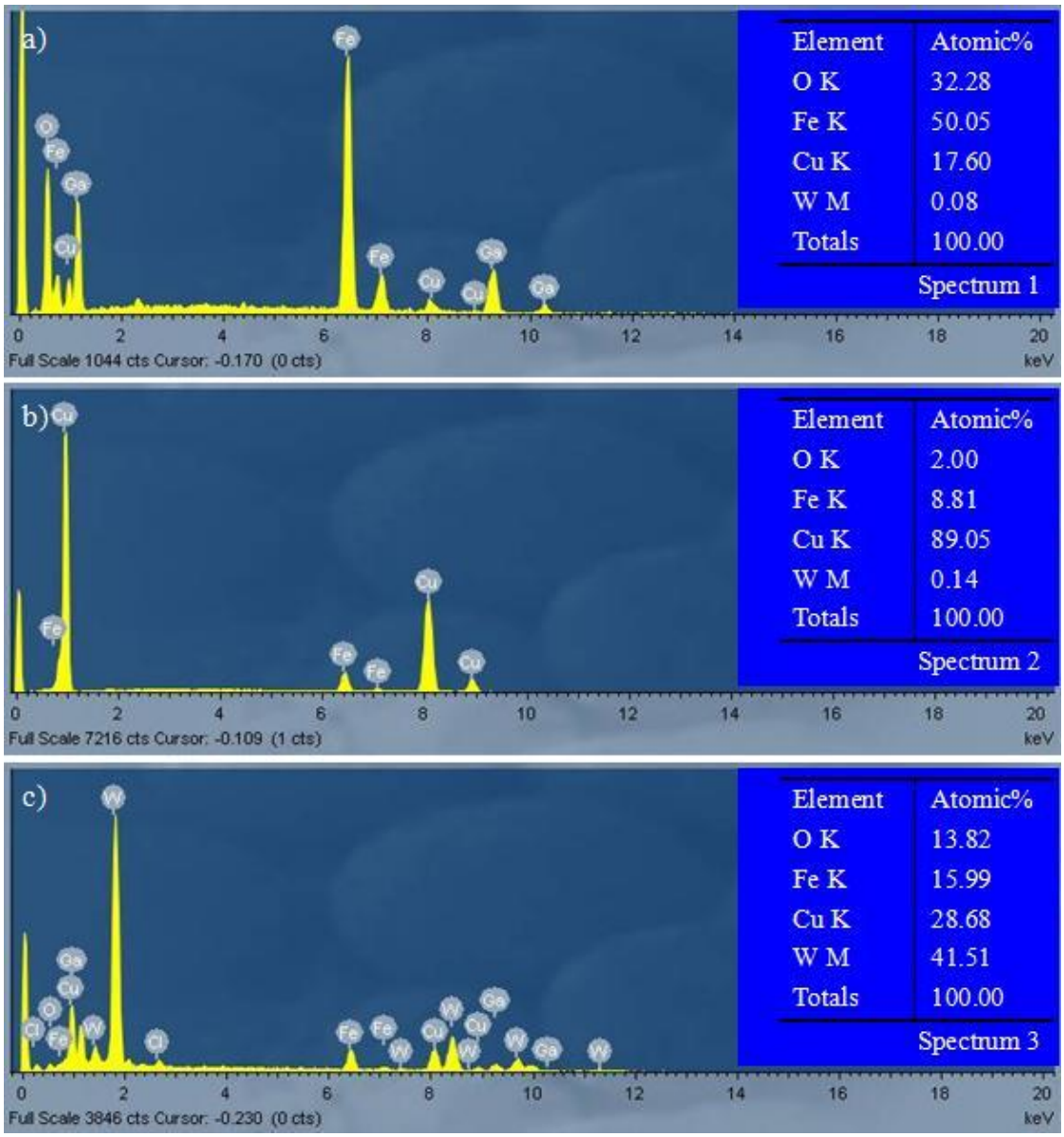

Figure 4.24 Typical EDX traces from Spectrum 1 (a), Spectrum 2 (b) and Spectrum 3 (c) in FIB image of figure 4.24.

Columnar grains are clearly observed following the first thin layer of very fine grains. The grain size increases with the distance from the substrate. Most of the grains close to the film/substrate interface are of about 20 nm. The total thickness of this ultrafine grain area is less than 200 nm. The subsequent layers consist of much larger columnar grains as the very fine grains generated are thermodynamically less stable than the

large ones because of the high energy associated with the high density of grain boundaries. The average width of the columnar grain is about 250 nm and the length can reach up to 1 μm. Most of the columnar grains are twinned. The thickness of twin lamellae ranges from several nanometers to several tens of nanometers. The twin fraction is about 34 %.

4.7 Room-temperature Grain Growth (Self Annealing)

Self-annealing (recrystallization & grain growth at room temperature) was observed in sample FS1 of about 80 μm thickness. The microstructure evolution as a function of time of a DC deposited copper film was studied using focused ion beam imaging (FIB) and back-scattered electron imaging (BSE). The EBSD was performed to investigate the grain orientation.

Fig. 4.25 shows the ion channeling contrast images taken from the same area of the copper film. Ion channeling contrast is caused by the ion induced secondary electrons yield, which is analogous to the secondary electrons produced by an incoming electron beam. A noticeable grain growth with time can be observed (e.g. see the dark grains in the blue-square). The channeling contrast images were obtained from the sample at 3 hours (a), 20 hours (b) and 76 hours (c) after the deposition, where the average grain size of about 580 nm, 660 nm and 860 nm were measured. The grains in dark have increased obviously in size. The darker contrast indicates a stronger channeling effect. Those grains appear darker because of the decrease in the number of ion induced secondary electrons that are emitted, giving “channeling contrast” or “orientation contrast” in the resulting image. The grains that appear bright contrast decrease the size with time. The bright contrast indicates a larger number of ion induced secondary electrons emanated from the sample surface. Plan-view BSE images were taken to confirm the microstructure evolutions of the DC deposited copper as shown in figure 4.26. The white dots might be contaminations either from the electropolishing solution or the oxides formed during electropolishing. The BSE images were obtained from sample FS1 as well at 3 hours (a), 20 hours (b) and 76

hours (c) after deposition, where the average grain size of about 570 nm, 650 nm and 870 nm were measured, which are consistent with the measurements obtained using ion beam imaging. The comparisons of results obtained from FIB imaging and BSE imaging are shown in figure 4.25.

In the literature, TEM and FIB imaging were the most frequently used to investigate the abnormal grain growth of electrodeposited copper films. However, ion beam bombardments gradually "eat" away the materials. In the present study, the BSE imaging shows consistent grain growth and similar grain size as that measured using ion beam. In other word, ion beam imaging does not give significant influence to the grain growth of copper film after electrodeposition.

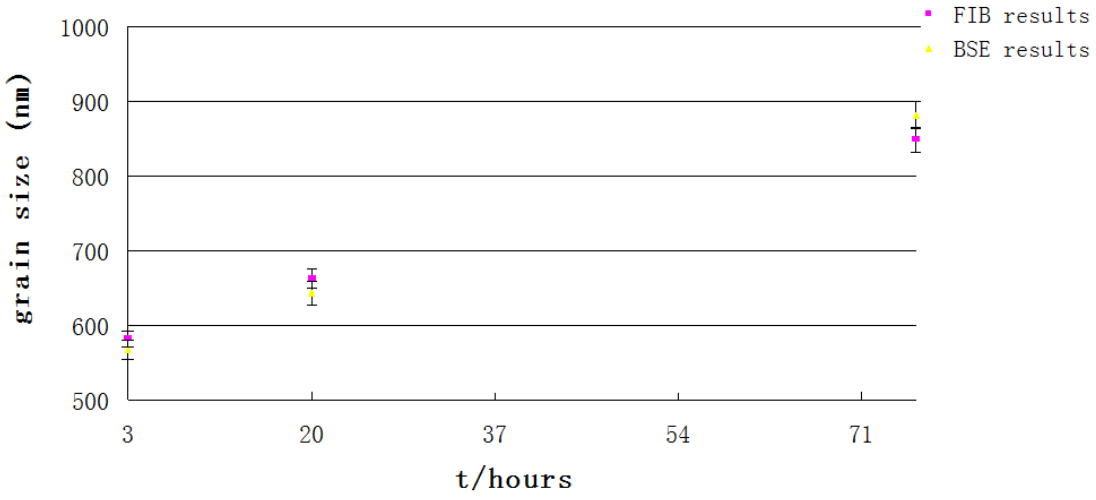

Figure 4.25 Grain size increment as a function of time (t) of DC Cu after electrodeposition.

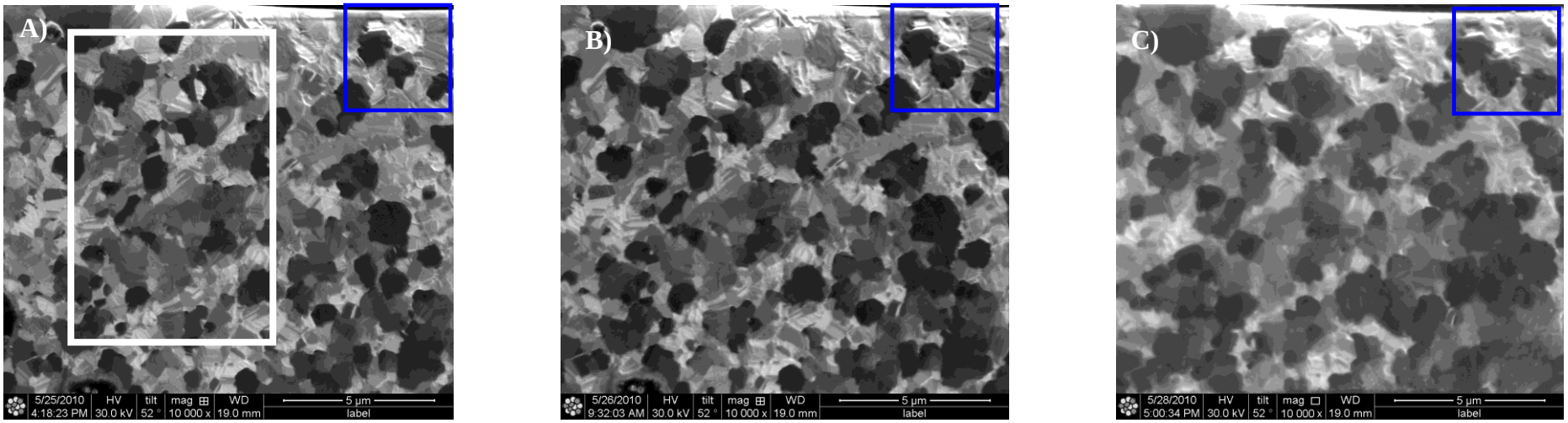

Fig. 4.26 FIB images showing microstructure evolutions as a function of time (t) of sample FS1 in the same region. A) t = 3 hrs; B) t = 20 hrs; C t =76 hrs.

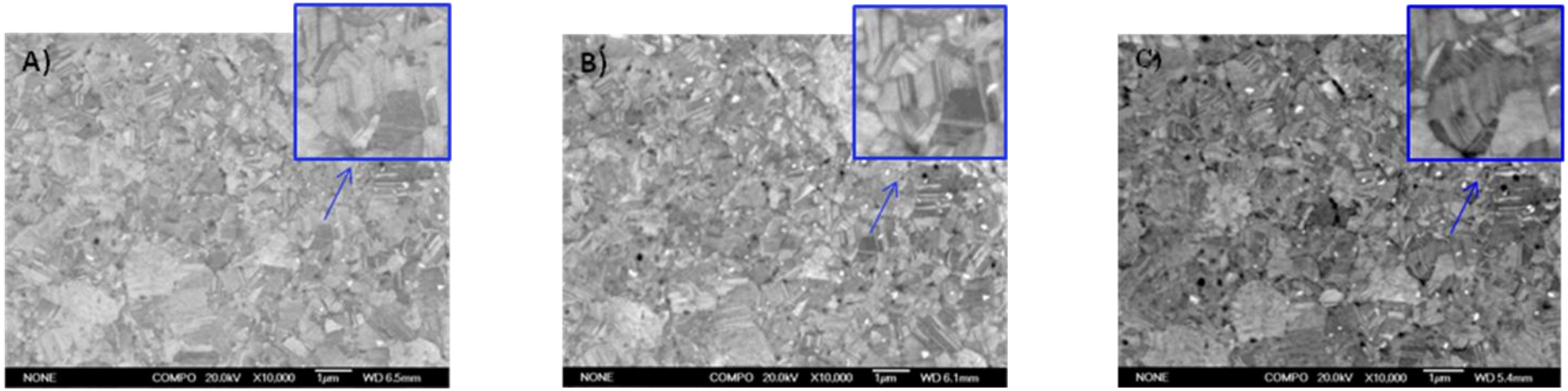

Fig. 4.27 BSE images showing microstructure evolutions as a function of time (t) of sample FS1 in the same region. A) t = 3 hrs; B) t = 20 hrs; C t = 76 hrs

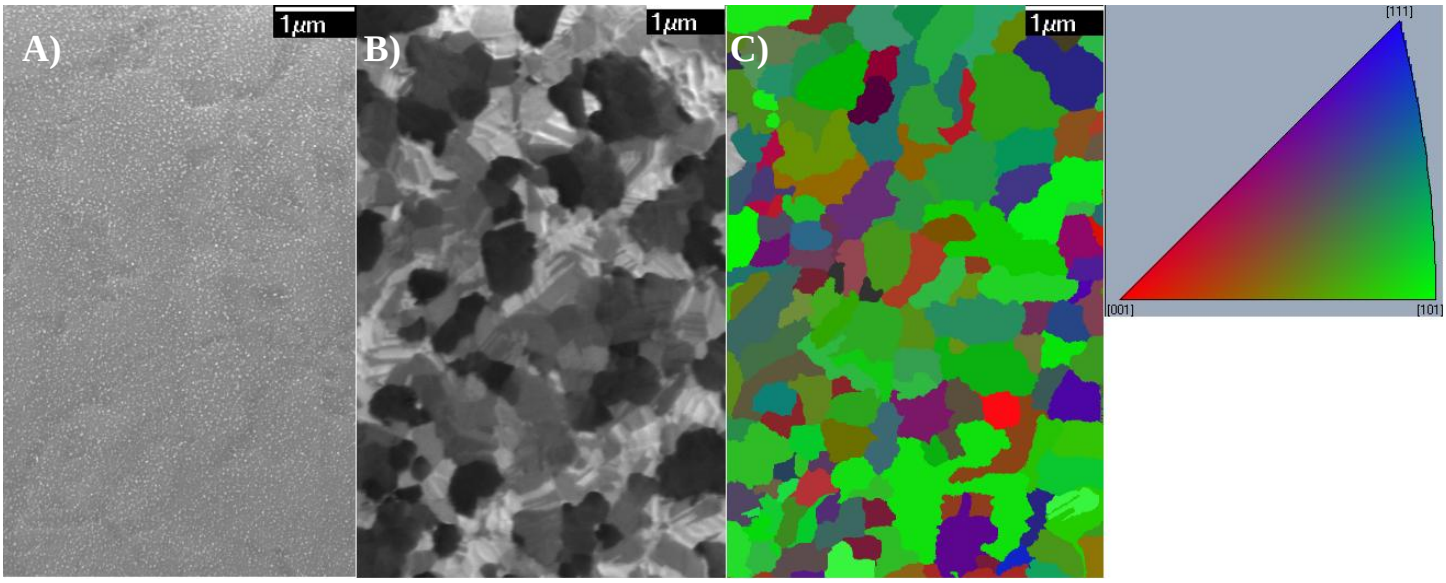

Figure 4.28 SEM a), FIB b) and OIM c) images of the same region showing the microstructure and grain orientations of copper films after deposition for 20 hours with the indication colour code.

Figure 4.28 shows the microstructure and EBSD orientation image maps obtained from the electrodeposited copper films marked by the white square in figure 4.26 a). The secondary electron image in figure 4.27 a) does not reveal the grain structure, but the FIB image and OIM clearly indicate the grain structure and its orientations. The electrodeposited Cu film has strong [110]//ND texture. Most grains which appear darker in b) possess the out-of-plane direction of [110], and are more likely to grow up with time after the deposition.

It is known that grain growth occurs during thermal annealing of nanocrystalline metals and alloys [22]. In the case of cold-worked material, the grain growth at relatively low temperature could be caused by the high strain energy. It has been suggested that the energy stored, in the form of high density crystalline defects such as dislocations and point defects, is likely the main driving force of this phenomenon [23-25], but the evidence is limited [6]. It has been widely recognized that materials

synthesized by deposition techniques are often plagued by high levels of stress [3]. High levels of internal strains, large volume fraction of grain boundaries and high density of dislocations/defects/impurities may result microstructure evolution.

Surface energy and strain energy minimisation has been proposed to explain the abnormal [110] grain growth direction in the electrodeposited copper [26, 27]. (100), (110) and (111) are the three low-index surface energy planes in FCC metals [19], and are likely to be the major texture components or possess higher volume fraction in order to reduce the whole energy of the material. [111] grain growth direction is preferred due to its lowest surface energy in FCC structure [19]. In the current study, grains with [110]//ND are not only favourable to form but also more preferred in the abnormal growth rather than the grains with [111]//ND in the thick copper film. The analogous phenomenon was reported on the abnormal grain growth in polycrystalline films [26]. This was explained from the view of film stress with a critical film thickness [26, 27]. It has been reported that, through the cross-section observation, the microstructure evolution (texture transition and/or abnormal grain growth after deposition) does not occur until the grain growth reaches the boundary of normal columnar grain structure [26]. Thompson [26] has reported that the driving force of the preferential growth of grains with orientations in a critical film thickness was the surface energy and strain energy minimisation. He [26] has indicated that for fcc metals, surface energy minimisation drives the nucleation and grain growth at low thickness when the surface energy is dominant; while strain energy minimisation drives the nucleation, grain growth and recrystallisation at large thickness when the strain energy is dominant. The critical film thickness has been suggested to be determined by several factors as following, the grain size in preferential growth orientation; the

surface energy difference (r_1-r_2), where r_1 is the energy of the top and bottom surfaces of the growing grain, r_2 is the corresponding average energy of the matrix grains; temperature difference between the current temperature and the temperature at which the film was deposited [26]. Sanchez and Arzt [28] have reported the similar phenomenon of thin film of aluminum alloys deposited onto oxidised silicon silicon single crystal substrates. They has explained that the strain energy densities difference between the typical (111) and (110) oriented grains provided a sufficient driving force advantage for the preferred abnormal growth of the (110) grains in the film plane. In-plane stress in a grain is a function of grain orientation factor, i.e. the yield stress of the grain varies with its orientation [29]. They [29] calculated the stress gradients and strain energy densities between adjacent grains of different orientations. The calculated orientation factor of (111) oriented grains is the 3.46, which is the largest value among 7 low index orientations including (100), (110), (111), (210), (211), (221), (311). The orientation factor is 1.42 for (110) oriented grains which is the smallest [28]. This suggests that the yield stress of (110) oriented grains is smaller than any grains. Therefore, the observed growth of grains of (110) oriented will lead to an overall strong energy reduction, which confirms the explanation by the strain energy minimisation.

In summary, at a large film thickness, the strain energy minimization of (110) oriented grains are likely to drive the observed abnormal growth. However, further investigations are needed.

The ion induced channeling contrast is more obvious than the back-scattered electron channeling contrast as shown in figures 4.26 and 4.27. The principle for

back-scattered electron channeling contrast is similar to ion channeling contrast. It has been reported that the penetration depth for an electron is much larger than for an ion and the orientation-dependent change in penetration is resultantly much smaller [30]. Therefore, the maximum orientation-dependent change in yield of back-scattered electrons per incident electron is much smaller than the orientation dependent change in ion induced electron yield. So the available orientation contrast is much weaker in electron imaging than in ion imaging. Furthermore, it has been suggested that the ion channeling effect is the strongest in the grains with [110]//ND orientation [31]. This is consistent with the current observation. Kempshall et al [31] have calculated the sputtering yield from the channeled and non-channeled fraction of differently oriented grains using the Lindhard-Onderdelinden [32, 33] approach, and grains with [110]//ND were found to have the strongest channeling contrast. The main reason for the decrease in the sputtering yield is that the channeled ions whose energy loss was mainly caused by interaction with electrons rather than nuclei are able to penetrate deeper into the crystal lattice. The deeper penetration and the lower probability of nuclear collisions near the surface limits the probability that the ion will cause a collision cascade that will contribute to the electron yield. Further analysis is needed to understand the ion channeling effect.

4.8 Nanohardness and Elastic Modulus of Cu Films

To minimise the effect of substrate, a 50 mN peak load was used to measure the hardness (H) and elastic modulus (E) from the surface of all samples with 80 μm thickness. The maximum depth of the indent is around 1500 nm. Typical load-displacement curves obtained from samples FS1, FS2, FS3 and FS4 are shown in Figure 4.29. It can be seen that PC deposited samples exhibit a shallower penetration depth as compared to the DC deposited sample (FS1).

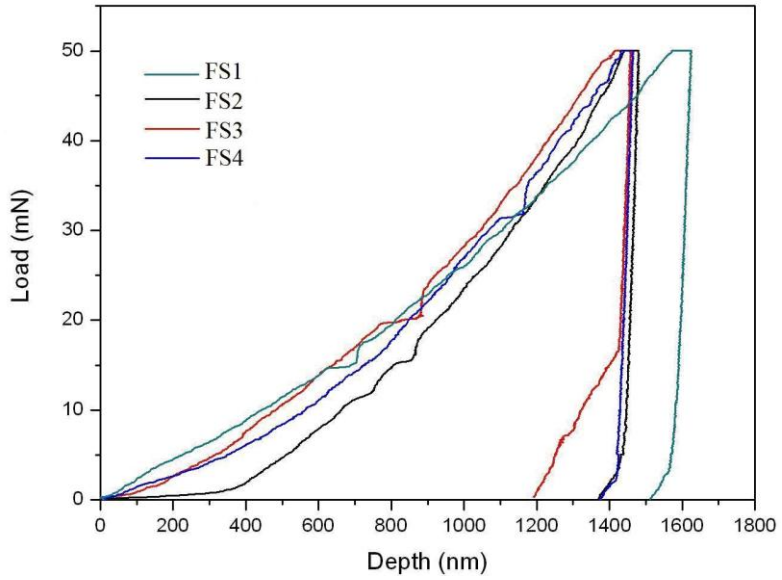

Figure 4.29 Typical nano-indentation loads against displacements curve.

Table 4.7 summarises the hardness and elastic modulus of the copper deposits. It shows that both the hardness and elastic modulus of the PC deposited samples are higher than that of the DC deposited sample. The highest hardness of 1.12 ± 0.01 GPa and elastic modulus of 166.2 ± 12.3 GPa were obtained from FS3. The lowest hardness of 0.83 ± 0.02 GPa and elastic modulus of 136.9 ± 7.9 GPa were obtained from sample FS1.

The hardness values can be quantitatively explained by both of Hall-Petch effects. Hall-Petch effect is understood by considering grain boundaries as obstacles to dislocation motion, i.e. hardness is inversely proportional to grain size. Sample FS1 possessed the largest grain size compared with the other samples, the hardness is the lowest. The fine-grained copper (Samples FS2, FS3 and FS4) overall has higher hardness value due to the relatively smaller grain size. Nevertheless it shall be noted that the strengthening mechanisms in nanocrystalline materials may be different from those in conventional grain sized materials. For instance, the grain size effect is of less (or even a negative) strengthening effect at very small grain size regime.

The hardness can also be derived from other strengthening methods. The highest hardness of sample FS3 can be explained by its microstructural differences from samples FS2 and FS4. The volume fraction of twin density in FS3 is the highest. The twin boundaries act strengthener to block dislocation motions within the grain. Previous investigations [34] demonstrated that the presence of twins blocks the propagation of slip bands, implying that the existing coherent twin boundaries behave more or less like grain boundaries in acting as obstacles to slip transmission. So the structural twins here could be the predominant reason to explain the highest hardness for sample FS3 compared with samples FS2 and FS4.

Table 4.7 Surface nano-hardness and Young's modulus of samples FS1, FS2 FS3 and FS4

Materials	FS1	FS2	FS3	FS4
Hardness (GPa)	0.83 ±0.02	0.99 ±0.02	1.12 ±0.01	1.01 ±0.04
Elastic's Modulus (GPa)	136.9 ±7.9	163.1 ±13.2	166.2 ±12.3	163.1 ±8.3

The elastic modulus of sample FS1 is 136.9 ±7.9 GPa, which is 7～23% higher than

that of conventional coarse-grained copper of 110-128 GPa [35]. For the PC deposited samples, the elastic modulus is nearly the same. The average elastic modulus is 164.1 GPa, which is 35% higher than that of conventional coarse-grained copper. It has been reported that copper is elastically highly anisotropic and the (111) preferentially oriented texture Cu has a higher elastic modulus than of the (110) or the (100) oriented texture Cu [35]. The present magnitude of the elastic modulus is almost 50% higher than that of the reported particular (111) oriented fine-grained Cu films [36]. It is known that the elastic modulus is determined by atomic bonding, but can be affected by film density or microcrack, texture, grain boundary sliding and grain coalescence and so on [37-39]. As mentioned in the literature, nanocrystallite size or the embedded nanostructured twins improves the film ductility remarkable [5, 40]. Maybe the improved ductility in sample FS3 contributes the highest value of elastic modulus. However, further work about comprehensively understanding the relationship between the structure - elastic modulus needs to be carried out.

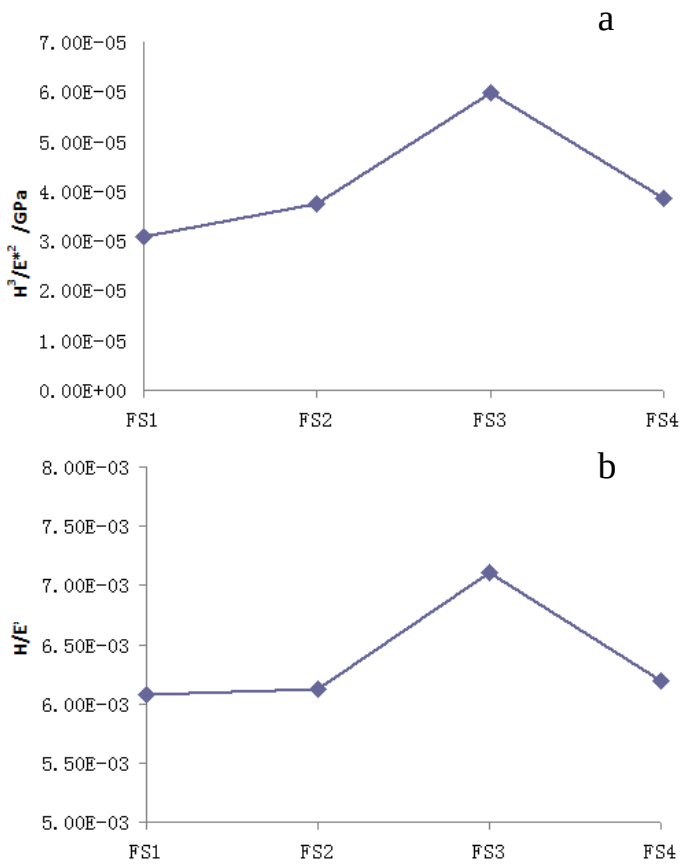

Figure 4.30 Variation of the ratio H^3/E^{*2} (a) and H/E (b) for the copper deposits as a function of sample.

For some cases, a more general relationship has been proposed to ascertain the mechanical resistance of a material through the ratio between plastic hardness and effective elastic modulus ($E^* = E/(1-\nu^2)$, where ν is the Poisson's ratio) [41-43]. The higher the ratios H^3/E^{*2} (resistance against plastic deformation) and H/E (resistance against elastic strain to failure) are, the better is the overall mechanical response of the film [44]. Plots of these relations (Fig. 4.30 a, b) point out that the maximum value is that of sample FS3. Response from the other deposits is lower than this one. This indicates that sample FS3 is the most favourable in terms of the overall mechanical performance.

References

1. A. Balasubramanian, D. S. Srikumar, G. Raja, G. Saravanan and S. Mohan, Surface Engineering. 25 (2009) 389.
2. N. R. Shamsutdinov, A. J. Bottger, B. J. Thijsse, Acta Materialia 55 (2007) 777.
3. A. J. Detor, A. M. Hodge, E. Chason, Y. Wang, H. Xu, M. Conyers, A. Nikroo, A. Hamza, Acta Materialia. 57 (2009) 2055.
4. X. Wang, Z. Z. Fang, H. Y. Sohn, International Journal of Refractory Metals & Hard Materials. 26 (2008) 232.
5. X.. Zhang, K. N. Tu, C. Zhong, Y. K. Tan , C. C. Wong , S. G. Mhaisalkar, X. L. Tung, C. H, Cheng, C. K., J. NN, 5, 8 (2008).
6. L. Haebum, D. William, S. Simon Wong, Journal of Vacuum Science and Technology. B 22 (2004) 5.
7. U. Kazuyoshi, T. Ritzdorf, S. Grace, Journal of Applied Physics. 86 (1999) 9.
8. P. Sonnweber-Ribic, P. Gruber, G. Dehm, E. Arzt, Acta Materialia. 54 (2006) 3863.
9. H. E. Swanson, E. Tatge, Natl. Bur. Stand. (US), Circ. 539 (1953) 15.
10. B. Hong, C. Jiang, X. Wang, Surface & Coatings Technology, 201 (2007) 7449.
11. G. I. Finch, A. L. Willams, Trans. Faradary Soc. 33 (1937) 564.
12. A. A. Rasmussen, J. A. D.Jensen, A. Horsewell, M. A. J. Somers, Electrochimica Acta,. 47 (2001) 67.
13. B. Z. Cui, K. Han, Y. Xin, D.R. Waryoba, A.L. Mbaruku, Acta Materialia, 55 (2007) 4429.
14. N. A. Pangarov, Electrochimica Acta. 7 (1962) 139.
15. N. A. Pamgarov, Journal of Electroanalytical Chemistry. 9 (1965) 70.
16. I. Stranski, R. Kaishev, The Journal of Physical Chemistry, B 35 (1937) 27.
17. V. M. Kozlov, L. Peraldo Bicelli, Journal of Crystal Growth. 177 (1997) 289.
18. V. M. Kozlov, L. Peraldo Bicelli, V.N. Timoshenko, Journal of Crystal Growth. 183 (1998) 456.
19. Y. Wen, J. Zhang, Solid State Communications 144 (2007) 163.
20. V. M. Kozlov, L. Peraldo Bicelli, Journal of Crystal Growth. 203 (1999) 255.
21. V. M. Kozlov, L. Peraldo Bicelli, Materials Chemistry and Physics. 62 (2000) 158.
22. A. J. Haslam, S. R. Phillpot, D. Wolf, D. Moldovan, H. Gleiter., Mater. Sci. Eng. A 318 (2001) 293.
23. C. Lingk and M. E. Gross, J. Appl. Phys. 84 (1998) 5547.
24. M. E. Gross, R. Drese, C. Lingk, W. L. Brown, K. Evans-Lutterodt, D. Barr, D. Golovin, T. Ritzdorf, J. Turner, and L. Graham, Mater. Res. Soc. Symp. Proc. 562 (1999) 215.
25. C. Lingk, M. E. Gross, W. L. Brown, and R. Drese, Solid State Technol. 42 (1999) 47.
26. C. V. Thompson, Scr Metall Mater. 28 (1993) 167.
27. K. N. Chen, A. Fan, C. S. Tan, R. Reif, C. Y. Wen, Applied Physics Letters. 81 (2002) 3774.

28. J. E. Sanchez, E. Artz, Scr. Metall. Mater, 27 (1992) 285.
29. C. V. Thompson, R. Carel, J. Mech. Phys. Solids. 44 (1996) 657.
30. I. M. Fielden, D. Bultrey, T. Vystavel, Jounnal of Physics: Conference Series 126 (2008) 012029.
31. B. W. Kempshall, J. Vac. Sci. Technol. B. 19 (2001) 3.
32. J. Lindhard, Phys. Lett. 12 (1964) 126.
33. D. Onderdelinden, Appl. Phys. Lett. 8 (1966) 189.
34. L. Lu, Y. Shen, X. Chen, L. Qian, K. Lu, Science. 422 (2004) 304.
35. T. Tsuru, Y. Shibutani, Physical Review B. 75 (2007) 035415.
36. D. Yu, F. Spaepen, Journal of Applied Physics. 95(2004) 2991.
37. S. H. Hong, K. S. Kim, Y. M. Kim, J. H. Hahn, C. S. Lee, J. H. Park, Composite Science Technology. 65 (2005) 1401.
38. C. Zener, Physical Review. 60 (1941) 906.
39. N. R. Shamsutdinov, A. J. Bottger, B. J. Thijsse Acta Materialia. 55 (2007)777.
40. Y. Shen, L. Lu, Q. Lu, Z. Jin, K. Lu, Scripta Mater,52 (2005) 989.
41. J. Musil, P. Karavankova, J. Kasl, Surf. Coat. Technol. 139 (2001) 101.
42. J. Musil, F. Kunc, H. Zeman, H. Polakova, Surf. Coat. Technol. 154 (2002) 304.
43. F. Regent, J. Musil, Surf. Coat. Technol. 142 (2001) 146.
44. A. Ibanez, E. Fatas, Surface & Coatings Technology, 191 (2005) 7.

Chapter 5 Conclusions

- The microstructure of the electrodeposited copper has been studied. Although the current results suggest that the off-time may have a significant effect on the resultant microstructure, more systematic experiments are needed to this end as a future work.

- The substrate does not show significant influence on the texture of the thick copper films. All copper films with a thickness ～80 μm show a strong (110) texture.

- Self-annealing has been clearly observed in a DC deposited copper film using both FIB and BSE imaging. Grains with [110]//ND orientation are likely to grow in the self-annealing.

- Sample FS3, with the highest twin density shows the largest value of H/E, indicating a better mechanical performance.

Chapter 6 Future Work

Some phenomena reported in this work are interesting but have not been subjected to a systematic study due to the time limitation. These topics can be interesting for future research. For example:

1) The self-annealing behaviour in electrodeposited copper films. The current study has clearly demonstrated using both the FIB and BSE imaging that grain growth occurs at room temperature. However, the current study was carried out only on DC deposited sample. It would be interesting to study systematically and to understand the self-annealing process. For instance, to answer a few questions: what affects the self-annealing and how? FIB study of copper films prepared with different PC deposition parameters can be used to observe the growth rate and its dependence on the microstructure. The preferred grain growth orientation (preliminary result from the current study shows [110]//ND for DC deposited thick films) and its dependence with films thickness might be useful to understand the mechanism(s) that govern the self-annealing. At very small thickness, [111]//ND is the preferred film texture but it is still not clear what's the preferred grain growth orientation in this type of thin film.

2) Systematic mechanical property studies of the electrodeposited copper films. Although the hardness of elastic modulus have been measured using nanoindentation technique, a more comprehensive study of the mechanical properties of electrodeposited films is desirable. Such a study, in conjunction with a more extensive microstructure characterisation, will enable a fuller understanding of the underlying deformation mechanisms and consequently contribute to establish understand the relationship between processing, microstructure and performance of the electrodeposited thin films.

Appendix

Conceptual design of micro-scale tensile testing device

Principles

The typical tensile strength of copper is as follows:

Material	Yield strength σ_0 (MPa)	Ultimate strength σ_1 (MPa)	Density (g/ cm^3)
Cu (Purity :99.9%)	70	220	8.92

Table 1 Typical properties of copper [1]

The sample size is 6 mm x 3 mm x 0.2 mm which is appropriate to place in SEM, so the expected force at the point where the yield strength is reached is

$$F = \sigma_0 \times Area = 70MPa \times (3mm \times 0.2mm) = 42N$$

The expected force at the ultimate strength is

$$F = \sigma_1 \times Area = 220MPa \times (3mm \times 0.2mm) = 132N$$

The Young's modulus of copper ranges between 110GPa and 128Gpa [1], so the maximum strain within the elastic deformation ε is

$$\varepsilon = \frac{\sigma_0}{E} = \frac{70MPa}{110GPa} = 6.364 \times 10^{-4}$$

Consequently the maximum elastic deformation l is

$$l = \varepsilon \times length = 6.364 \times 10^{-4} \times 6mm = 3.818\mu m$$

For the displacement measurement, several methods are available. Commercial sensors such as capacitance displacement sensors with nanometre scale resolution are used commonly, but a good error analysis is needed to obtain the effective

deformation of the gauge section of the tensile specimen [2]. Modern optical strain sensors, such as using electronic speckle pattern interferometry and digital image correlation, do not have sufficient accuracy, although they are capable of measuring strains directly. SEM imaging methods have high accuracy but with higher costs. Force is measured with commercial sensors or load cells integrated with specimens; this is easy to operate, but also involves problems, such as aggravating the difficulty of strain measurement of the gauge section due to the general stiffness of the testing device being covered [3,4].

Actuation technologies exist that offer nanometer and sub-nanometer resolution, and others are available that offer large ranges of motion; the challenge is obtaining a system that provides a high dynamic range (i.e. fine step sizes and large ranges) [4]. Piezoelectric actuators offer decided advantages in terms of resolution of motion (since the principle is based on atomic-level straining) and speed control, and can be fabricated in special stack geometries to extend the range of motion. However, piezo-based actuation systems are susceptible to direct current (DC) drift and stack designs are not always very compact, precluding use in restricted spaces (e.g in situ experiments) [4]. High dynamic range actuators are commercially available that make use of the inertial drive mechanism mentioned previously, combining precision motion of piezoelectric materials with large travel (e.g. tens of millimeters), which is recommended. This motion can be accomplished using linear sliding or by a ratcheting motion of piezoelectric jaws over a finely threaded screw.

Plan (unit: mm)

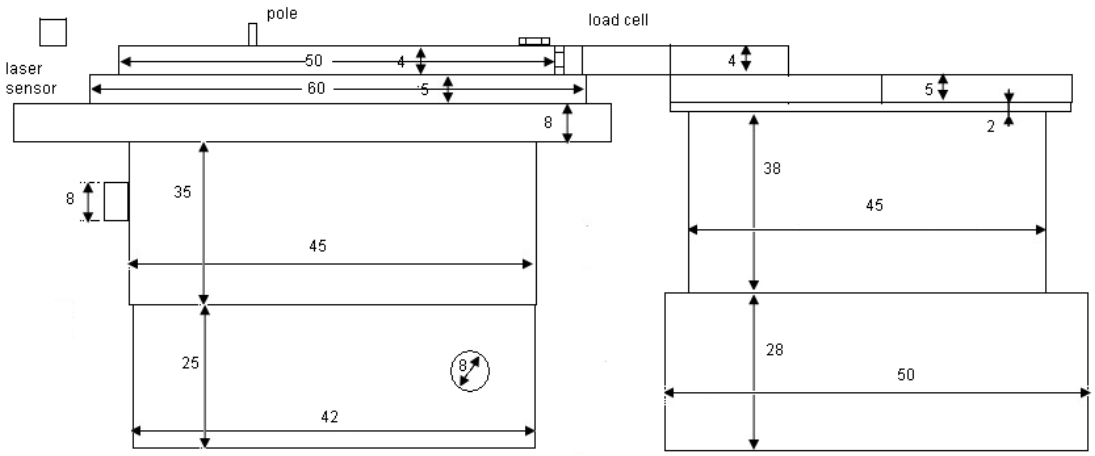

Figure 1 Front view of the micro-tensile testing device

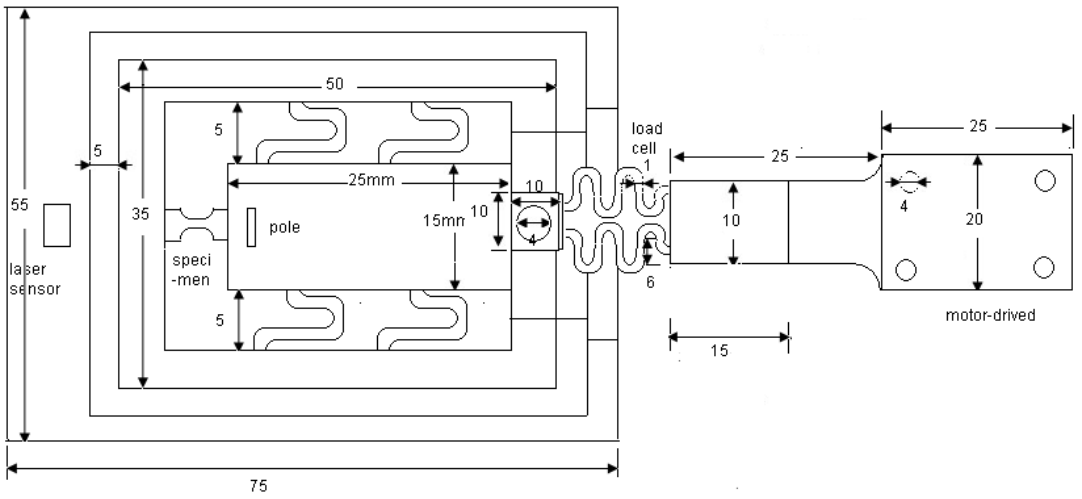

Figure 2 Top view of the micro-tensile testing device

The conceptual design of micro-tensile testing device is illustrated in figures 1 and 2. The dimension is according to the Philips XL30 SEM chamber size and actual parts size.

References

1. T. Tsuru, Y. Shibutani, Physical Review B. 75 (2007) 035415.
2. C. Malhaire, C. Seguineau, M.Ignat, C.Josserond, L.Debove, S.Brida, J.M.Desmarres, X.Lafontan, MRS Proc. 1052 (2009) 978.
3. C. Seguineau, M. Ignat, C. Malhaire, S. Brida, X. Lafontan, J.M. Desmarres, C. Josserond, L. Debove. Integration and Packaging of MEMS/MOEMS 1109 (2008) 8.
4. Oliver Kraft, Cynthia A. Volkert, Advanced Engineering Materials, 3 (2001) 99.